Alma Mater Studiorum · Università di Bologna

Scuola di Scienze
Corso di Laurea Magistrale in Fisica

# Charge and Spin Trasport in Memristive $La_{0.7}Sr_{0.3}MnO_3/SrTiO_3/Co$ Devices

**Relatore:**
**Prof.ssa Beatrice Fraboni**

**Correlatore:**
**Dott. Valentin Alek Dediu**

**Presentata da:**
**Lorenzo Vistoli**

**Sessione II**

**Anno Accademico 2014/2015**

Desidero ringraziare Alek per la passione per la fisica che è riuscito a trasmettermi durante questi mesi di lavoro. Grazie a tutto il gruppo di spintronica all'ISMN: Alberto, Alessandro, Elisabetta, Eugenio, Fabio, Federico, Ilaria, Patrizio, Sara e Silvio.
Inoltre vorrei ringraziare la Prof.sa Fraboni per il suo aiuto dall'università.
Ringrazio la mia famiglia per il tutto il supporto in questi anni, senza di voi questa tesi non sarebbe stata possibile.
Vorrei anche ringraziare tutti quelli che in questi anni ci sono stati, ma siete troppi da elencare (e per questo sono molto grato).
Sapete chi siete!

# Abstract

Il lavoro svolto si concentra sul trasporto di carica e spin in dispositivi trilayer $La_{0.7}Sr_{0.3}MnO_3/SrTiO_3/Co$ multifunzionali. Questi dispositivi mostrano sia magnetoresistenza che resistive switching, con un'interessante interazione fra i due effetti. Le giunzioni $SrTiO_3$ sono state scelte per questo lavoro sia per via dei precedenti studi su $SrTiO_3$ come barriera in dispositivi spintronici (cioè dispositivi con magnetoresistenza), sia perché sono promettenti come materiale base per costruire memristor (cioè dispositivi con resistive switching). Il lavoro di tesi è stato svolto all'Istituto per lo studio dei materiali nanostrutturati (ISMN-CNR) a Bologna.

Nella prima parte di questa tesi illustrerò la fisica dietro al resistive switching e alla magnetoresistenza di dispositivi trilayer, mostrando anche risultati di studi su dispositivi simili a quelli da me studiati. Nella seconda parte mostrerò la complessa fisica degli ossidi utilizzati nei nostri dispositivi e i possibili meccanismi di trasporto attraverso essi.

Nell'ultima parte descriverò i risultati ottenuti. I dispositivi $La_{0.7}Sr_{0.3}MnO_3/SrTiO_3/Co$ sono stati studiati tramite caratterizzazione elettrica, di magnetotrasporto e con spettroscopia di impedenza. Le misure ottenute hanno mostrato una fisica molto ricca dietro al trasporto di spin e carica in questi dispositivi, e la mutua interazione fra fenomeni spintronici e di resistive switching rappresenta una chiave per comprendere la fisica di questi fenomeni. Analisi dati della dipendenza della resistenza della temperature e caratteristice corrente-tensioni saranno usati per quantificare e descrivere il trasporto in questi dispositivi.

# Abstract

This thesis focuses on the transport of charge and spin in trilayer $La_{0.7}Sr_{0.3}MnO_3/SrTiO_3/Co$ multifunctional devices. These devices show both magnetoresistance and resistive switching, with an interplay between the two effect. $SrTiO_3$ junctions were chosen because of the extensive studies conducted on/$SrTiO_3$-based spin valves (devices showing magnetoresistance) and $SrTiO_3$based memristors (devices showing resistive switching). The thesis work was carried out at the Institute of Nanostructured Materials (ISMN-CNR) in Bologna, Italy.
In the first part of this thesis I will illustrate the physics behind resistive switching and magnetoresistance of trilayer devices, showing also previous results of studies on similar multifunctional devices. In the second part I will explain the complex physics of the oxides used in our studied device. Then I will show the possible transport mechanisms in insulating junction, applicable to $SrTiO_3$ junctions.
The $La_{0.7}Sr_{0.3}MnO_3/SrTiO_3/Co$ devices were studied through extensive electrical, magnetotransport and impedance spectroscopy. These measurements show very rich physics underlying the transport of charge and spin in these device, and the interplay between resistive switching and spintronic properties represents a key to understanding the physics behind these effect. Data analysis on the temperature dependence of the resistance and current-voltage characteristics will be used to quantify and describe the transport in these devices.

# Contents

**1 Memristive and spintronic devices** **1**
1.1 Memristors . . . 1
1.2 Spintronic devices . . . 4
1.2.1 Tunneling Magnetoresistance . . . 5
1.2.2 Giant magnetoresistance . . . 8
1.3 Memristive Spin Valves . . . 13
1.3.1 Memristive organic spin valves . . . 13
1.3.2 Memristive $TaO_x$ spin valves . . . 17

**2 Oxides for memristive and spintronic devices** **21**
2.1 LSMO . . . 21
2.1.1 Jahn Teller rffect and rxchange interaction . . . 21
2.1.2 Doping and exchange properties . . . 24
2.1.3 Magnetoresistance . . . 26
2.2 STO . . . 28
2.2.1 STO spintronic devices . . . 28
2.2.2 STO memristors . . . 31
2.3 Conduction through insulators . . . 33
2.3.1 Tunneling . . . 33
2.3.2 Nearest neighbor hopping . . . 34
2.3.3 Mott variable-range hopping . . . 35
2.3.4 Efros-Schklovskii variable range hopping . . . 35
2.3.5 Poole-Frenkel effect . . . 36
2.3.6 Zabrodskii-Zinov'eva analysis . . . 37

**3 Pinholes in vertical devices** **39**
3.0.1 Thickness dependence criterion . . . 40
3.0.2 Conductance criterion . . . 41

3.0.3 Temperature dependence of the resistance: the parallel circuit model . . . 43
3.0.4 Ballistic magnetoresistance . . . 45

**4 Experimental setup** **47**
4.1 Device fabrication . . . 47
4.1.1 LSMO electrodes and STO barrier . . . 49
4.1.2 Cobalt electrode . . . 49
4.2 Electrical characterization . . . 50
4.3 Magnetic characterization . . . 51

**5 Structural characterization** **55**

**6 Transport and forming pulse in amorphous and epitaxial STO** **59**
6.1 Amorphous STO devices . . . 59
6.1.1 Hopping in a-STO junctions . . . 59
6.1.2 Parallel circuit model in a-STO junctions . . . 66
6.2 Epitaxial STO devices . . . 79

**7 Memristive and spintronic amorphous STO devices** **83**

**Bibliography** **93**

Chapter 1

# Memristive and spintronic devices

In this thesis I will study trilayer junctions that are both memristors – devices that feature resistive switching – and spin valves – devices that feature magnetoresistance. These devices are interesting both for the fundamental device physics and for the potential applications. Memristors are two terminal devices and, while they are used for many applications in computing, are conceptually different from the three-terminal physics of CMOS technology; thus a third input, the magnetic field, that can modulate the device, makes these devices more attractive for beyond CMOS technology. The second reason is that the knowledge on resistive switching explains how spin transport works in certain devices while the presence of resistive switching in spintronic devices can lead to novel applications of such devices.

## 1.1 Memristors

In 1971, the engineer Leon Chua theorized the existence of element of electric circuits that no one had yet found – the memristor [7]. Chua argued that there exist four fundamental variables in a circuit: the electric current $i$, voltage $v$, charge $q$ and magnetic flux $\phi$. Since charge and current are governed by

$$i = dq/dt$$

and voltage and magnetic flux are governed by Faraday's law

$$v = d\phi/dt$$

it means there are four possible circuit elements that can connect the variables: the resistor ($R = dv/di$), the capacitor ($C = dq/dv$), the inductor ($L = d\phi/di$) and the fourth, never seen before, memristor ($M = d\phi/dq$). The relationship between circuit elements and variables is outlined in fig. 1.1.

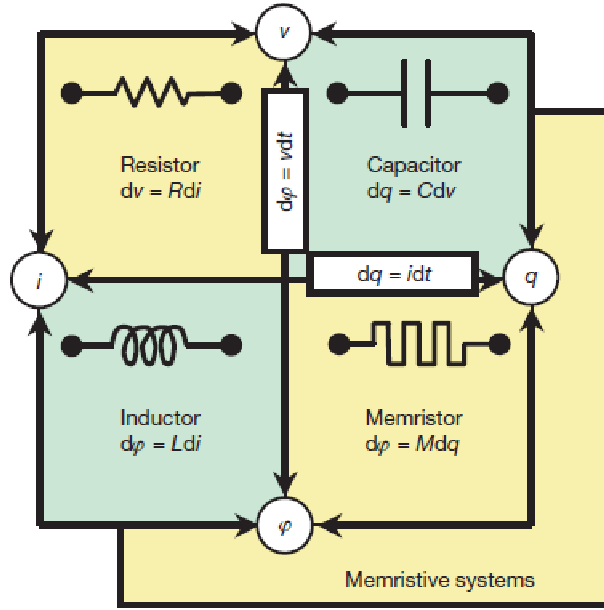


Figure 1.1: The four fundamental circuit elements.

From the memristor equation and using Faraday's law and the conservation of charge, we obtain

$$v = Mi. \tag{1.1}$$

If $M$ is a constant then we have obtained nothing more than a normal resistor, but if $M$ depends $q$ itself we obtain the general and more interesting formula.

$$v = M(q)i, \tag{1.2}$$

but no physical model was able to give this simple equation. Chua and Kang generalized the concept of memristor to a system described by the equation

$$v = R(w, i)i \tag{1.3}$$

where

$$\frac{dw}{dt} = f(w, i). \tag{1.4}$$

$R$ and $f$ can be functions of time but this analysis is restricted to the case of time-independent devices. It is clear from these equation that we are essentially talking about devices that feature resistive switching

Strukov et al. [8] produced a model of a device that acted as a memristor device described by the equation 1.2. Consider a semiconductor of thickness $D$ sandwiched between two metallic contacts. In a region of thickness $w$ with a high density of dopants and resistance $R_{ON}w/D$ while the rest has low density of dopants and a

higher resistance $R_{OFF}(1-w)/D$, as in fig 1.2. An equivalent circuit to this device is a series of two variable resistors where their resistance is determined by $w$ (the first is $R_{ON}w/D$ and the second $R_{OFF}(1-w/D)$). Thus the ohmic law of this circuit is

$$v(t) = \left(R_{ON}\frac{w}{D} + R_{OFF}\left(1-\frac{w}{D}\right)\right)i(t). \tag{1.5}$$

Applying a voltage to this devices moves the charged dopants, giving rise to the resistive switching. Linear ionic drift of the dopants in an uniform field, with mobility $\mu_D$, gives

$$\frac{dw}{dt} = \mu_D\frac{R_{ON}}{D}i(t), \tag{1.6}$$

which is then integrated, giving

$$w = \mu_D\frac{R_{ON}}{D}q(t). \tag{1.7}$$

Combining eq. 1.5 and 1.7, and considering $R_{OFF} \gg R_{ON}$ gives

$$M(q) = R_{OFF}\left(1-\frac{\mu_D R_{ON}}{D}q^2(t)\right), \tag{1.8}$$

which is the charge-dependent memristor predicted by Chua. It is also interesting to note that in no part of this treatment was any magnetic field involved, even though the concept of the memristor itself revolves around the magnetic flux.
There is an obvious boundary to $w = q(t)\mu_D R_{ON}/D$, which is

$$0 \leq w \leq D \tag{1.9}$$

outside of which this treatment is not viable and the system is not a memristor. A simulation of such a device is in fig. 1.2b, where it is interesting to note the hysteretic behavior the produces different (differential) resistances around $v = 0$ in different loops.
While this behavior resembles the already observed bipolar resistive switching but the mechanism itself is quite different since the model used linear diffusion and the result is a multi-state device since $w$ can take any value between 0 and $D$. If we consider nonlinearities in the ionic motion, instead of eq. 1.6 we have

$$\frac{dw}{dt} = \mu_D R_{ON}\frac{w(D-w)}{D^3}i(t) \tag{1.10}$$

obtained by multiplying the right hand side of eq. 1.6 by $w(D-w)/D^2$ to take into account that the drift will start to slow down when $w$ is close to 0 and $D$. In this regime the resistive switching is almost bipolar: when $w$ is close to 0 and $D$ (meaning $w(D-w)/D^2 \approx 0$) it takes a huge charge or voltage to move $w$ and when an applied

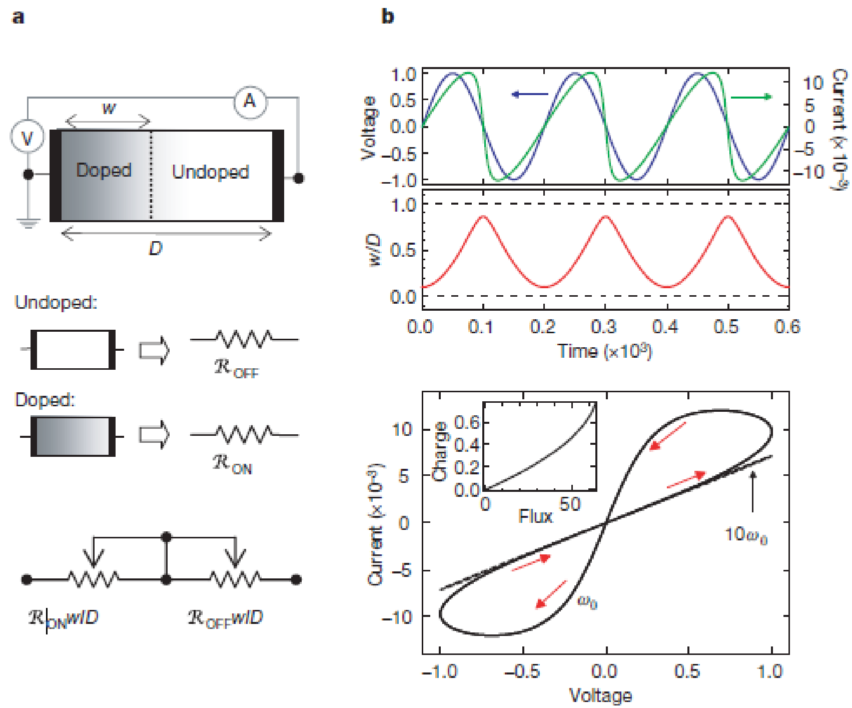


Figure 1.2: (a) Schematic of a memristive device and equivalent circuit (V is a voltmeter, A is an ammeter) (b) Simulation of the memristive device with $w(t) = w_0 \sin(\omega_0 t)$ with $\omega_0 = 2\pi D^2/\mu_V v_0$ and $R_{OFF}/R_{ON} = 160$.

bias is big enough to move $w$ away from these values, $w$ will immediately go from 0 to $D$ or vice versa, so we can approximately say that $w$ is either 0 or $D$. This behavior is seen in fig. 1.3 where the simulation with nonlinear ionic diffusion closely resembles the resistive switching of a typical $TiO_2$ device.
The fact that all resistive switching devices are in fact memristors has been claimed by Chua [7], also noting that the "fingerprint" of a memristor is the pinched hysteresis loop at $V = 0$, like the one seen in fig. 1.3.

## 1.2 Spintronic devices

Spintronics (spin transport electronics) is an exciting field of Solid State Physics conventionally born in 1988 with the discovery of the Giant Magnetoresitance, by A. Fert and P. Grunberg [1][2], who both won the Nobel Prize for Physics in 2007 because of this discovery. While the phenomenology of this effect is very simple (a thin magnetic multi-layer device under a sufficiently high magnetic field undergoes a *giant* change in resistance), this discovery spurred the creation of spin valves by IBM researcher S. Parkin, revolutionizing the world of hard disk drives, and opened

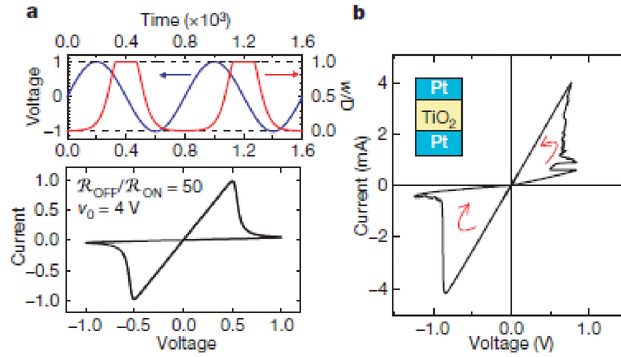


Figure 1.3: (a) Simulation of a memristive device with nonlinear contribution. (b) Resistive switching of an oxygen deficient $TiO_2$.

physicists to the idea of studying the effects of spin on transport of electrons.
Spintronics itself originates from the older magnetoelectronics, which studied the effect of magnetic field on electric current but ignoring the insights of quantum mechanics in the spin properties of electrons. A basic but important concepts in spintronics the Mott's two current model [3], which was used to explain the sudden increase in resistance of a ferromagnet as it is heated over the Curie temperature. In this model, electron currents can be completely separated in two distinct spin channels that have different transport properties. This model works when the basic assumption of no spin flip (due to magnons).
While this Mott's hypothesis would seem inconsequential in non-magnetic materials since electrons with spin up or spin down should act the same way, in ferromagnets one should be more careful. Since ferromagnets have a net magnetizations, electrons in these materials feel a magnetic field and their spins interact with this field with energy $-\mu \cdot \vec{B}$, where $\mu$ is the spin magnetic moment of the electron. This interaction causes a band splitting of $2\mu B$ (fig. 1.4) and so the Fermi level the density of states is different for the two spin states. If conduction takes places in an electron band with band splitting, causing different DOS at $E_F$, the current will be *spin-polarized*, meaning that an electron will have a 50/50 chance of having either spin and thus the whole current will have a net polarization.

### 1.2.1 Tunneling Magnetoresistance

The first spintronic effect was observed by Jullière in 1975 [4] but was largely ignored for two decades. Tunneling Magnetoresistance (TMR) is the change in resistance of a Magnetic Tunnel Junction (MTJ) represented in fig. 1.5, a device consisting of two ferromagnetic electrodes sandwiching a thin non-magnetic insulator. The first observed device to show TMR was a Co/Ge/Fe MTJ that, at 4.2K, showed a decrease of conductance of $\Delta G = 14\%$ between the states of parallel and antiparallel magneti-

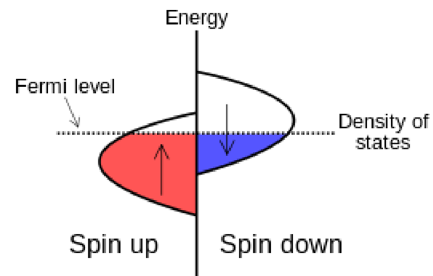


Figure 1.4: Example of a generic band splitting in a ferromagnet.

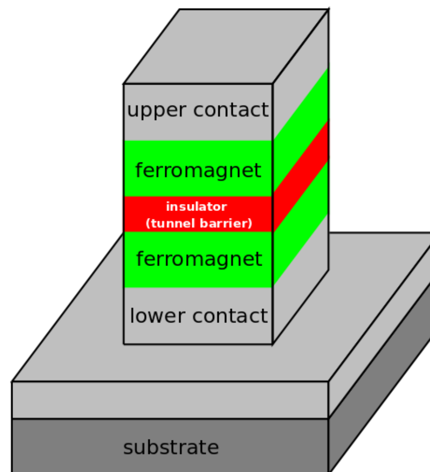


Figure 1.5: Schematic representation of a typical MTJ.

zation of the two electrodes. Knowing that the only possible way that electrons could pass from one electrode to the other was tunneling, Jullière produced a model assuming that the tunneling current is spin polarized to explain the variation of resistance. The spin polarization of the $i$-th electrode is defined as

$$P_i = \frac{N_{i\uparrow}(E_F) - N_{i\downarrow}(E_F)}{N_{i\uparrow}(E_F) + N_{i\downarrow}(E_F)}, \tag{1.11}$$

where $N_{i\sigma}$ is the density of states of the $i$-th electrode of the spin state $\sigma$, and simply is the expectation value of the spin of an electron in an electrode at the Fermi level $E_F$. Working with the two current model and assuming that the tunneling probability and thus the conductance for a certain spin channel is only proportional to the product of the density of states at the Fermi level of the two electrodes at a certain alignment of the magnetizations (i.e. electrons with different spins see the same energy barrier),

$$G_P = N_{1\uparrow}(E_F)N_{2\uparrow}(E_F) + N_{1\downarrow}(E_F)N_{2\downarrow}(E_F) \tag{1.12}$$

and

$$G_{AP} = N_{1\downarrow}(E_F)N_{2\uparrow}(E_F) + N_{1\uparrow}(E_F)N_{2\downarrow}(E_F). \tag{1.13}$$

This is graphically explained in fig. 1.6. The TMR ratio defined as

$$TMR = \frac{R_{AP} - R_P}{R_P} = \frac{G_P - G_{AP}}{G_{AP}} \tag{1.14}$$

and can be computed from eqs. 1.13 and 1.12, obtaining

$$TMR = \frac{2P_1P_2}{1 - P_1P_2}. \tag{1.15}$$

A trivial but important fact is that if even one electrode is unpolarized the $TMR$ ratio is 0. Another important thing to note is that the sign of the TMR ratio is negative only when the two electrode polarizations are of the opposite sign.
As long as there is no voltage applied to the junction, the tunneling process is symmetric and no current is (obviously) produced. When applying a voltage, electrons have a higher tunneling rate from the low voltage to the high voltage electrode and a current is produced.
The main failure of this model is that it doesn't account for the TMR dependence on the applied bias and on the choice of the barrier material. This will be shown in subsection 2.2.1 for LSMO/STO/Co MTJs.
In 1991, after the discovery of GMR, interest in TMR was rekindled by the discovery of a TMR of 2.7% at room temperature. These devices have been improved to the point of a TMR of 200% room temperature and now are commonly used as read-heads in hard-disk drives and in magnetic random-access memories (MRAM).

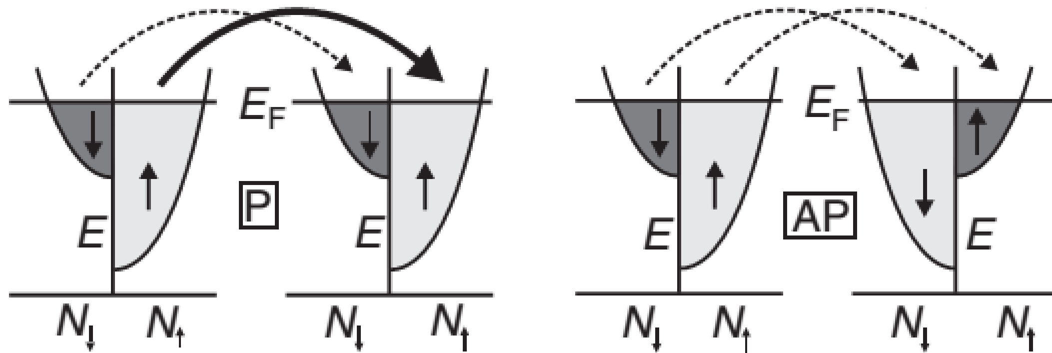


Figure 1.6: Graphical explanation of the TMR effect. The tunneling electrons are approximated as free electrons and the splitting between the two spin states is given by the magnetization of the electrode. The increase in resistance in the antiparallel state is because the majority ↑ electrons tunnel to the minority ↓ state and thus find less states available.

### 1.2.2 Giant magnetoresistance

While Jullière's experiments in the '70s did not attract much attention, during the '80s thin film technology was developing and a the Giant Magnetoresistance (GMR) was discovered in 1988 both by Fert's and Grunberg's groups [1][2]. This discovery attracted much more attention because of higher resistance ratios and because of and easier was to control the magnetization of the ferromagnetic layers.
In 1986 Grunberg discovered that two thin film of Fe separated by a Cr layer less than 1 nm thick are anti-ferromagnetically coupled. This is because of the RKKY (Ruderman-Kittel-Kasuya-Yosida) interaction, which is an indirect exchange mechanism between nuclear spins that interact with each other through a cloud of conduction electrons (that interact with the nuclei via hyperfine interaction). The exchange coupling between two nuclear spins separated by $\vec{R}$ takes the usual form

$$E(\vec{R}) = -J(\vec{R})\vec{S_1} \cdot \vec{S_2} \tag{1.16}$$

where $J(\vec{R})$ can take different signs as seen in fig. 1.7.
As a consequence, for certain thickness of the Cr layer in a Fe/Cr superlattice, the Fe layers are anti-ferromagnetically aligned at zero magnetic field. Applying a field aligns the magnetizations of the Fe layers and reduces the overall resistance of the superlattice in the configuration corresponding to the alignment of the magnetizations of the Fe layers. Figs. 1.8a and 1.8b show the first reports of GMR by the two groups.

The explanation brought forward by A. Fert is the dependence of the conduction of different spin states in the Fe layers: one spin state feels a resistivity lower than the other. In the anti-parallel configuration (no magnetic field applied) each spin states

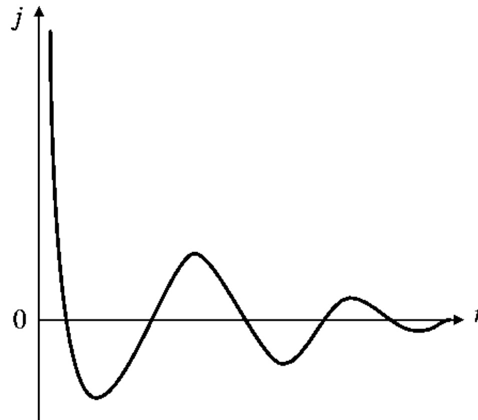


Figure 1.7: Coupling constant of the RKKY interaction mechanism. At small distances the coupling is ferromagnetic.

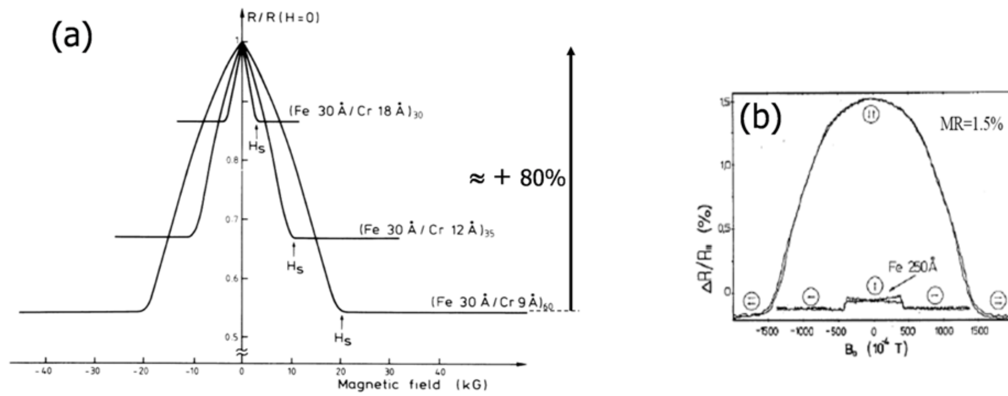


Figure 1.8: (a) GMR of a Fe/Cr(001) superlattice; the maximum GMR ratio obtained was 80% [1] (b) GMR of a Fe/Cr/Fe trilayer; the maximum GMR ratio obtained was 1.5% [2]

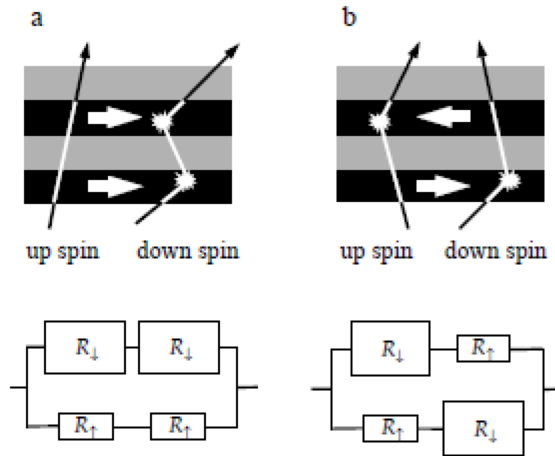


Figure 1.9: Schematic interpretation of the effect of spin dependence of electrical conductivity on the resistance in different magnetization states and equivalent circuit of the parallel resistor model.

feels low resistivity in one layer and high resistivity in the other and overall the resistance of each channel is the same. In the parallel configuration one of the spin states feels lower conductivity in both layers while the other feel high conductivity in both; the latter channel thus has lower resistance and causes a short-circuit lowering the resistance of the whole device compared to the anti-parallel case.

The reason different spin channels feel different resistance is due to the spin-dependent scattering mechanisms that Mott hypothesized in 1939 and that Fert observed in 1968. For a spin $\sigma$ with effective mass $m_\sigma$ and DOS $n(E_F)$, the resistivity is

$$\rho_\sigma = \frac{m_\sigma}{n_\sigma(E_F)e^2\tau_\sigma}, \tag{1.17}$$

where $\tau_\sigma$ is the relaxation time that can be evaluated as

$$\tau_\sigma^{-1} = |V_\sigma|^2 n(E_F) \tag{1.18}$$

with $V_\sigma$ the scattering potential and $n(E_F)$ the density of states of the the final scattering state. In transition metals like cobalt, conduction is carried out by the "light" $3s$ electrons and their strongest scattering is towards the "heavier" $3d$ electrons. Since the $3d$ band is split, the two spin channels feel different relaxation times and thus different resistivities. In cobalt, the $3d_\uparrow$ is below the Fermi energy and so $n_{\sigma\uparrow} \approx 0$, giving the $\downarrow$ channel a much lower resistance than the $\uparrow$ channel.

While the first experimental observations of GMR effect where is current-in-plane (CIP) geometries, I will focus on the current-perpendicular-to-plane (CPP) geometry since it is currently the most common. A straightforward explanation is the parallel resistor model, shown in fig. 1.9, which works well for trilayers of FM/NM/FM. In

the antiparellel configuration, both spin channels will be majority ($\downarrow$) in on FM and minority ($\uparrow$) in the other, so the total resistance is

$$R_{AP} = \frac{R_\uparrow + R_\downarrow}{2}. \tag{1.19}$$

In the parallel configuration, the majority spin channel is the same in both FMs, leading to the short-circuit effect. In this case the total resistance is

$$R_P = \frac{2R_\uparrow R_\downarrow}{R_\uparrow + R_\downarrow}. \tag{1.20}$$

The GMR ratio is defined as the TMR

$$GMR = \frac{R_{AP} - R_P}{R_P} \tag{1.21}$$

and in this parallel resistor model

$$GMR = \frac{(\alpha - 1)^2}{4\alpha} \tag{1.22}$$

where $\alpha = R_\downarrow / R_\uparrow$ is the spin asymmetry parameter. As with TMR, GMR exists entirely because of the spin splitting of the electron bands.
The parallel resistor model works with a few basic assumptions. First of all, it is assumed that the ferroelectric electrodes are completely identical (material and thickness) and that the resistivity of the space is not relevant. If the latter assumption is not true, the $GMR$ can be modified as

$$GMR = \frac{(\alpha - 1)^2}{4(\alpha + pd_{NM}/d_{FM})(1 + pd_{NM}/d_{FM})} \tag{1.23}$$

where $p = \rho_{NM}/\rho_\uparrow$. Since the GMR decreases with increasing $pd_{NM}/d_{FM}$, it is important that the thickness and the resistance of the nonmagnetic spacing be small.
In many cases, negative GMR is measured when the ferromagnetic layers are of different materials; this also can be interpreted with this simple model. In this case the $GMR$ becomes

$$GMR = \frac{(\alpha_1 - 1)(\alpha_2 - 1)}{\alpha_1(1 + q) + \alpha_2(1 + q^{-1})} \tag{1.24}$$

where $q = \rho_{1\uparrow}/\rho_{2\uparrow}$ and $\alpha_1$ and $\alpha_2$ are the spin asymmetry parameters of the two FM layers. Similarly to the TMR effect where negative TMR ratios are observed when the polarizations of the electrodes have opposite signs, here negative GMR ratios are possible when $\alpha_1 > 1$ and $\alpha_2 < 1$ or vice versa. From eqs. 1.17 and 1.18, we have

$$\rho_\sigma \propto n(E_F)$$

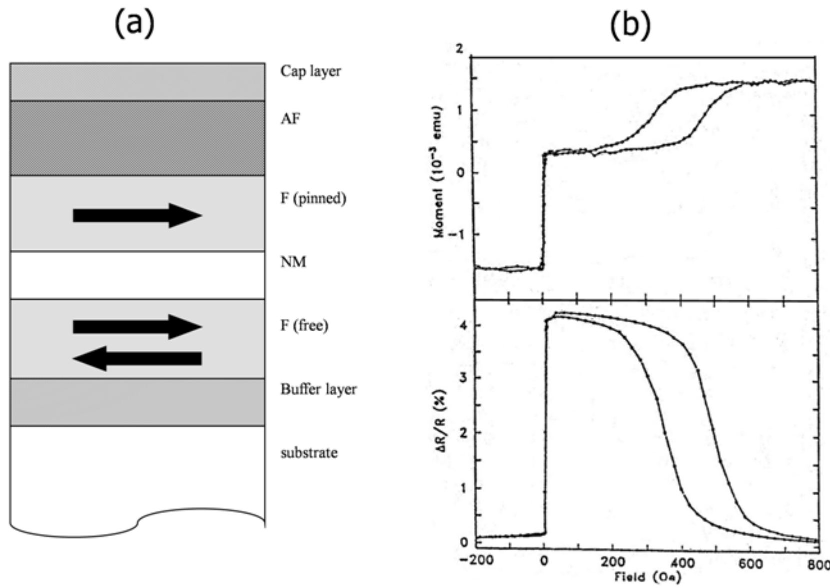


Figure 1.10: (a) Schematic of a spin valve device (b) Magnetization and magnetoresistance loops of a NiFe(6 nm)/Cu(2.2 nm)/NiFe(4 nm)/FeMn(7 nm) device. [5]

and thus, like in TMR, negative GMRs are possible the the two electrodes have different spin splitting.

**Spin valves**

To observe a GMR effect it is necessary to be able to switch from the anti-parallel configuration to the parallel by applying magnetic fields. In the first GMR experiments, this was obtained using the RKKY coupling between ferromagnetic layers but it is not necessarily the most useful method. Another option is the spin valve (SV) device [5], which is now used in most spintronics experiments. These devices, similar to the ones used to first observe TMR, are thin film stacks of three layers; the first is a ferromagnet coupled to an anti-ferromagnet or ferrimagnet to obtain a pinning of its magnetization, the second is the non-magnetic layers and the third is the other ferromagnetic electrode. This way, the magnetization of the fist electrode is pinned and an applied magnetic field only modifies the magnetization of the second layer. The behavior of a typical SV is in fig. 1.10

Another option is the pseudo spin valve (although normally called spin valve) where the electrodes are made of materials with different coercive fields. This way, when at zero field the magnetizations are parallel, applying a magnetic field in the opposite directions first reverses the magnetization of the softest material, obtaining an antiparallel configuration, and only at higher field reverses the magnetization of the hardest material, obtaining a parallel magnetization again. This behavior is described in fig. 1.11. These devices are the ones studied in this thesis.

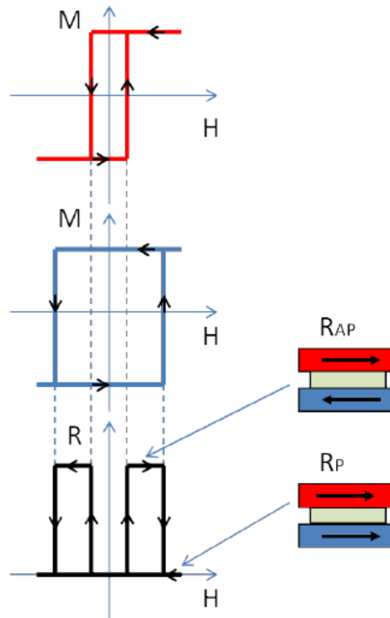


Figure 1.11: Schematic representation of electrode hysteresis loop and MR curve of a spin valve device. At high magnetic field the top electrode (red line) and the bottom electrode (blue line) magnetic moments are aligned and the device is set in the low resistance parallel configuration $R_P$ . When the top electrode magnetization is reversed the device is switched in a resistance state antiparallel configuration $R_{AP}$. Finally, when the bottom electrode moment is also reversed, the parallel configuration is restored. Pictured is also the correspondence between the coercitivies of the electrode and the increase and decrease of the resistance of the device when switching from parallel to antiparallel and vice versa.

Some materials that have been recently studied as junctions in spin valves and MTJs include MgO, $SrTiO_3$, $AlO_x$ and organic semiconductors such as Alq3.

## 1.3 Memristive Spin Valves

As I previously pointed out, devices that are both memristors and spin valves are interesting for fundamental and applied physics. In this section I report two experiments, both showing the applications of such devices and how knowledge of one mechanisms transports to the other.

### 1.3.1 Memristive organic spin valves

Interest in memristors has sparked since the publication of Strukov et al.'s article [8], as these devices can be applied in ultradense memories, logic gates and neuromorphic computing. A few years later, while working on spin valves with organic semiconductor junctions, Prezioso et al. [10] [11] reported an $La_{0.7}Sr_{0.3}MnO_3/Alq3/AlO_x/Co$

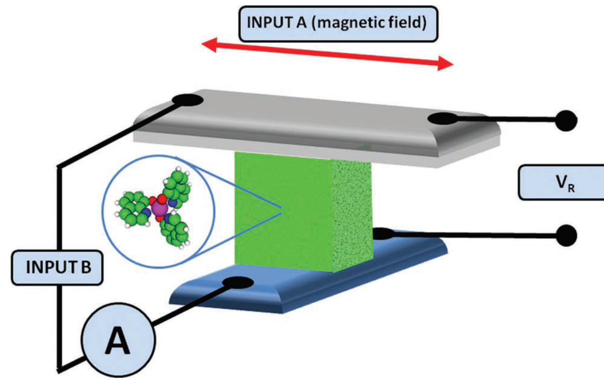


Figure 1.12: Schematic of the multifunctional device investigated by Prezioso et al. [11]. From top to bottom: a Co magnetic electrode, a thin $AlO_x$ barrier, Alq3 organic semicondutor and a $La_{0.7}Sr_{0.3}MnO_3$ electrode. The device was measured in four contact mode by applying a bias voltage at INPUT B, reading the current generated with an ammeter A an measuring the voltage $V_R$ produced in the two remaining contacts. The resistance is defined as $R = V_R/A$. The magnetoresistance is measured by applying a magnetic field parallel to the Co electrode.

thin film device showing both spin valve and resistive switching effects witch various different resistive states. Furthermore, the spin valve magnetoresistance (SVMR) was shown to be controlled by the resistive state of the device, disappearing at the highest resistance.

A schematic of the device is in fig. 1.12. The different resistive states and their magnetoresistance are shown in fig. 1.13. The different resistive states were non-volatile (a necessary condition for a memristor). Based on this interplay between between magnetoresistance and resistive switching, it is possible to create a logic gate based on this device.

A universal Boolean logic gate is a logic gate that is able to reproduce the behavior of every other logic gate. One of the universal gates is the material implication (IMP) gate, which is simply the truth table of the statement $A \to B$. To realize this gate with such a device, the input A's 0 value is assigned to the saturation magnetic field of 3 kOe while the 1 value is the field that creates an antiparallel configuration (see fig. 1.13c). Input B's 0 value is assigned to the programming bias leading to the lowest resistance state (that also has the highest SVMR percentage) and the 1 value is assigned to the programming bias leading to the highest resistance state (that has no spin valve effect). The output is read by applying a -0.1 V bias and by measuring the current; considering that the lowest possible resistance (and thus highest possible current) is in the low resistance state with the electrodes in the antiparallel configuration (since the SVMR is negative), this current value is assigned to the 0 value while lower currents are assigned to the 1 value. This is obtained by setting a current threshold: if the current exceeds this threshold the output is 0, otherwise it is 1. The

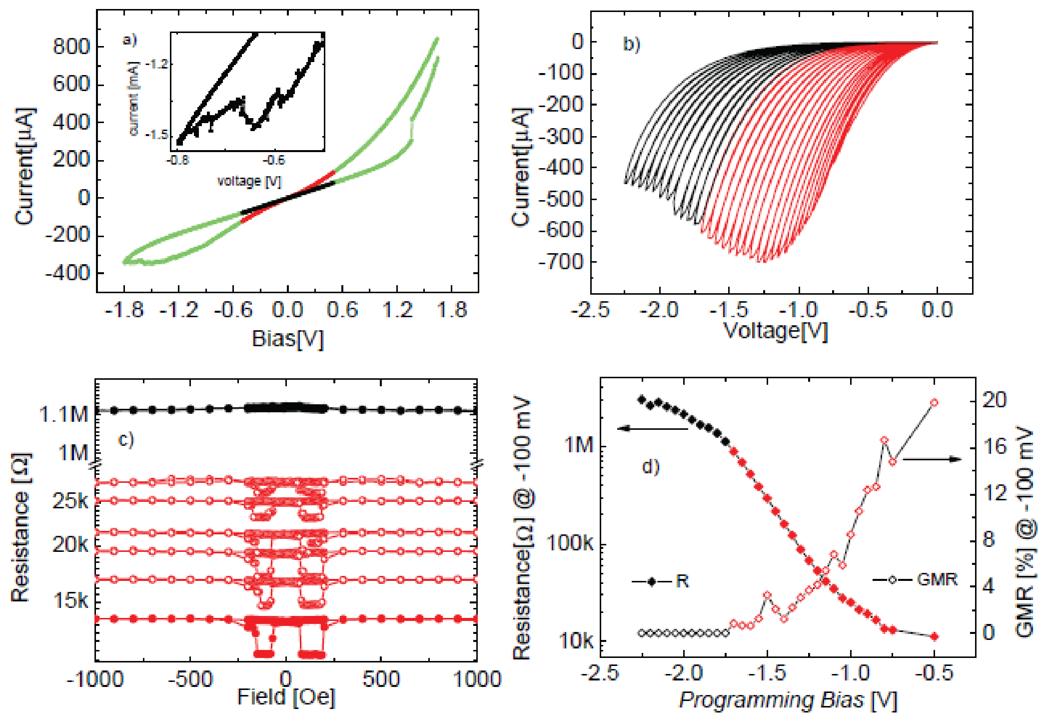


Figure 1.13: $I-V$ and magnetoresistance measurements from a device (fig. 1.12) with a 200 nm thick Alq3 layer. a) Resistive switching hysteresis $I-V$ curve typical of a memristor. Note the different resistance around $V = 0$ for the two different states. b) 32 different resistive states produced by reaching increasingly higher negative programming biases. In red are the curves that produced states that showed SVMR at -0.1 V. c) Magnetoresistance curves taken at -0.1 V of the different resistive states. d) Resistance and SVMR of the different states.

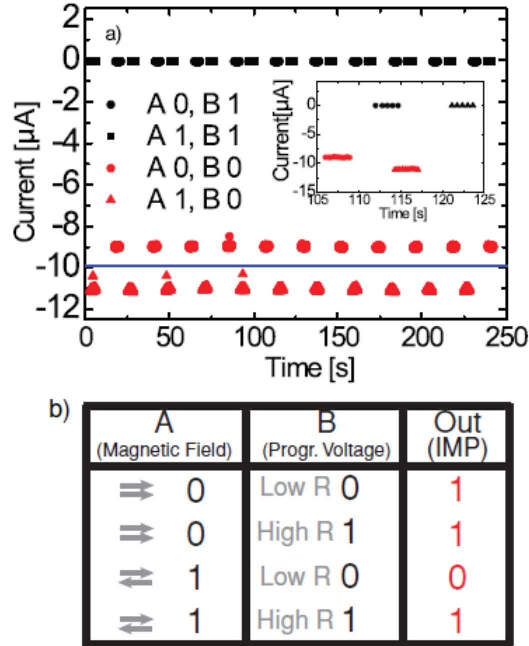


| A (Magnetic Field) | B (Progr. Voltage) | Out (IMP) |
|---|---|---|
| 0 | Low R 0 | 1 |
| 0 | High R 1 | 1 |
| 1 | Low R 0 | 0 |
| 1 | High R 1 | 1 |

Figure 1.14: a) Logical outputs of the device operating as an IMP gate after setting the inputs. The straight line is the threshold over which the current produces an 0 output value. b) Truth table of the device.

device's operation as an IMP logic gate is shown in fig. 1.14.

There are two main advantages for using such a device as an universal IMP gate. The first is that with traditional memristors an universal IMP gate was only possible with two different memristor devices. The second is that, since one of the inputs is a magnetic field, it can be applied to a whole arrays of gates.

Many theories have been brought forward to explain resistive switching in devices with $Alq_3$ and other organic semiconductors but no definite proof has been found for every one of them. A phenomenological model brought forward by Rozenberg et al. is commonly used to explain. According to this model, the $Alq_3$ barrier contains metallic domains (dopants, vacancies, metallic clusters) which can be grouped in top electrode, bottom electrode and middle domains, assuming that the middle domains vastly outnumber the other electrode domains. A representation of this structure is in fig. 1.15a. Applying a high enough voltage to move charges into the injecting electrode domains thus trapping them.

Using a modified Jullière model to take into account spin depolarization, the spin valve magnetoresistance (SVMR) is

$$SVMR = \frac{P_1 P_2 e^{-\frac{\tau_t}{\tau_s}}}{1 - P_1 P_2 e^{-\frac{\tau_t}{\tau_s}}} \tag{1.25}$$

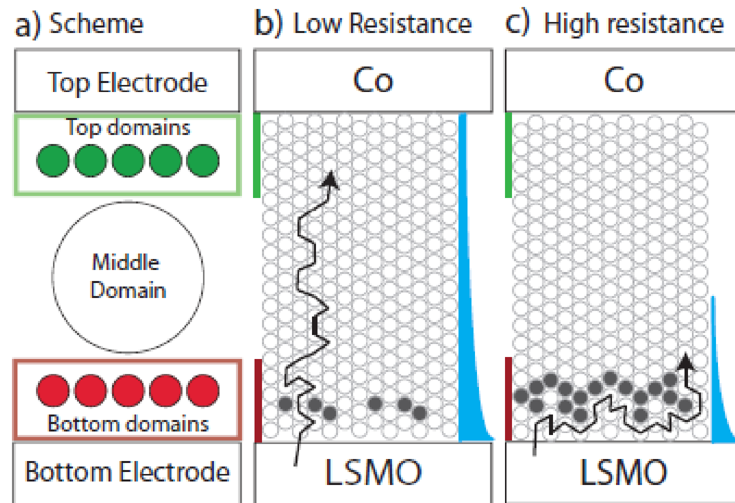


Figure 1.15: a) Metallic domains inside the $Alq_3$ junction b) In low resistance states, no or few domains are trapped and thus the spin diffusion length is low; on the right side the blue bar indicates the local spin polarization of the current c) In high resistance states, many domains are trapped and thus the spin diffusion length is low; on the right side the blue bar indicates the local spin polarization of the current.

where $P_1$ and $P_2$ are the polarizations of the electrodes, $\tau_t$ the transit time of the spin carrier and $\tau_s$ the spin coherence time. As domains are trapped, the spin diffusion length increases and thus the polarization of the current arriving at the top (analyzer) electrode decreases.

### 1.3.2 Memristive $TaO_x$ spin valves

A second memristor with spin valve effect was reported by Jang et al. [12] in 2012. In their article they reported a ferromagnet/oxide/ferromagnet vertical device that feature resistive switching and magnetoresistance in only one resistive state, at room temperature. The device is a Co(60 nm)/$TaO_x$(16 nm)/Cu(5 nm)/Py(Supermalloy, 60 nm); the supermalloy layer is a soft ferromagnet while cobalt is a hard ferromagnet. $I - V$ curves were taken at room temperature and feature resistive switching with an OFF/ON ratio of $10^5$ (fig. 1.16). Resistive switching in Pt/$Ta_2O_5$/Cu had already been attributed to copper filaments created and annihilated by bias voltages and these filaments are typically of a diameter of 10 nm.
MR measurements were taken at a temperature of 77 K and are pictured in fig. 1.17. The magnetic field was swept from -25 mT to 25 mT so that only the magnetization of the Py layer is reversed. The MR of the ON states features a small but clear 0.3% spin valve signal while the OFF state features no spin valve effect. This behavior of the magnetoresistance indicates that spin transport happens only in the copper

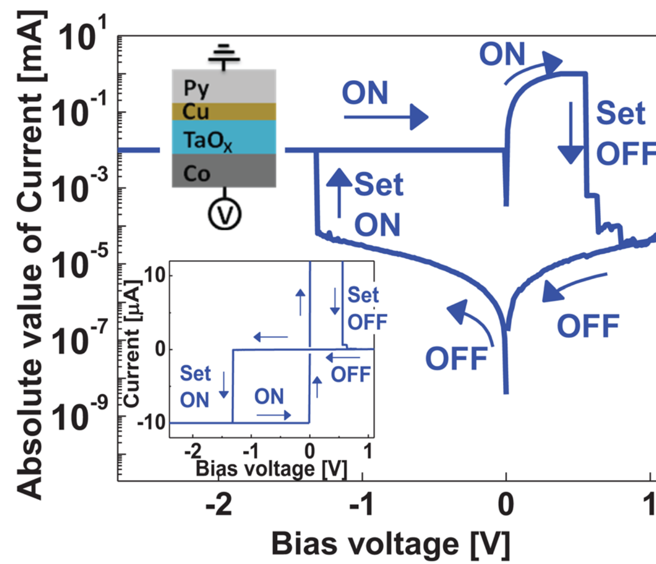


Figure 1.16: $I-V$ double-logarithmic curve of a $TaO_x$ junction pictured in the top inset, featuring resistive switching. In the bottom inset is the zoomed linear curve

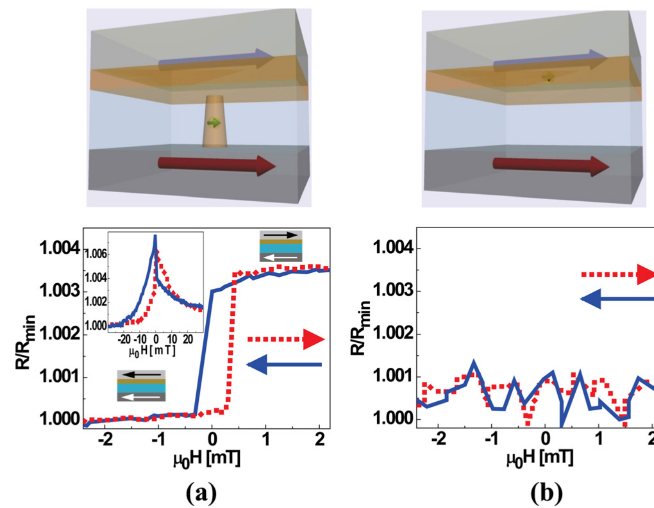


Figure 1.17: Magnetoresistive measurements of the $Co/TaO_x/Cu/Py$ in both resistive states, pictured above. The magnetic field applied was lower than the coercive field of the copper layer so that the MR curve resembling the soft hysteric behavior of the supermalloy layer clearly implies the dependence of the resistance on the magnetization of the supermalloy layer, and thus spin transport in the device.

filaments formed in the ON states of the devices. Another important finding that the resistance of the ON state is lower at 77 K than at room temperature indicating a metal-like conduction while the OFF state at 77 K has a higher resistance than at room temperature, indicating an insulating-like conduction.

# Chapter 2

# Oxides for memristive and spintronic devices

## 2.1 LSMO

Perovskite manganites are a class of materials widely studied for their colossal magnetoresistance (CMR) and, more recently, for their near-100% spin current polarization. These materials are $R_{1-x}M_xMnO_3$ ($0 < x < 1$), where R is a rare earth material (La, Pr, Ce) and M is an alkaline earth metal (Sr, Ca) and they take their name from their crystal structure described in fig. 2.1. These materials also feature rich phase transitions with different compositions. In this thesis I will concentrate specifically on $La_{0.7}Sr_{0.3}MnO_3$ (LSMO).
Interest in these materials sparked in the '50s with the discovery of CMR but interest faded as the field needed to obtain this effect were too great. In the decades, as spintronics began to develop, this class of materials has been studied for their peculiar characteristic of being a half-metal, meaning that one spin state has a metallic behavior while the other feels a band gap and thus is insulating. This means that at the Fermi level there is only one spin state with a non-zero density of states and so the current is nearly 100% spin polarized. Recent experiments [13] have shown that the bulk polarization is actually lower and that the high current polarization is actually due to the different mobilities of the minority and majority spins.

### 2.1.1 Jahn Teller rffect and rxchange interaction

It is interesting to study the 3d valance electrons of manganese atoms, contained inside the oxygen octahedron. First of all, since the octahedron is a non-uniform distribution of positive charge there is a first splitting of the 3d levels described in fig. 2.3. The split energy levels are represented in fig. 2.2; in this case the atom in the

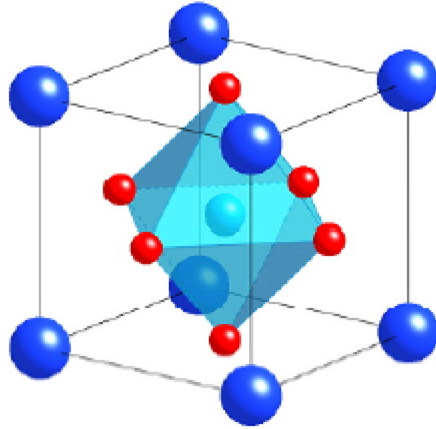

Figure 2.1: Perovskite crystal structure. In a $R_{1-x}M_xMnO_3$ perovskite manganite, the corner atoms are Mn atoms, the body centered atoms are dopants (R and M) and the face centered atoms are O. This crystal structure takes the name from the mineral $CaTiO_3$ called perovskite.

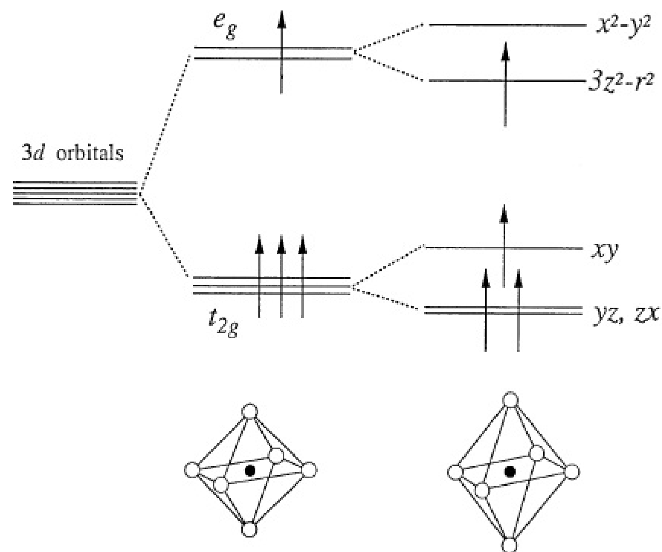


Figure 2.2: Jahn-Teller effect: splitting of the energy level of an atom inside an octahedron of oxygen due to the distortion of the latter.

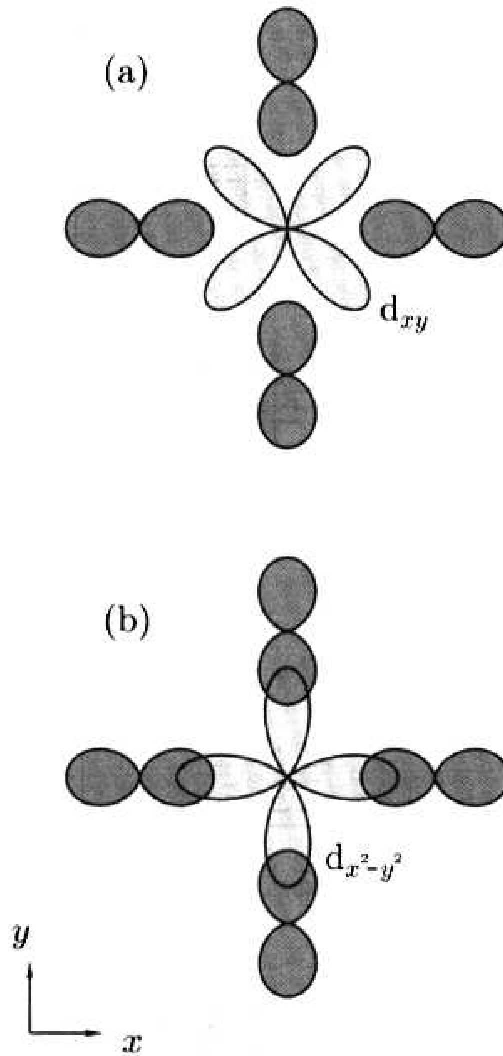


Figure 2.3: Representation of how the crystalline environment influences electron energy levels. $d_{xy}$ electrons have lower overlap with the neighboring orbitals of the oxygen atoms and thus have lower energies than $d_{x^2-y^2}$ atoms that have higher overlap with the neighboring oxygen orbitals.

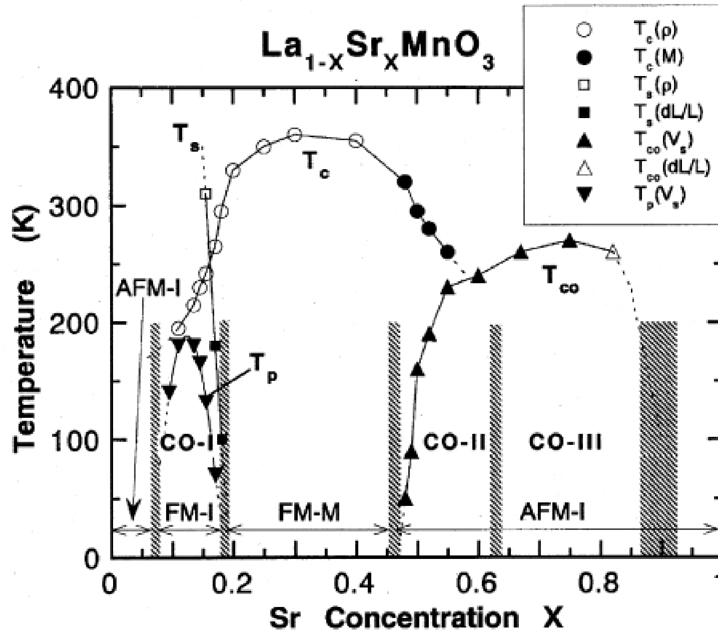


Figure 2.4: LSMO phase diagram showing transport and magnetic properties as a function of Sr concentration $x$. In the range $0,175 < x < 0,45$ the compound becomes ferromagnetic and metallic under a Curie temperature, which has a maximum at $x = 0.3$.

center of the octahedron has four valence electrons and the electronic configuration is in the weak crystal field case, meaning that is energetically convenient to place the fourth electron in the higher energy $e_g$ orbital since the energy difference is lower than the Coulomb energy required to pair two different electrons in the same orbital.
A second splitting of the energy levels is the Jahn-Teller effect, which is the distortion of the lattice since it is energetically convenient for the atoms inside an octahedron of oxygens to be in a distorted environment. The stretching of the octahedron splits the $e_g$ and $t_{2g}$ further, as described in fig. 2.2. If the atom has four valence electrons, this is energetically convenient since the $e_g$ electron lowers its energy and thus the octahedron distorts itself; if the atom has only three valence electrons the Jahn-Teller effect is not present since there is no lowered energy to cause the distortion.

### 2.1.2 Doping and exchange properties

Most interesting properties of $La_{1-x}Sr_xMnO_3$ come from the fact that Mn atoms exists in two different oxidation states because of the rich phase transitions due to doping. $LaMnO_3$ contains only $Mn^{3+}$ with a $3d^4$ valence band (a Jahn-Teller atom). The Mn atoms are far away and the only possible interaction between Mn valence electrons is through super exchange: the Mn $e_g$ electron distorts the oxygen's orbitals attracting the electron with opposite spin and distances the opposite spin electron,

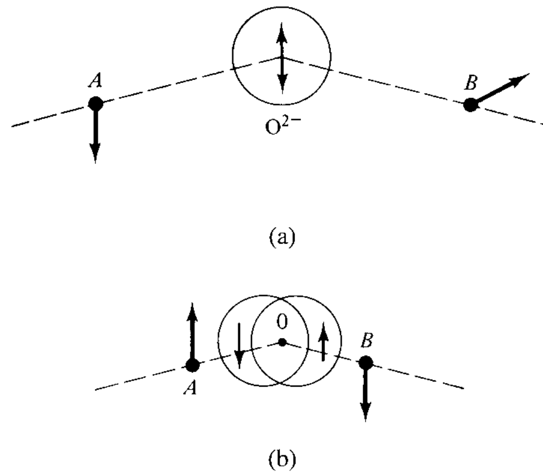


Figure 2.5: Super exchange interaction: (a) if the atoms in the A and B positions are far away enough the electron cloud is unaltered; (b) if A and B are closer the electron cloud deforms causing an antiferromagnetic exchange force between the atoms in A and B.

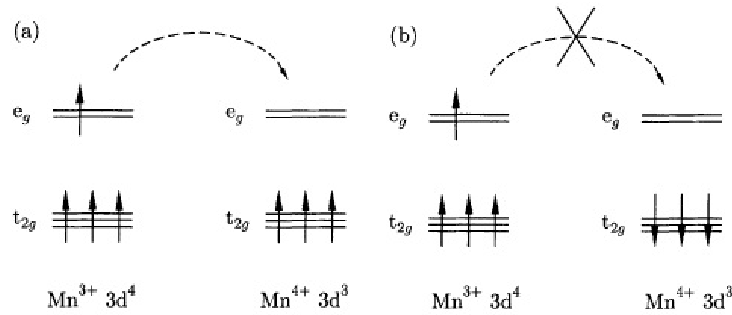


Figure 2.6: Schematic representation of double exchange mechanism. The $e_g$ electron hopping from $Mn^{3+}$ to $Mn^{4+}$ ion is allowed only when $t_{2g}$ spins are parallel to its spin due to Hund's first rule.

inducing an opposite spin in an adjacent Mn atom (see fig. 2.5. The manganite is thus insulating since no electron conduction can take place and is also antiferromagnetic because of the interaction. With a Sr concentration of $0 \leq x \leq 0.175$ this also holds.

Because of La and Sr doping, there is a fraction $x$ of $Mn^{4+}$ and a fraction $1 - x$ of $Mn^{3+}$. With a sufficient concentration of both oxidation, superexchange is no longer relevant since it relies on the two Mn atoms separated by an oxygen to be in the same oxidation state. In this case one Mn ion has three electrons in the lower $t_{2g}$ energy level while the other also have on in the $e_g$ state. Because of Hund interaction, if the $t_{2g}$ electrons of the two atoms are ferromagnetically aligned the $e_g$ electron can freely hop to the neighboring atom. If the Mn atoms are antiferromagnetically aligned the $e_g$ electron feels a very high energy barrier because of Hund interaction and the material is a conducting ferromagnet. Since the ferromagnetic alignment lowers the

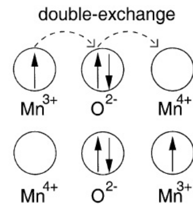


Figure 2.7: The role of oxygen in double exchange.

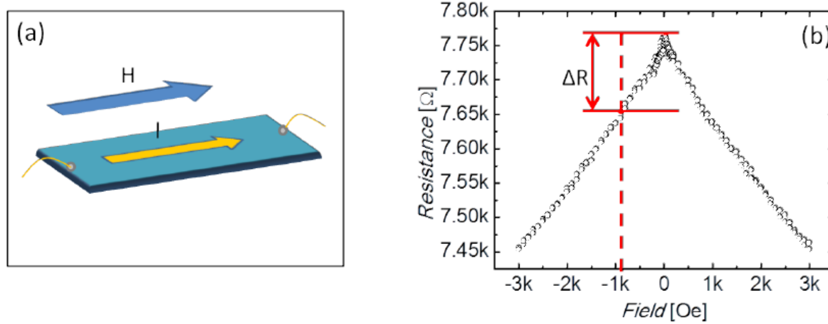


Figure 2.8: (a) Schematic representation of an LSMO stripe connected in a two point configuration. The magnetic field H is applied parallel the current I. (b) CMR signal measured on a 9 nm thick LSMO film at 100 K. The CMR signal amplitude is here defined as $CMR = \Delta R/R$, where $\Delta R = R(0) - R(800\text{Oe})$ as indicated by the red lines.

kinetic energies of the $e_g$ electrons, it is energetically convenient for the manganite to be ferromagnetic and metallic. This is called double exchange (see fig. 2.6 and 2.7) since the hopping process is through an oxygen atom between the two Mn atoms.
At high enough temperatures thermal fluctuations dominate and destroy the ferromagnetic alignment of the $t_{2g}$ electrons, transforming the material to paramagnetic at a Curie temperature $T_C$ and thus insulating.
The situation is actually more complicated because the carriers interact with phonons because of Jahn-Teller effect. The strong electron-phonon coupling in this systems implies that the carriers are actually polarons above $T_C$, i.e. electrons accompanied by a large lattice distortion. These polarons are magnetic and are self-trapped in the lattice. The transition to the magnetic state can be regarded as an unbinding of the trapped polarons.

### 2.1.3 Magnetoresistance

Because of the double exchange effect, the higher the magnetic ordering of the electrons in the $t_{2g}$ valence state the LSMO the lower is its resistance. Thus if we apply a magnetic field parallel to the magnetization of the LSMO we increase the

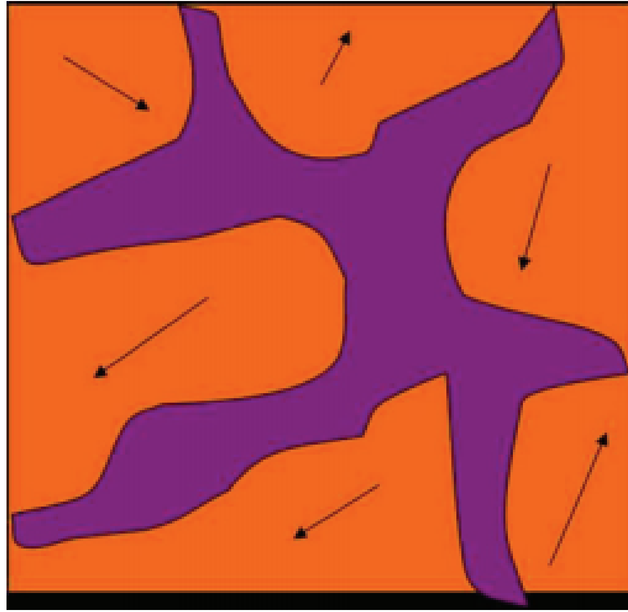

Figure 2.9: Ferromagnetic clusters in LSMO and thei magnetization (orange). In purple are the insulating islands.

net magnetization of the electrons in the $t_{2g}$ state and we lower its resistance. This effect is called *colossal magnetoresistance* and is shown fig. 2.8 where we can also observe anisotropic magnetoresistance (AMR). CMR scales linearly with the applying magnetic field with field up to a few kOe and can reach up to 100%. From fig. 2.10 we can see that the CMR effect has a clear peak slightly before the $T_C$ (which is actually defined as the linear extrapolation to zero of the MR segment to the right of the peak) and then goes to zero at $T = 0$. The exact explanation of both CMR (and AMR) is yet to be discovered but it was recently proposed that phase transition happens through nucleation of ferromagnetic clusters while the rest of the material is insulating (fig. 2.9) that become bigger and bigger until the material becomes entirely ferromagnetically.

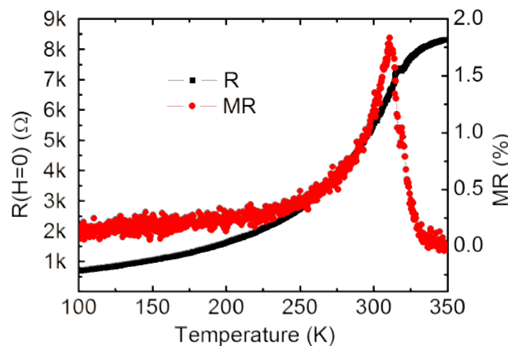


Figure 2.10: Measured resistance and magnetoresistance $(R(0) - R(800\text{Oe})/R(0))$ of a 9 nm LSMO strip.

Electrons can travel easily through clusters with parallel magnetization and less easily in clusters with other magnetizations. Applying an external magnetic field changes the orientation of these clusters and move domain walls, gradually transforming the material to a metallic, ferromagnetic state with a well defined magnetization. In this picture, applying a magnetic field induces a phase transition from an insulating to a metallic state and the CMR, the reduction of resistance with applied field, is simply the signature of this transition.

## 2.2 STO

$SrTiO_3$ is another perovskite oxide with strong paraelectric and insulating properties and also features superconductivity al low temperatures. It features an electric constant of 300 at room temperature and 2000 at 100K, reaching $10^4$ at low temperatures while approaching a ferroelectric phase transition. The material is still always paraelectric because of quantum fluctuations. Because of the high dielectric constant, it is commercially available in high voltage capacitors. It is also used as a substrate for oxide thin films, especially oxide superconductors. Recently, STO has been studied for its resistive switching properties because of the inherent property of the oxide to harbor oxygen vacancies in point defects and the redox processes along dislocations in the Ti sublattice of the perovskite structure.

### 2.2.1 STO spintronic devices

In 1999 De Teresa et al. [15] reported an LSMO/STO (2.5 nm)/Co MTJ featuring an inverse TMR effect (i.e. the resistance is lower in the antiparallel configuration) of 50%. Since the polarization of LSMO is positive, according to Jullière's TMR formula (eq. 1.15), the inverse TMR is a signature of negative polarization. While Co features positive polarization with in many MTJ, for example with $Al_2O_3$ [17], the reason Co has negative polarization in this MTJ is because of the different hybridization of the interface with STO. Due to $d-d$ electron bonding with Ti and Sr at the interface and since $3d$ Co electrons have higher DOS of minority states, the predominance the $d-d$ bonding lowers the polarization of the tunneling electrodes to the point of reversing it [18].

In fig. 2.12 we can see the TMR for different biases. At positive biases the TMR lowers to the point that it becomes positive. The maximum of the positive TMR is 1.5% at 1.15 V and the maximum of inverse TMR is 50% at -0.4 V. To interpret this, we can consider the relative position of the LSMO and 3d Co electrons with these biases (fig. 2.13.). This is because, since applying a bias changes the relative position of the DOS of the two electrode, electrons do not tunnel from the Fermi level of one electrode to the we need to consider all of the possible tunneling routes from the two

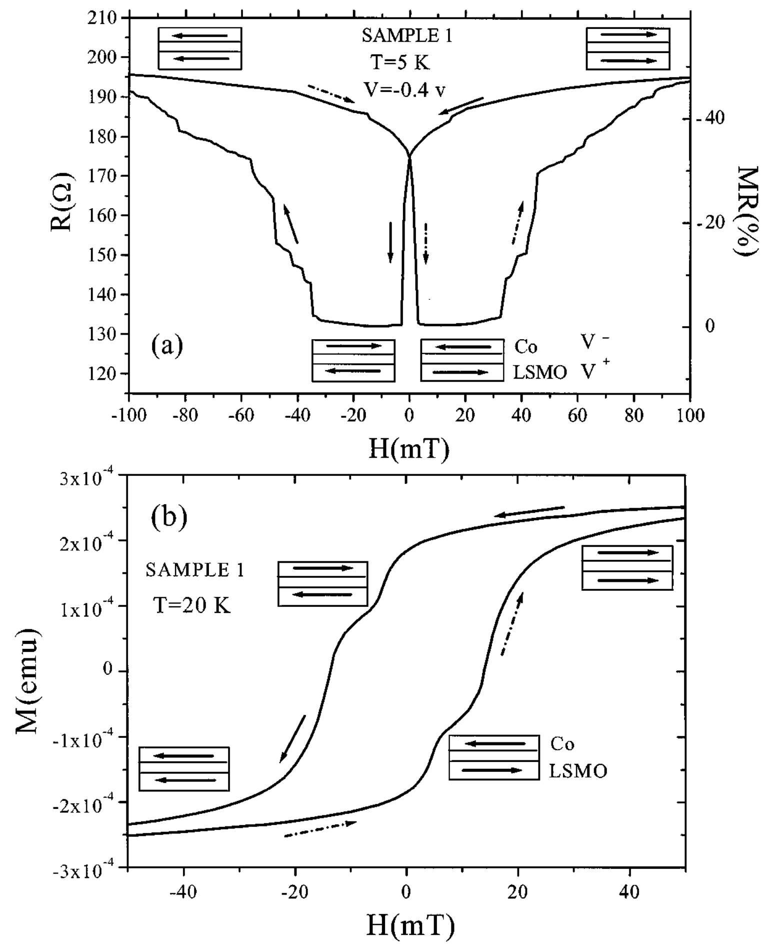


Figure 2.11: (a) Resistance versus applied magnetic field for the LSMO/STO (2.5 nm)/Co MTJ at 5 K and -0.4 V. (b) Magnetization of the device versus applied magnetic field [15].

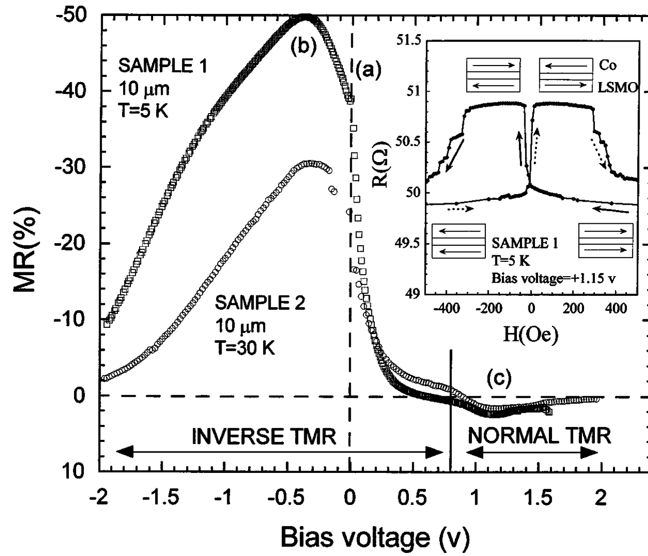


Figure 2.12: Measured TMR versus applied bias for the LSMO/STO (2.5 nm)/Co MTJ at 4 K. [15].

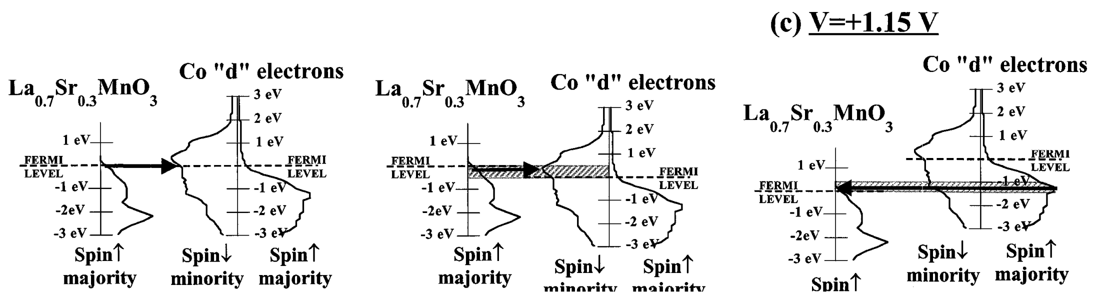


Figure 2.13: Relative position of the DOS of the LSMO and Co (3d) electrons for different biases: -0,4 V corresponds to the maximum of the inverse TMR and 1.15 corresponds to the maximum of positive TMR (fig. 2.12). The arrows correspond to the most probable route of tunneling. [15]

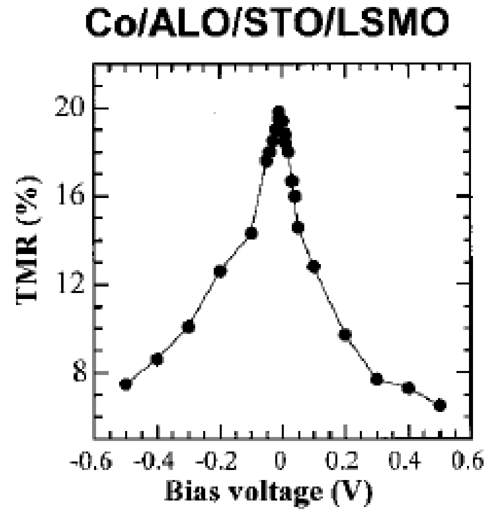


Figure 2.14: Bias dependence of TMR of a Co/$Al_2O_3$/STO/LSMO. [16]

shifted DOS.

At -0.4 V the inverse TMR is maximum because the electrons in the Fermi level of the LSMO can tunnel to the maximum of the $\downarrow$ minority 3d electrons of Co, which is 0.4 V higher than the 3d Co Fermi level. The high TMR is guaranteed by the low DOS of minority electrons at that energy. At 1.15 V Fermi level of the the electrons in the maximum DOS of $\uparrow$ majority electrons can tunnel to the Fermi level of the LSMO. Since at that energy the DOS of the minority electrons is lower than that of the majority, the TMR is positive but it is not high in absolute value because of the high competition between the two channels.

With Co/$Al_2O_3$ the situation is different: it has been computed from first principles [18] that the $Al_2O_3$ hybridizes forming $sp-d$ bonds with the Al atoms that facilitate tunneling for the positively polarized $s$ electrons and creates a tunneling barrier for the negatively polarized $d$ electrons. To confirm the dependence of the TMR sign on the interface effect, a Co/$Al_2O_3$/STO/LSMO were fabricated [16]. These device feature entirely positive TMR (fig. 2.14), consistent with tunneling from the positively polarized $s$ electrons.

These interesting finding show the importance of considering surface states when studying the tunneling of electrons and are of utmost importance for the work presented in this thesis.

### 2.2.2 STO memristors

Memristors made of STO junctions have been reported for Fe-doped STO [43], single crystal STO [42], policrystalline STO (which was used to realize an IMP circuit) [44], and amorphous STO [19]. Of these I will focus of the latter since it is similar to

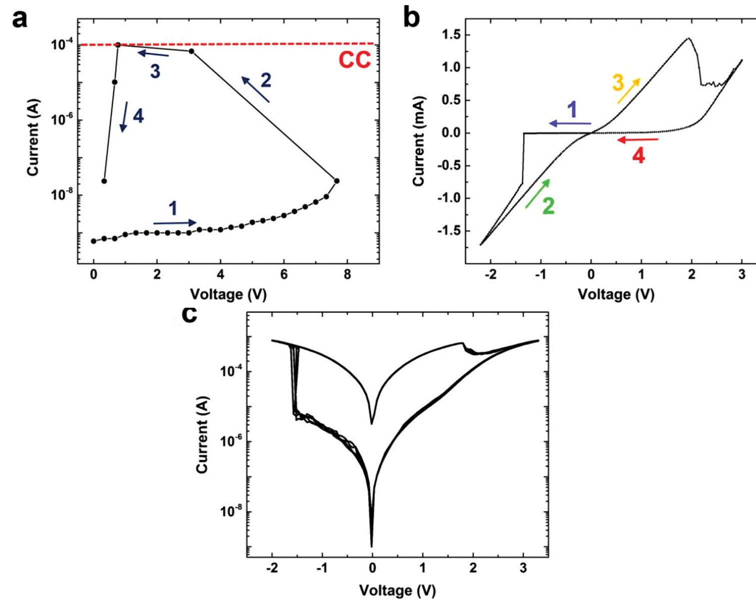


Figure 2.15: a) Typical electroforming sweep in positive polarity for a- STO junction. b) Typical bipolar switching behavior of a- STO junction. c) Bipolar switching performance of a single cell over $10^6$ consecutive $I$–$V$ sweep cycles.

the devices we have fabricated and studied.

In 2014 Nili et al. [19] reported Pt/Ti/a- STO (100 nm)/Pt memristors with 20-100 µm dimensions.. These device operate after a forming pulse (reported in fig. 2.15a). These forming pulses are the irreversible lowering of the device resistance by sweeping the voltage up to 8-10 V (for this particular device). After this forming pulse the devices exhibit stable, non-volatile, resistive switching behavior (fig. 2.15b,c) with OFF/ON resistance ratios of over $10^3$ (read voltage: $\pm$ 250 mV). These devices are also stable in time and operate for more than $10^6$ with no appreciable changes in the ON and OFF resistances.

XPS spectroscopy of 100 $\times$ 100 devices was used to probe the defect chemistry of the resistive switching mechanism. The result is in fig. 2.16: the virgin state shows an oxygen deficiency of $\approx$ 3% while the formed state has an oxygen deficiency of $\approx$ 5%, increasing while approaching the Ti electrode. Since this technique averages the measured concentration, we can conclude that there is an overall movement of oxygen vacancies in the device during the forming pulse. The distribution of oxygen vacancies around the Ti electrode denote a redox process in this metal/oxide interface. The bipolar switching is thus the rearrangement of the oxygen vacancies, due to the applied bias, moving towards the Pt electrode forming conductive pathways, since the oxygen vacancy alters the local stoichiometry of the STO creating a highly $n$-doped structure from one electrode to the other. Furthermore, scanning probe microscopy (SPM) and nano-contact measurements indicate the existence of structurally weak

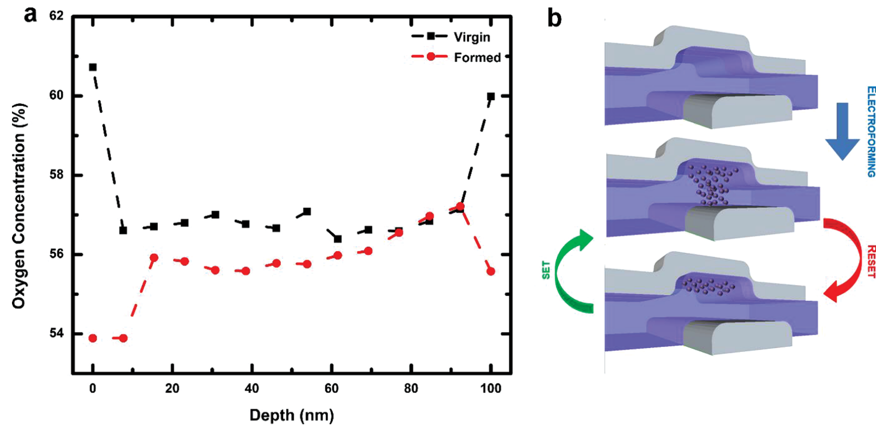


Figure 2.16: a) Relative oxygen concentration throughout the thickness of the oxide layer calculated based on XPS depth profile results on 100 μm × 100 μm a-STO cells, before and after forming pulse. b) Schematic of forming pulse and subsequent switching mechanisms in a- STO cells.

nano-grains, distributed uniformly in the device, that act as filaments that can harbor the oxygen vacancies and act as nano-switches, causing the resistive switching of the device. As oxygen vacancies drift from one electrode to the other during the forming pulse through a network of pre-existing defects, an extended network of filaments is created. The amorphousness of the material is the key to the forming of these filaments: the lack of crystalline order causes a non-preferential expansion of the defects structure around the pre-existing point defects creating the pathway that can harbor oxygen vacancies.

## 2.3 Conduction through insulators

Since in this thesis I will present results based on studies on insulating junction, I will briefly show the mechanisms of electron conduction in such insulating materials we used in this study.

### 2.3.1 Tunneling

When an electron tunnels from one metal to another metal through an insulator, if the two metal electrodes are of two different materials and thus with generally different work functions, the differential conductance $G(V) = \mathrm{d}I/\mathrm{d}V$ is, according to the commonly used Brinkman-Rowell-Dynes model [28],

$$G(V) = G(0)\left[1 - \frac{A\Delta\phi}{16\phi^{3/2}}eV + \frac{9}{128}\frac{A_0^2}{\phi}(eV)^2\right] \tag{2.1}$$

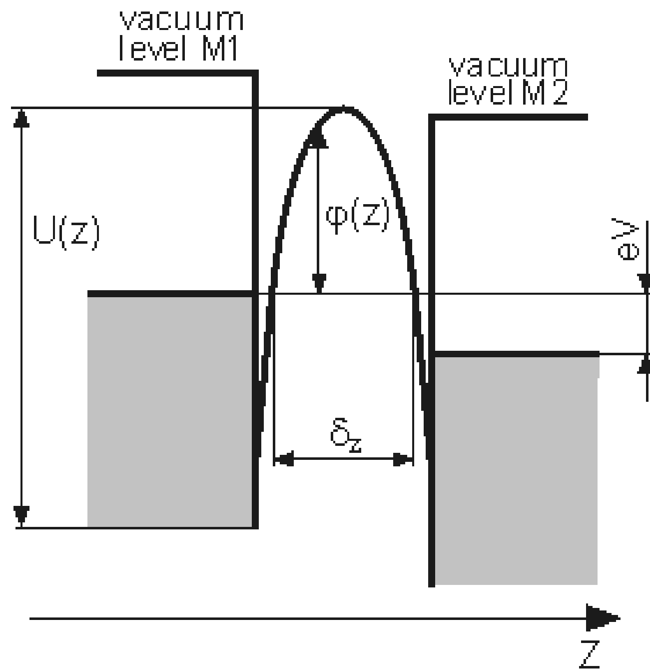


Figure 2.17: Metal/insulator/metal device with an arbitrary potential barrier.

where $\Delta\phi$ is the asymmetry of the barrier heights on the two sides of the insulator, $\phi$ is the average barrier height in the insulator, $A_0 = 4(2m)^{1/2}d/3\hbar$ and $G(0) = 3.16 \times 10^10\phi^{1/2}d\exp(-1.025d\phi^{1/2})$. If $\Delta\phi = 0$ the formula previously obtained is equivalent to the common Simmons formula for tunneling without considering barrier asymmetry. There is no complete theory explaining the temperature dependence of the resistance in a purely tunneling regime since temperature is commonly expected not to modify the system in any way. If the tunneling states have show a strong temperature dependence of their DOS this may influence the temperature dependence of the resistance of the tunneling device.

### 2.3.2 Nearest neighbor hopping

In nearest neighbor hopping conduction, electrons hop from one empty impurity site to the other with an activation energy $W = T_{NNH}/k_b$ and the resistance of the device is

$$R(T) = R_0 \exp\left(\frac{T_{NNH}}{T}\right) \tag{2.2}$$

while the hopping distance is

$$R_{NNH} = \left(\frac{4\pi N_d}{3}\right)^{1/3} \tag{2.3}$$

where $N_d$ is the concentration of carriers in the junction. If we define the parameter $\lambda = R_{NNH}/a$, where $a$ is the effective Bohr radius

$$.a = \frac{4\pi\epsilon_0\epsilon_r\hbar^2}{m_e e^2}, \tag{2.4}$$

it is expected to see NNH conduction if $\lambda \gg 1$. Instead, if

$$\lambda \to 1, \tag{2.5}$$

Mott argues that the system should show a metallic behavior [21].

### 2.3.3 Mott variable-range hopping

Nearest neighbor is not the only hopping mechanism for electrons in a disordered system. Provided that the DOS near the Fermi energy $E_f$ is slowly varying as a function of energy, Mott showed that the resistance of the insulator is

$$R(T) = R_0 \exp\left(\frac{T_M}{T}\right)^{1/4}. \tag{2.6}$$

The hopping distance is

$$R_M = \frac{3}{8}\xi\left(\frac{T_M}{T}\right)^{1/4}, \tag{2.7}$$

where $\xi$ is the localization length, and the energy difference between sites is

$$\Delta_M = \frac{1}{4}k_bT\left(\frac{T_M}{T}\right)^{1}/4. \tag{2.8}$$

There are two requirements that need to be satisfied for this kind of hopping to take place instead of nearest neighbor. The hopping length $R_M$ needs to be $\gg R_{NNH}$. The second revolves around coulomb interaction between hopping sites: this interaction freezes some electrons and reduces the DOS at the Fermi level in energy range of width $\Delta_C$. Mott variable-range hopping is observed when

$$\Delta_{NNH} > 2\Delta_C. \tag{2.9}$$

### 2.3.4 Efros-Schklovskii variable range hopping

What happens when the condition on the the energy difference of Mott variable-range hopping is no longer valid? This regime is called Efros-Schklovskii variable range hopping, where the resistance follows

$$R(T) = R_0 \exp\left(\frac{T_{ES}}{T}\right)^{1/2}. \tag{2.10}$$

Hopping length is

$$R_{ES} = \frac{3^{1/6}}{2^{5/6}2.8^{1/2}}\xi\left(\frac{T_{ES}}{T}\right)^{1/2} \tag{2.11}$$

and the energy difference between sites if

$$\Delta_{ES} = \frac{6^{1/2}}{2.8^{1/2}}k_b\left(\frac{T_{ES}}{T}\right)^{1/2}. \tag{2.12}$$

Also, in this regime it is possible to computed the localization length as

$$\xi = \frac{10.5}{k_b T_{ES}(\pi g_2)^{1/3}}, \tag{2.13}$$

where

$$g_2 = \frac{3^8\pi^2\epsilon_0^3\epsilon_r^3}{2^5 e^6}. \tag{2.14}$$

There are four condition to fulfill so that this kind of conduction is possible:

$$\Delta_{ES} \geq k_b T \tag{2.15}$$

$$d \gg R_{ES}, \tag{2.16}$$

where $d$ is the thickness of the insulator,

$$R_{ES} \geq \xi \tag{2.17}$$

$$\Delta_C > \Delta_{ES}. \tag{2.18}$$

### 2.3.5 Poole-Frenkel effect

While the previous hopping mechanism are applied to disordered system such as amorphous materials, when the insulator is a crystal and thus present a band structure, transport can occur when thermal excitation excite the electron to the conduction band the electron can move before relaxing to another localized state. The temperature dependence is the same as nearest neighbor hopping, but since this transport relies on band structure, the deformation of the electron band by the applied bias comes in to play, giving this transport mechanism

$$I \propto V \exp\left(\frac{-e(\phi - \sqrt{eV/d\pi\epsilon_0\epsilon_R})}{k_b T}\right), \tag{2.19}$$

where $\phi$ is the voltage barrier at zero bias.

### 2.3.6 Zabrodskii-Zinov'eva analysis

In 1984 Zabrodskii and Zinov'eva proposed an analysis to study how to distinguish between different hopping regimes. Suppose that the resistance of a sample follows the law

$$R(T) \propto T^{-m} \exp(T_0/T)^s \tag{2.20}$$

(for example, for nearest neighbor hopping $m = 0$ and $s = 1$ and for Richardson-Schottky emission, where the resistance of an insulator is dominated by the injection through the interface barrier, $m = 1$ and $s = 1$), if we define the function

$$W(T) = -\frac{\mathrm{d} \ln R(T)}{\mathrm{d} \ln T}, \tag{2.21}$$

then

$$\ln W(T) \approx \ln(sT_0^s) - s \ln T. \tag{2.22}$$

If we plot $\ln W(T)$ vs $\ln T$ the slope is $-s$. By using this data analysis one can easily extrapolate the value $s$.
This analysis cannot prove by itself that some kind of hopping takes place, for example by finding $s = 0.5$ one cannot immediately say that the sample follows Efros-Schklovski variable range hopping since one should also take into consideration the conditions required by theory. Still, it is a very useful method to intuitively exclude certain kinds of hopping and concentrate one's analysis on others.

Chapter 3

# Pinholes in vertical devices

Since interest in MTJs renewed in the '90s, it became important to find ways to test is electron conduction is actually through single-step tunneling, which in many cases is an unlikely conduction mechanisms though an insulator and may be shadows by other competing conduction mechanisms. In particular, in a vertical ferromagnet/insulator/ferromagnet (F/I/F) trilayer device there may be small, metallic conduction path from one ferromagnetic electrode to the other, paths known as pinholes. The pinhole originally were thought as short circuits formed by one electrode percolating through the insulator and touching the other electrode but these results also apply to memristors that rely on the creation an annihilation of metallic paths through an insulator [12] [19] [20]. Since magnetic nanocontacts were found to have magnetoresistances up to 300% many research groups have became to study effects on pinhole in vertical trilayer devices, and in particular whether there pinhole contribute to or degrade the magnetic properties of these devices.
Between the '60s and '70s, Rowell developed various criteria to determine the absence of pinholes in multilayer structures containing superconducting electrodes. In a F/I/F trilayer, three of these criteria are commonly used: (i) an exponential insulator thickness ($t$) dependence of the resistance,

$$R(t) \propto \exp(t/t_0),$$

with $t = \hbar/2\sqrt{2m\Phi}$, (ii) a parabolic voltage (V) dependence of the conductance G(V) that can be fitted to theoretical models of symmetrical (Simmons model [27]) or asymmetrical barriers (Brinkman-Dynes-Rowell model [28]), and (iii) a weak insulating-like temperature dependence R(T). Unfortunately, it was shown that these criteria can be bypassed by pinholes.

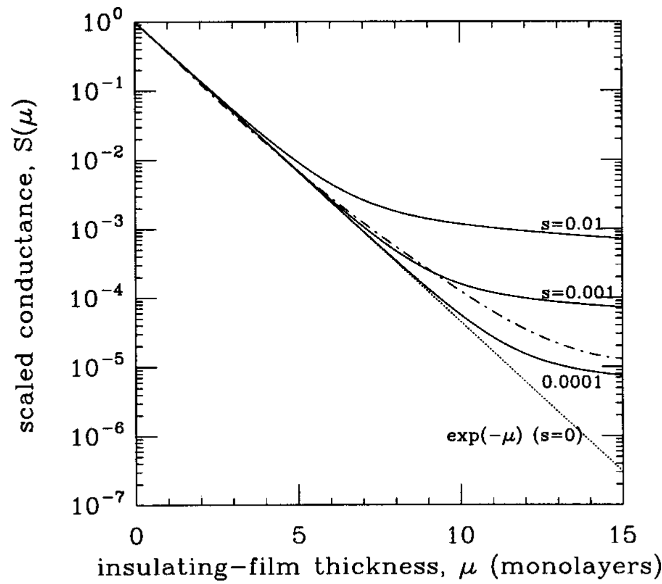


Figure 3.1: Conductance as a function of film thickness for various values of $s = R_0/R$. [23]

### 3.0.1 Thickness dependence criterion

The first criterion, exponential thickness dependence of the resistance was shown by Rabson [23] to be reproducible by pinholes by numerical calculations. Since a tunnel junction typically has a resistance-area product of 1 k$\Omega\mu$m$^2$ and a metallic junction has a resistance-area product of 1 m$\Omega\mu$m$^2$, even a small pinhole region of 1 part in $10^6$ ensures that half of the current is through the pinhole.
Consider a first metallic electrode on top of which a perfect insulator is randomly deposited, approximating every layer of the insulator as an $L \times L$ lattice. If the deposition is thermal, the distribution of the height of the barrier over one single cell is poissonian (assuming one column is independent from the others). If we then deposit another metallic electrode over the insulator, we have short circuits only in the cell where no columns were formed. In fig. 3.1 there is a graph of the computed conductance for various values of $s = R_0/R$ where $R_0$ is the resistance of the nanocontact between the electrodes and $R$ the resistance of one block of insulator. The crossover thickness (in monolayers) above which the conductance ceases to be exponential is

$$\mu_0 \approx \ln(2/s).$$

The contact resistance through a pinhole of diameter 1 $\mathring{A}$, and assuming a typical metallic Fermi temperature and electronic density, we have contact resistance $R_0 =$

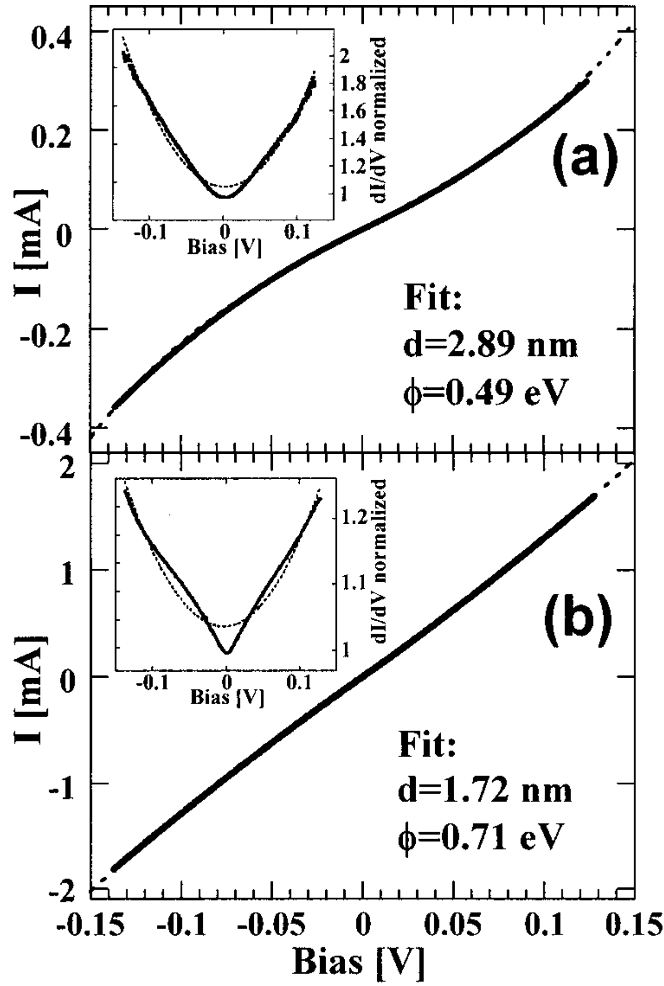


Figure 3.2: (a) I –V curve for sample A at $T = 90$ K together with a fit to Simmons' model (dashed line). Inset: original conductance data fitted with the BDR model (dashed line). (b) Same for sample B at T=77 K.

$10^4$ V. The classical resistance of an insulating block is less well defined, but a minimum resistivity $10^6$ V cm suggests $R \geq 10^{14}$ V, so that $s \geq 10^{-10}$. For this value, the critical thickness is $\mu_0 = 24$ monolayers.

### 3.0.2 Conductance criterion

Even the second Rowell criteria can be useless to probe for pinholes. Akerman et al. [24] fabricated two different Nb/Al/$AlO_x$/Fe, one being a standard MTJ and the other with pinholes. At 90K, both devices had differential conductances that gave reasonable fits with Simmons' model. According to this model, the conductance of an MTJ where an electron tunnels through an arbitrary energy barrier $\phi$, the conductance is [27]

$$G(V) = G_0 + G_0 \left( \frac{9}{128} \frac{A^2}{\phi} \right) (eV)^2 \tag{3.1}$$

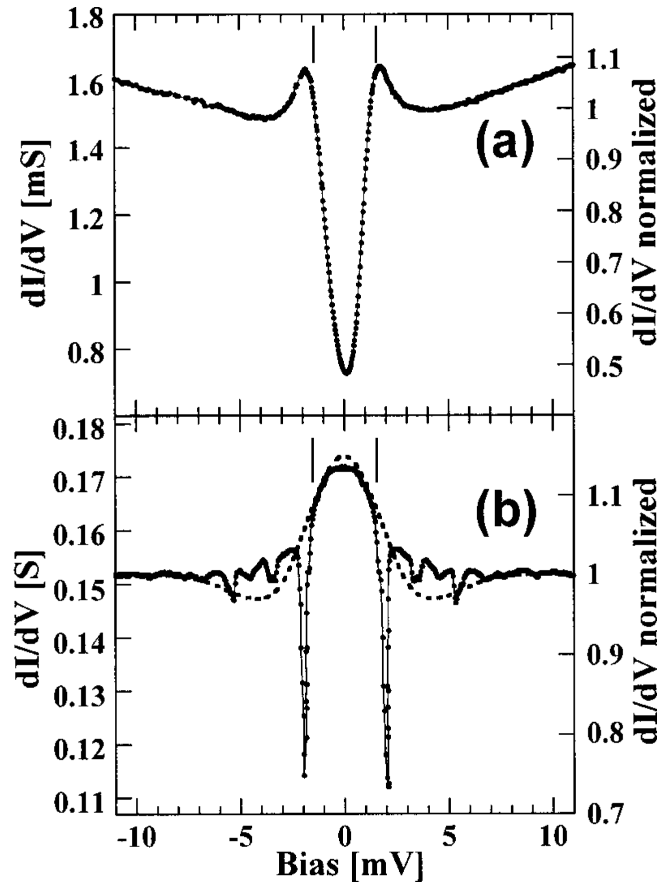


Figure 3.3: Differential conductance of the two samples at $T = 4.2$ K, where the Nb layer is superconducting. The lines indicate the gap voltage for bulk Nb, $\pm$ 1.5 mV. The dashed line in (b) is data from for an Fe–Ta point contact with the bias scale multiplied by the gap ratio of Nb to Ta. [24]

where $A = 4(2m)^{1/2}d/3\hbar$, $d$ the thickness in Å. Fig. 3.2 shows the $I - V$ curves and conductances of both devices, giving very reasonable parameter from fits using Simmons's model. Fits using Brinkman-Dynes-Rowell's model also give reasonable parameters. To prove that one device feature tunneling while the other had pinholes, the devices were cooled below the superconducting critical temperature of the Nb electrode. In fig. 3.3 the first device shows the typical tunneling conductance through a superconducting electrode: a reduced conductance near $V = 0$ and two symmetric maxima after $\pm\Delta$. The second device shows an increase of conductance near $V = 0$, consistent with Andreev reflection at a superconductor/metal interface, and a negative conductance spike after $\pm\Delta$, also typical of superconductor/metal nanocontacts. Comparing the conductance to that of a Fe-Ta point contact further proves the presence of pinhole. It is hence safe to conclude that a fit above Tc cannot be used as a criterion to ascertain whether or not a tunneling barrier is free of pinholes.

Zhang and Rabson used a simple model to explain this phenomena. Tunneling

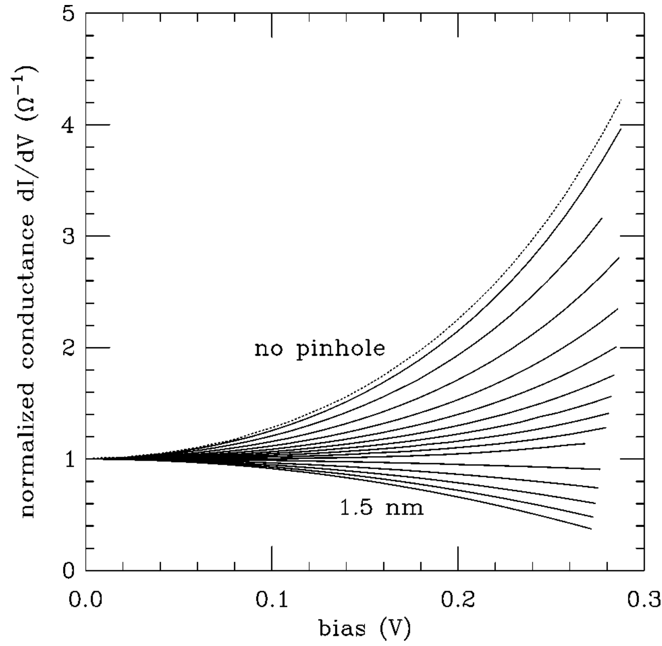


Figure 3.4: Computed normalized differential conductance for devices with pinholes of different thicknesses. [25]

features a conductance that increases with bias, as carriers see an effectively narrower trapezoidal barrier. This conductance can be modeled with the previously mentioned Brinkman-Rowell-Dynes model. On the other hand, a pinhole will dissipate more heat with greater biases and conduct less, giving a conductance with downward curvature; the total curvature of the conductance of a device will feature an interplay between these two channels. To quantify this behavior, a Al/$AlO_x$ (2 nm)/Fe with an Al pinhole in the center is modeled through numerical computation. The pinhole can have widths up to 1.5 nm. The result of the computation is in fig. 3.4. The result is that the curvature of the conductance is upward up to 1 nm thickness of the pinhole. These conductances fit with Simmons model giving effective barrier heights from 0.5 eV (the actual barrier height) to 1.6 eV (at 1 nm) and effective thicknesses of the barrier from 2 nm to 1 nm (at 1 nm pinhole width). These two experiments show how difficult it is to properly fit $I - V$ and conductances when there are pinholes.

### 3.0.3 Temperature dependence of the resistance: the parallel circuit model

Only the third criterion, the temperature dependence of the device, still stands. To study the effect of pinholes on the resistance-temperature curve of the device, Ventura et al. [29] developed a simple phenomenological model to quantify the effects of pinholes of the R(T). In this model, a metallic channel and a tunneling channel are

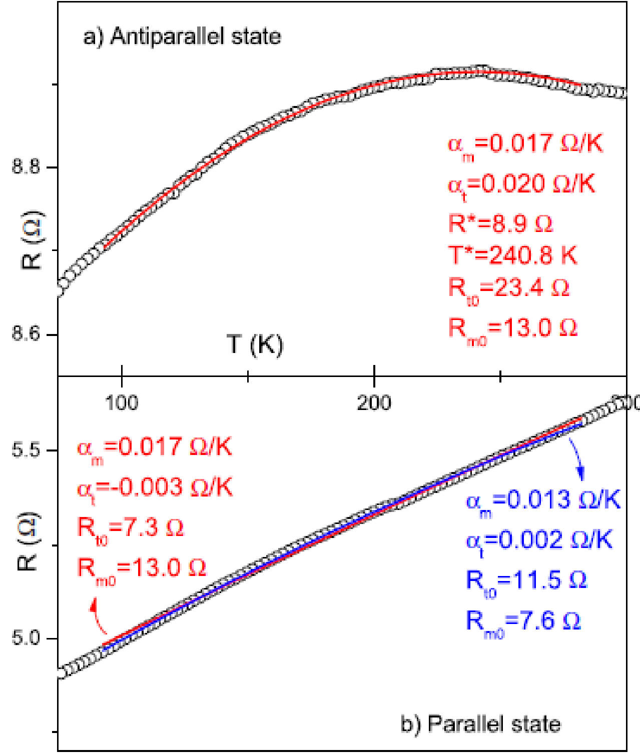


Figure 3.5: Temperature dependence of the resistance of an MgO MTJ with the electrodes in the antiparallel and parallel state. [29]

placed in a parallel circuit. This model is extremely simple but works simply with the assumption that geometrical effects are irrelevant and that the two channels are independent (i.e. we ignore tunneling from an electrode to the pinhole and, vice versa, tunneling from somewhere in the pinhole to an electrode). Thus the resistance of the device is

$$\frac{1}{R_d} = \frac{1}{R_m} + \frac{1}{R_t} \tag{3.2}$$

where $R_d$ is the resistance of the devices, $R_m$ the resistance of the metallic pinhole and $R_t$ the resistance of the tunneling. Simply using linearly increasing and decreasing resistance for the pinhole and the tunneling, respectively, R(T) curves of MgO MTJ were fitted both in parallel and antiparallel state of the magnetization of the electrodes. These devices featured a room temperature TMR of at least 60%. The antiparallel state (fig. 3.5) clearly shows a crossover temperature (where dR/dT goes from positive to negative) reproducible by a parallel of two linearly increasing and decreasing resistance channels

$$R_m = R_{m0} + \alpha_m * T \qquad R_t = R_{t0} + \alpha_t * T. \tag{3.3}$$

Then fitting the parallel state while keeping the pinhole channel parameter set (i.e. assuming that the magnetoresistance is entirely attributable to the tunneling channel gives unreasonable parameters for the tunneling channel: a negative $\alpha_t$ and a MR of 220% for the tunneling channel, implying a higher resistance in the parallel state which is the opposite of what has always been found in pinhole-free Mg0 junctions. A second fit with all four parameters was used, obtaining similar parameters compared to the antiparallel state for the tunneling channel but very different, indicating that the MR is attributable also to the pinholes.

### 3.0.4 Ballistic magnetoresistance

The problem of explaining magnetoresistance in pinhole conduction still remains. Garcia has shown that ballistic electron conduction through sufficiently small pinholes yields the same spin polarizations tunneling through an oxide layer, so that magnetoresistance cannot distinguish the two processes [30]. The theory for ballistic contact from one ferromagnetic electrode to another states [31]

$$BMR = \frac{R_{ap} - R_p}{R_p} = \frac{2P^2}{1 - P^2} \times F(\lambda, k_F) \tag{3.4}$$

with

$$F(\lambda, k_F) = \frac{1}{2} \left( \frac{1}{\cosh^2 \pi k_F \lambda} + \frac{1}{\cosh^2 \pi P k_F \lambda} \right) \tag{3.5}$$

which accounts for spin depolarization due to domain wall scattering. $\lambda$ is the width of the domain wall and $k_F$ the Fermi wave vector. If the domain wall width at the nanocontact $\lambda$ is very small, $F \approx 1$ and the $BMR$ formula is exactly the same as the Jullière $TMR$ formula. The reason the formulas are same is because the processes arise from the same physical principles, which is the matching of the wave functions at both sides of the pinhole [30]. The only difference between the two processes is that in ballistic contacts the transmissivity is almost 1 while in tunneling it decays exponentially with the junction length $l$.

Chapter 4

# Experimental setup

The devices studied in this thesis are made of a bottom electrode of LSMO, a layer of STO and a top electrode of Cobalt, as in fig. 4.1. In this chapter I will describe both the fabrication process and the equipment and techniques used to study the devices.

## 4.1 Device fabrication

The spin-valve devices are fabricated by shadow masking following the steps illustrated in fig. 4.2. As a substrate a $10 \times 5$ mm$^2$ NGO (110) single crystal from CRYSTAL GmbH is used. The crystal is cleaned by sonication in isopropanol. This is a good substrate for LSMO growth because of the very small difference between lattice parameters (NGO is an orthorombic material with $a = 0.544$ nm and $b = 0.550$ nm, since the subrate is (110), over one NGO cell are deposited two LSMO cells, which has a cell parameter of 0.387 nm). With LSMO on NGO the dead layer (a thin layer of LSMO which has no magnetic properties because of strain) is roughly 3 nm.

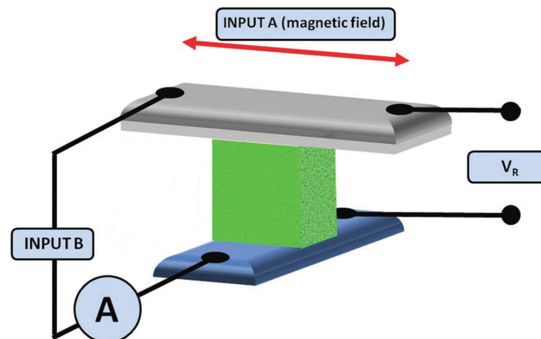


Figure 4.1: Schematic representation of a device. A layer of STO is sandwiched between the two perpendicular electrodes (LSMO and Co) [11].

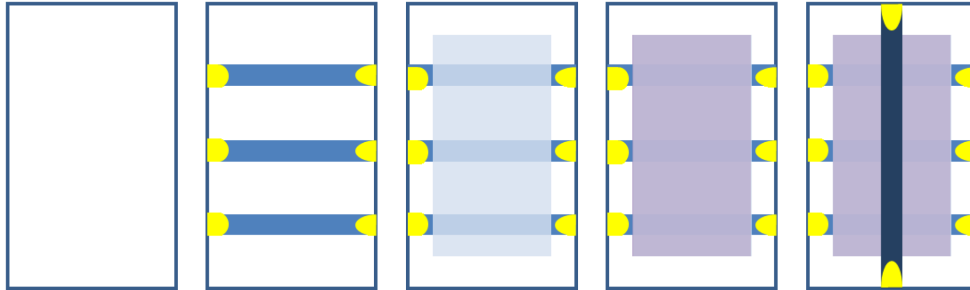

Figure 4.2: Fabrication steps for a spin-valve device. (a) STO substrate. (b) LSMO bottom electrodes with gold contacts on top. (c) Spacer layer. (d) AlOx tunnel barrier (only for organic Alq3 spacers). (e) Co top electrode with gold contacts.

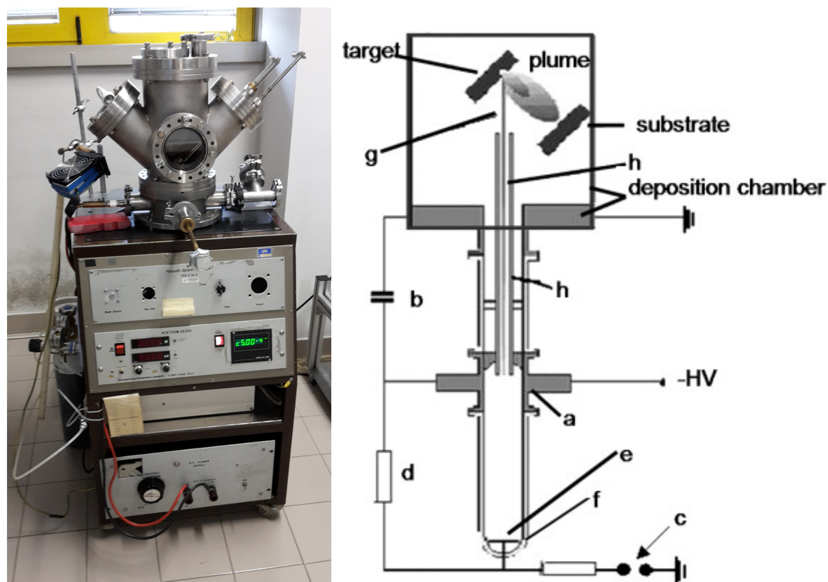


Figure 4.3: Photo and schematic of a Channel Spark Ablation machine. [32]

### 4.1.1 LSMO electrodes and STO barrier

To deposit the oxides we used a Channel Spark Ablation (CSA) machine, shown in fig. 4.3. The same figure shows the working principle of the CSA: a negative high voltage (5-30 kV) power supply is directly connected to a hollow cathode (a) and a capacitor (b). The latter is grounded through an air gap (c) having a floating electrode which is decoupled from the capacitor by charging resistor (d). Between the charging resistor and the floating electrode of the air gap a triggering anode plate (e) is located and inserted in the bulb (f). At a sufficient high voltage a spark breaks down the air gap (c), a rapid variation of the electric field between the hollow cathode and the anode plate ionizes the gas molecules in the bulb triggering plasma in the cathode cavity (a), where the amplification of the discharge happens. Because of the high resistance of the charging resistor, the capacitor discharge happens through the low impedance electron beam in the Pyrex channel(h). The electron beam current would be continuous if the power supply could provide a sufficient current, but since its limited in current, the electron beam cannot be sustained and the discharge extinguishes up to the new spark in the air gap. As a consequence the beam assumes a pulsed character. The current supplied to charge the capacitors defines the charging time and, hence, the operating frequency. The high voltage and the capacitance determine the accumulated charge and the total energy. The energy distribution of the electrons in the beam and the length of the pulse is determined by the accelerating voltage and gas pressure [32].
The electron beam then hits and oxide stochiometric target that heats up and creates a plasma plume, directed at the desired substrate.
After the deposition of bottom LSMO electrodes at 850 $^{o}$C in an atmosphere of $10^{-2}$ mbar of $O_2$, the sample is then annealed at 250 $^{o}$C for 30 min in order to restore the LSMO surface the sample and STO is deposited (at 750 $^{o}$C for epitaxial STO and 350 $^{o}$C for amorphous STO). The epitaxial growth of STO is guaranteed by the similar lattice parameter of the the two perovskite oxides: 0.386 nm for LSMO an 0.390 nm for STO. The sample is then exposed to air and introducedin a load lock chamber at a base pressure of $10^{-6}$ mbar, where gold contacts are evaporated on LSMO stripes as illustrated in fig. 4.2. The sample is then transferred into the main chamber.

### 4.1.2 Cobalt electrode

The sample is transferred in the metal-deposition chamber at a base pressure of $10^{-8}$ mbar. A mini e-flux e-beam evaporator from tectra GmbH is used to evaporate the cobalt top electrode. A coiled tungsten filament (ground potential) is placed in close vicinity of a cobalt rod with a diameter of 2 mm (kept at the positive potential of 2 kV). The thermionically emitted electrons are accelerated towards the rod producing a current of 8-10 mA with extremely high heating-power densities. High-purity cobalt

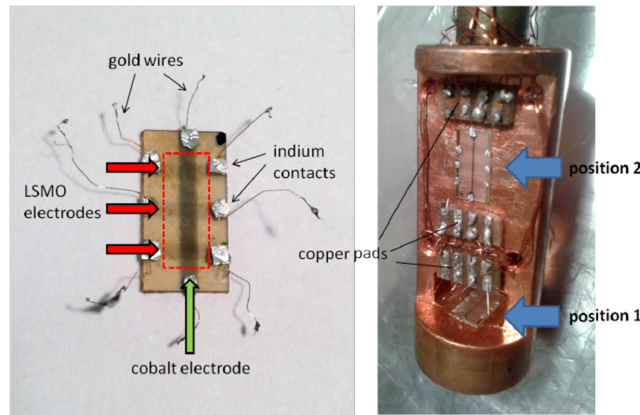


Figure 4.4: (a) Top view of a substrate with three devices, whose active region corresponds to the cross section between LSMO and cobalt electrodes. Organic layer is deposited inside the region indicated by the red dashed line. (b) Samples located on the cryostat sample holder. The copper pads connect the devices to the external plug. Position 1 and position 2 allow to rotate the sample respectively in plane and out of plane.

(99.99%) is then evaporated on the sample as top electrode in the cross-bar geometry described in fig. 4.2. A Sycon Thickness Monitor STM-1 is used to control the deposition rate (0.4-0.5 Å/s). Finally the sample is moved again in the load lock chamber, where gold contacts are deposited on cobalt.

## 4.2 Electrical characterization

Fig. 4.4a shows three spin-valve devices on a STO substrate. LSMO and cobalt electrodes are connected to gold wires with a diameter of 50 nm by means of indium. The samples are located on the cryostat sample holder and the wires are soldered to the copper pads (fig 4.4b), which connect the DUT (device under test) to the external plug. Electrical characterizations have been carried out by using a Keithley 236 Source Measure Unit (SMU). Fig. 4.5 shows the SMU electrical scheme in the Source V-Measure I configuration, both for remote sense (4-points) and local sense (2-points) mode. An ammeter is connected between the voltage source (Vsource) and Output HI. Sense circuitry is used to constantly monitor the output voltage and make adjustments to Vsource as needed. Vmeter measures the voltage at the output (local sense) or at the DUT (remote sense) and compares it to the programmed voltage level. If the sensed level and the programmed value are not the same, Vsource is adjusted accordingly ensuring that the programmed voltage appears at the DUT. Triaxial cables (triax) are used to accurately measure low currents. Guard is kept at the same potential as the Output HI by the buffer circuit to eliminate the effects of the leakage current (and capacitance) that exists between the Output HI and the Output

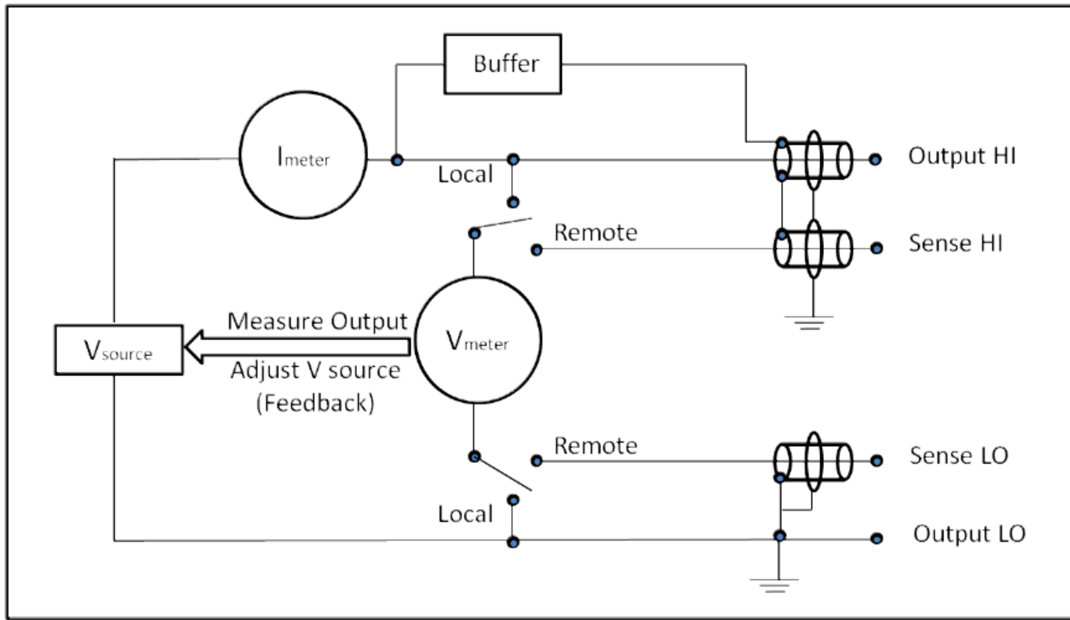


Figure 4.5: Electrical scheme of Keithley 236 SMU in the SourceV-MeasureI configuration. The instrument has an integrated feedback system: the measured voltage Vmeter is compared with the programmed voltage level and, if they are not the same, Vsource is adjusted accordingly. In local sense mode, Vmeter measures the voltage at the output, while in the remote sense mode it measures the effective voltage across the DUT.

LOw. A keithley 708A switching system has been used to automatically redirect the signals from the SMU to the desired electrodes as schematically represented in fig. 4.6a. The SMU and the switching system are connected in series to a PC through a GPIB to USB converter and I-V characteristics are acquired by means of a software developed in LabView programming environment (fig. 4.7).
The fabricated device are measured with in four contact mode shown in fig. 4.1: this way we can ignore complications due to contacts and measure directly the resistance of the junction between the two electrodes.

## 4.3 Magnetic characterization

The sample holder is introduced into the inner chamber of a gas-exchange cryostat from Oxford Instruments, filled with nitrogen gas up to the pressure of 102 mbar. The outer chamber is kept at $100^{-}5$ mbar, in order to thermally insulate the system. The intermediate chamber is part of the nitrogen circuit: liquid nitrogen is pumped into the chamber from the dewar and the exhausted gas is pumped out, as described in fig. 4.8. The samples can be cooled down to 77 K and heated up to 400 K at the desired rate (K/min) by means an Oxford ITC 503S temperature controller. The coils

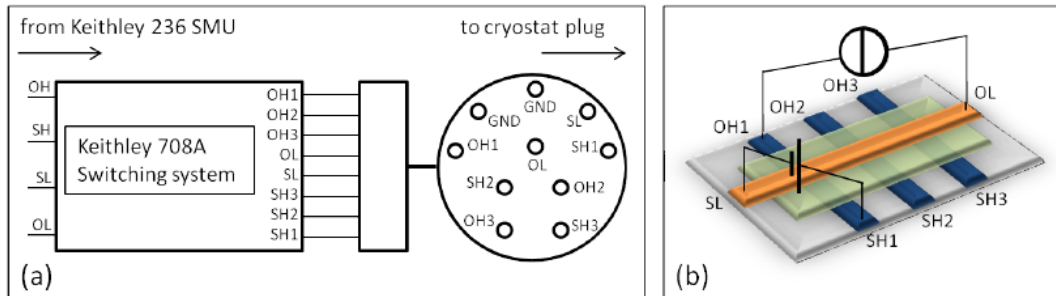


Figure 4.6: (a) Schematic representation of the circuitry connecting the SMU to the cryostat plug. The source signals (OH, OL) and the sense signals (SH, SL) from the SMU are sent to a Keithley 708A switching system which redirects them to the desired outputs (OH1, OH2, OH3, OL, SL, SH1, SH2, SH3). The core pins of the triax from the switching system are collected into the cryostat plug. (b) Device contacts corresponding to the pins of the cryostat plug. As an example device 1 in remote sense configuration is illustrated.

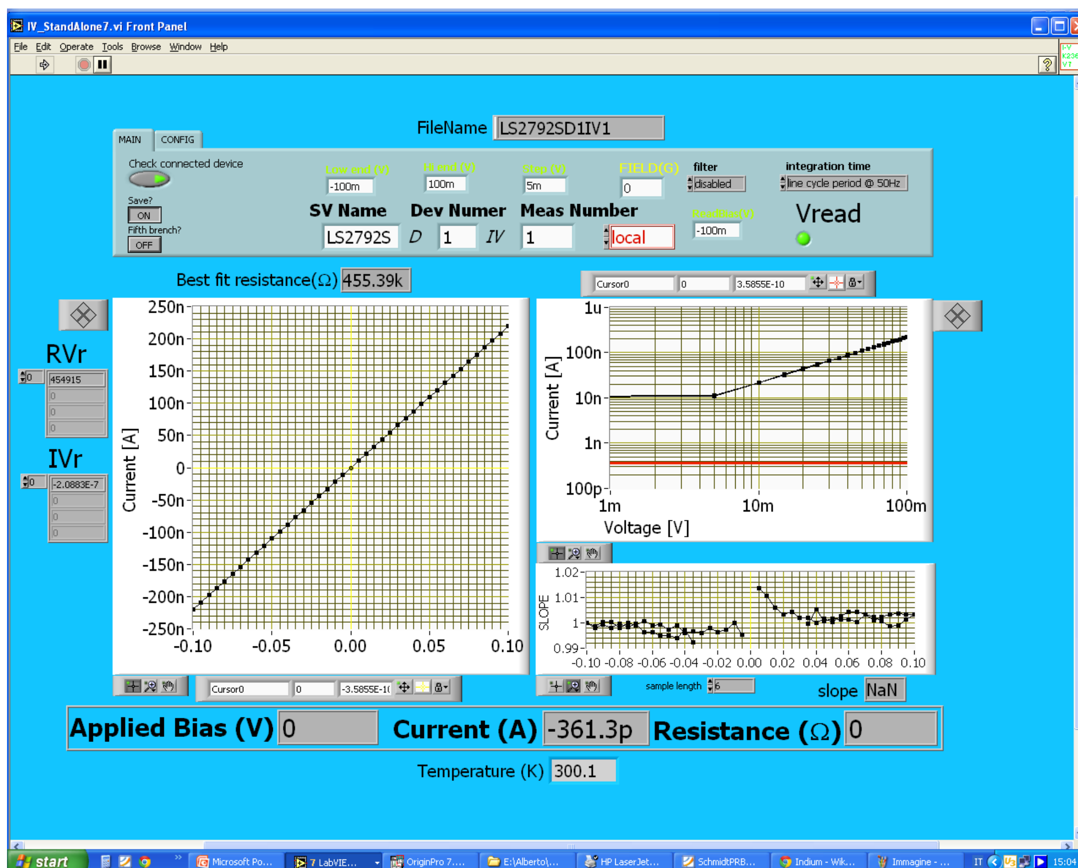


Figure 4.7: User interface of the LabView VI used to acquire I-V characteristics.

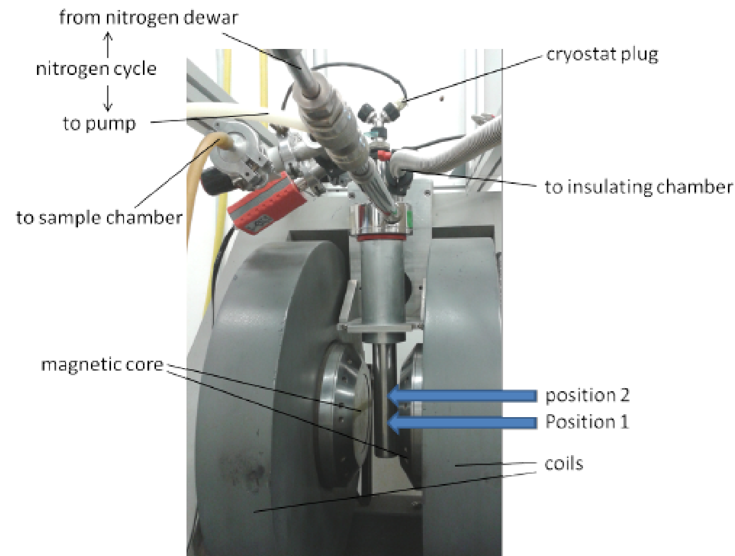


Figure 4.8: Experimental setup for magnetoresistive characterizations. The blue arrows indicate the position of the samples between the magnetic poles.

of the EPR electromagnet are connected to an Elind KL power supply through an high power switcher which allows to change the current direction. The right current-to-field conversion factor was obtained by calibrating the magnet with a gaussmeter. The high field homogeneity over a large volume guarantees that the same magnetic field is applied both to position 1 and to position 2. R-H characteristics have been taken by applying a fixed bias potential to the DUT and acquiring its resistance values as a function of magnetic field, typically ranging from -3 kOe to 3kOe (fig. 4.10). MR as a function of temperature are also measured. The sample is kept at a fixed bias potential and the difference between the resistance at zero and at applied field is taken, while the temperature is slowly increased the ITC temperature controller. Moreover, as mentioned before, the sample holder allows to rotate the sample in plane and out of plane (fig. 4.9) making possible to study the MR as a function of angle.

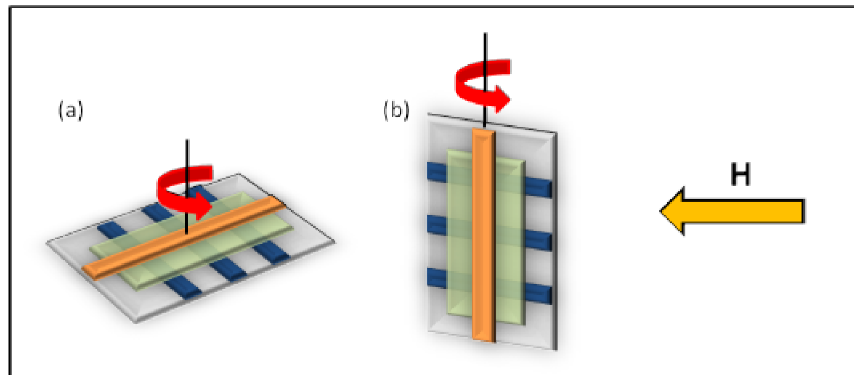


Figure 4.9: (a) Sample in position 1 can be rotated in plane. (b) Sample in position 2 can be rotated with a field component out of plane.

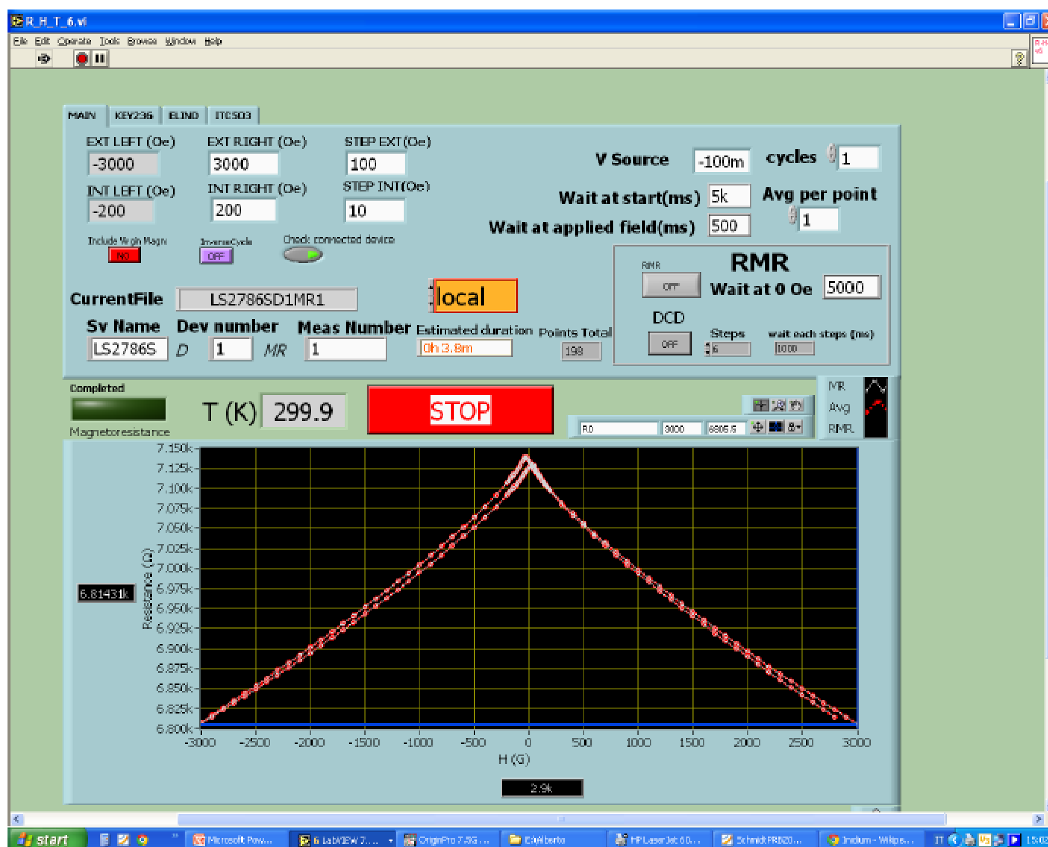


Figure 4.10: User interface of the LabVIEW VI used to acquire R-H characteristics.

# Chapter 5

# Structural characterization

The uniformity of the thicknesses of the materials of our devices is crucial to guarantee their proper functioning. Atomic force microscopy (AFM) measurements were taken after the growth of the LSMO electrodes on NGO substrates, described in the previous chapter. An image of 10 nm thick LSMO electrodes is in fig. 5.1. The root mean square roughness of the surface is 0.15 nm (1.5%). Since the percentage of root mean square roughness is known to lower with lower thicknesses, we can expect that the 5 nm LSMO electrodes (used in the devices studied in this thesis) has a root mean square roughness less than 0.075 nm (1.5%). This number has to be compared to the cubic cell parameter of the STO (0.390 nm); this means that the grown LSMO electrodes are essentially smooth to the scale of a cubic cell.

To check the crystalline quality of our devices, transmission electron microscopy (TEM) images were taken by K. O'Shea at the University of Glasgow. These images are in fig. 5.2: the Co electrode is policrystalline due to is granular appearance, the epitaxial growth of LSMO con NGO is good (due to the compatible cell dimensions);

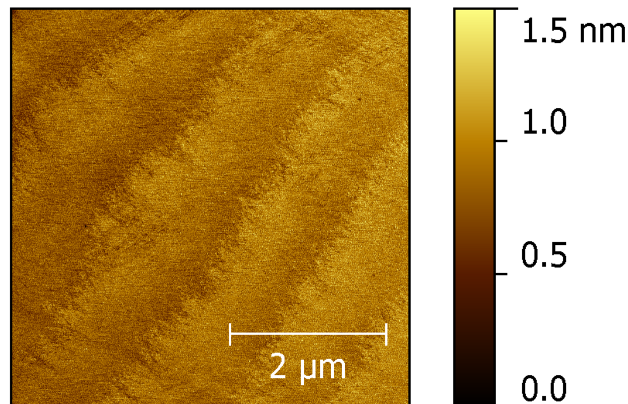


Figure 5.1: AFM image of a 10 nm thick LSMO electrode on an NGO substrate.

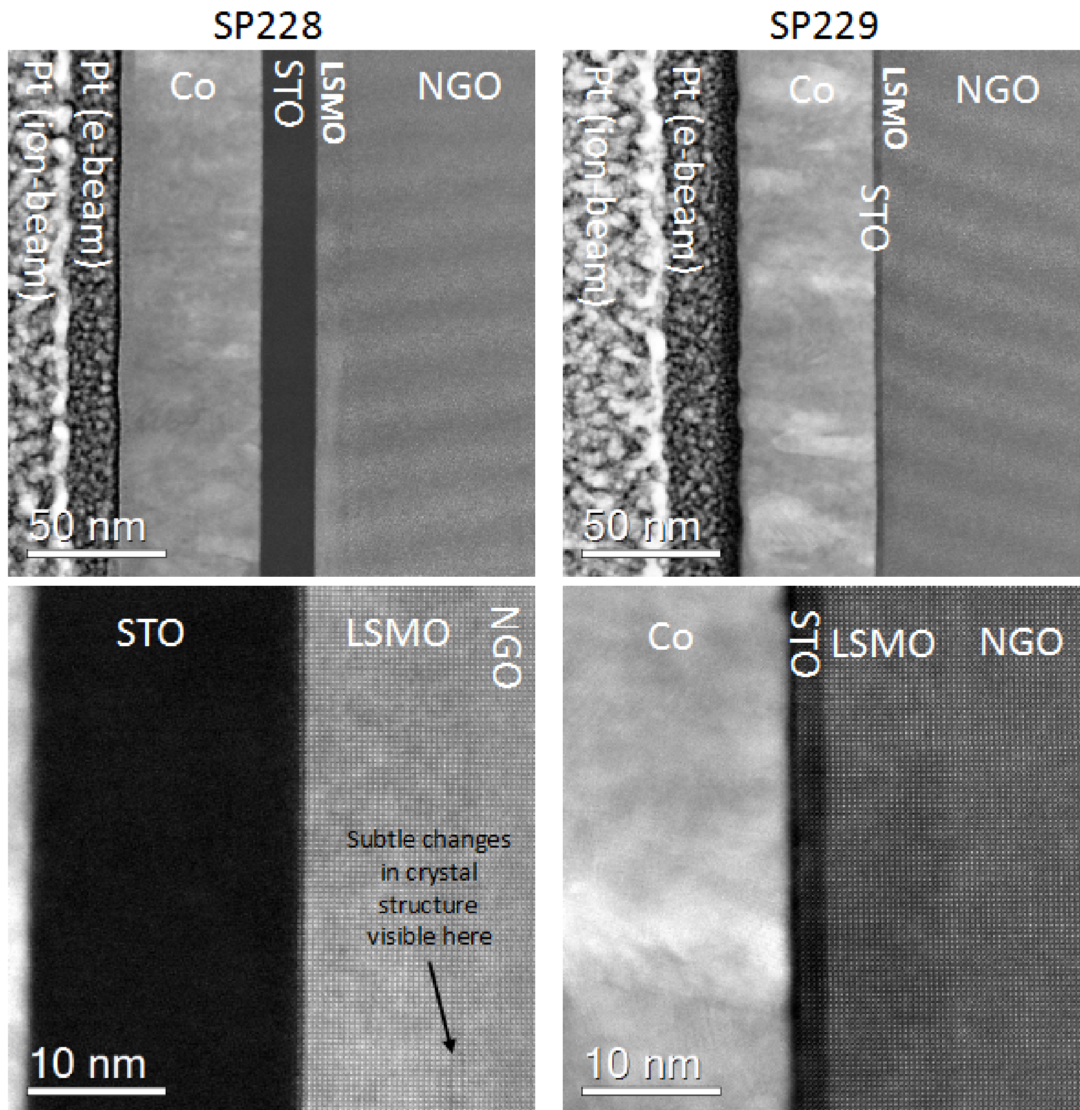


Figure 5.2: TEM images of a 25 nm thick amorphous STO device (SP228) and a 2.5 nm thick epitaxial STO device (SP229).

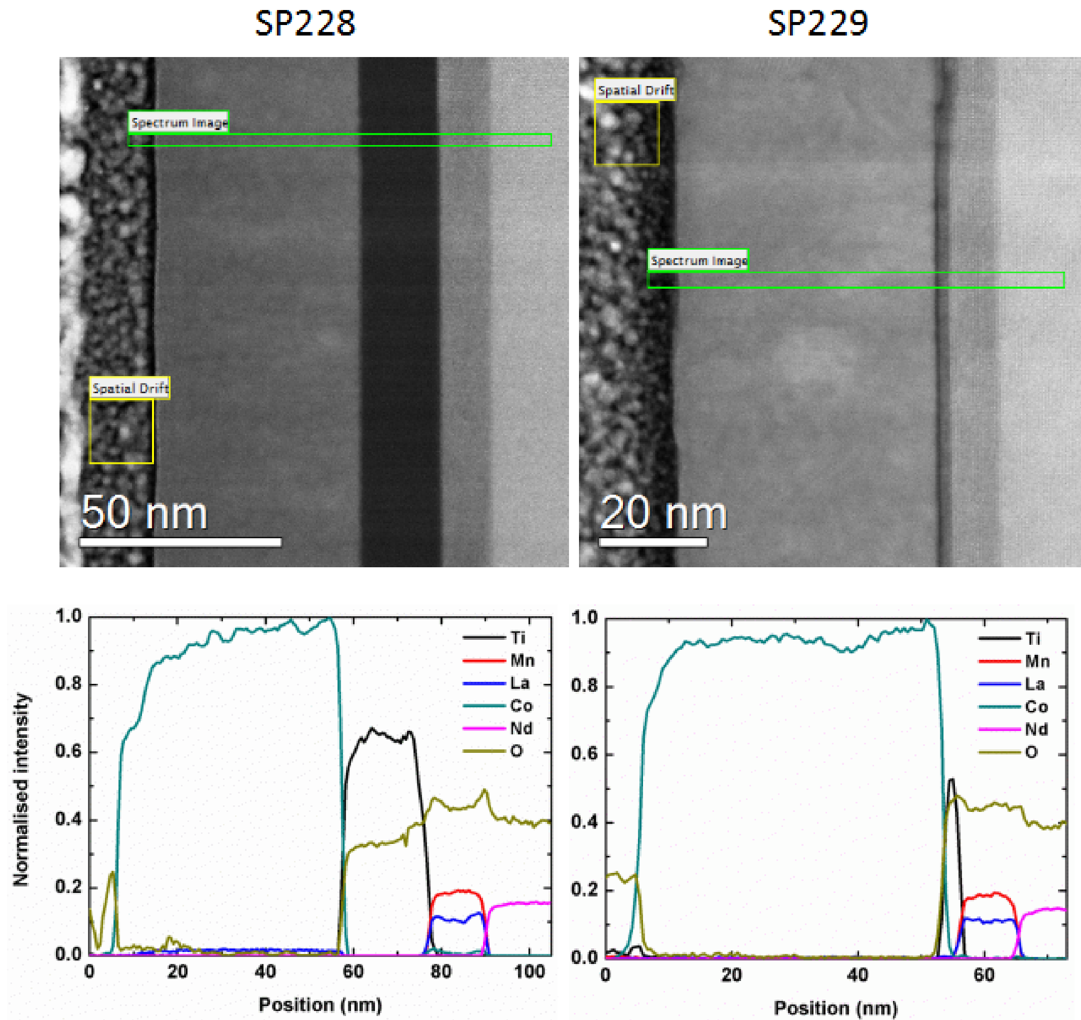


Figure 5.3: TEM spectra showing the chemical composition of a 25 nm thick amorphous STO device (SP228) and a 2.5 nm thick epitaxial STO device (SP229).

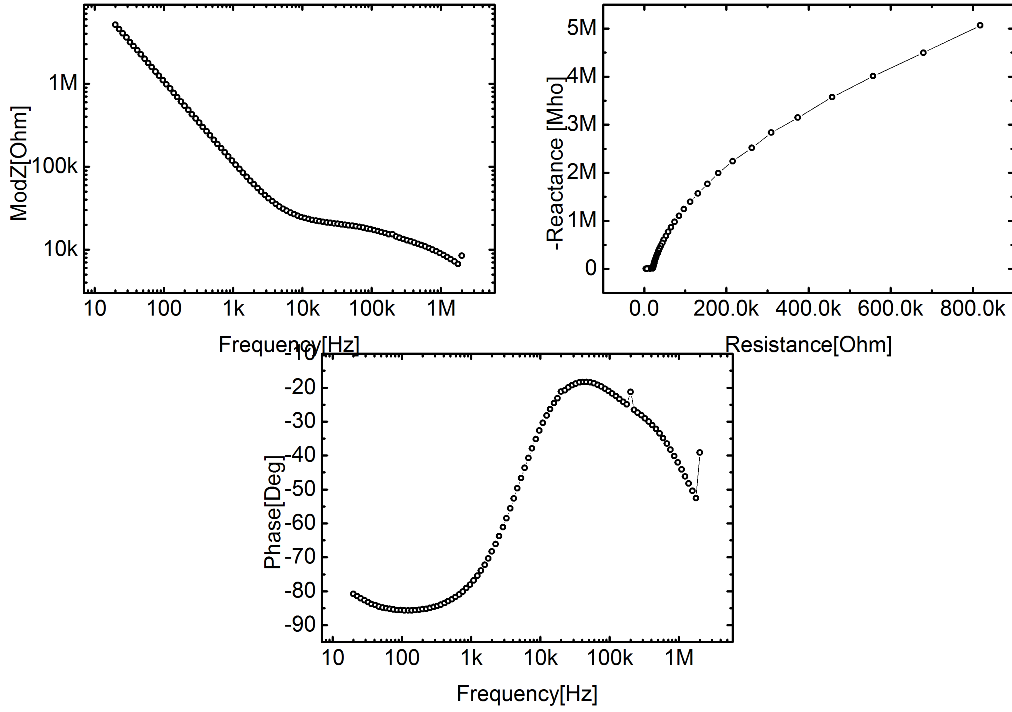


Figure 5.4: Impedance spectroscopy of a 5 nm thick a-STO device.

the STO grown at 350 $^o$C is completely amorphous while the STO grown at 750 $^o$C is completely crystalline. Taking the spectrum of the TEM images to investigate the chemical composition of the device (fig. 5.3) shows that, surprisingly, the oxygen signal is half of the titanium signal, indicating a high concentration of oxygen vacancies. Also, the fact that the STO imagine is very dark indicates a possible high concentration of strontium (the heavier element).

To further test the quality of our amorphous STO, we used impedance spectroscopy at 100 K to determine its dielectric constant. In fig. 5.4 is the results for a 5 nm thick a-STO device. Apart from deviations starting at 10 kHz, the device acts like a RC parallel circuit. Fitting the complex impedance of the device with the impedance of a RC parallel circuit

$$Z(\omega) = \frac{R}{j\omega RC + 1} \tag{5.1}$$

gives $C = 9.6$ nF. For a parallel plate capacitor

$$C = \frac{A\epsilon_0\epsilon_r}{d} \tag{5.2}$$

where $A$ is the area of the capacitor and d is the thickness. With our devices $A = 0.2$ μm$^2$ and $d = 5$, so

$$\epsilon_r = \frac{Cd}{\epsilon_0 A} = 28.$$

# Chapter 6

# Transport and forming pulse in amorphous and epitaxial STO

In this chapter I will show data relating to the transport of charge in $La_{0.7}Sr_{0.3}MnO_3$/ $SrTiO_3$/Co devices, both with epitaxial $SrTiO_3$ (e-STO) and amorphous $SrTiO_3$ (a-STO).

## 6.1 Amorphous STO devices

We fabricated LSMO/a-STO/Co devices with a-STO thickness of 5 nm and 25 nm. The LSMO thickness was of 5 nm, because of the smoothness of these thin films (reported in chapter 5) and, since memristive effects with oxide junctions rely on redox processes, the resistive and magnetoresistive behavior of the electrode could be used to probe these effects. I will focus the analysis on the data of the 5 nm thick devices but the same results are applicable to the other devices.

### 6.1.1 Hopping in a-STO junctions

The samples were fabricated with the techniques outlined in chapter 4 and set in the sample holder inside the cryostat described in the same chapter. The samples were then brought to 100K at a rate of 0.3 K/min, taking one resistance measurement every minute.
In this chapter I will consider two sample devices even though the same results were obtained on the others. At 100 K, device A showed forming pulse, lowering its resistance from 53 MΩ to 1 MΩ (at -0.1 V), by sweeping the applied voltage from 0 V to -2 V, as shown in fig. 6.1. The I-V curve shows negative differential resistance (NDR) and the two steps in this region suggests forming of two filamentary pathways, as proposed by Nili et al [19] [20]. The R(T) measurements both before and after this forming pulse are shown in fig. 6.2.

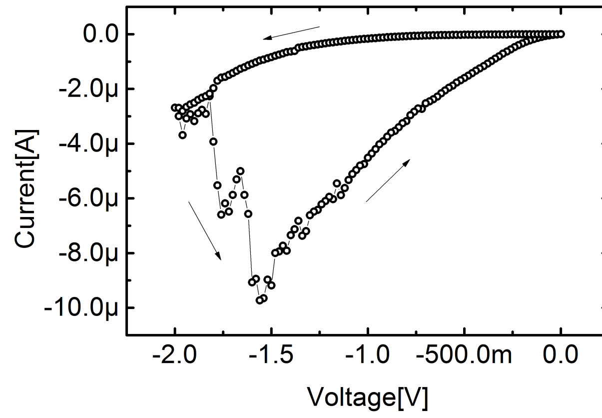


Figure 6.1: I-V measurement showing forming pulse. The arrows in indicate the direction of the sweep.

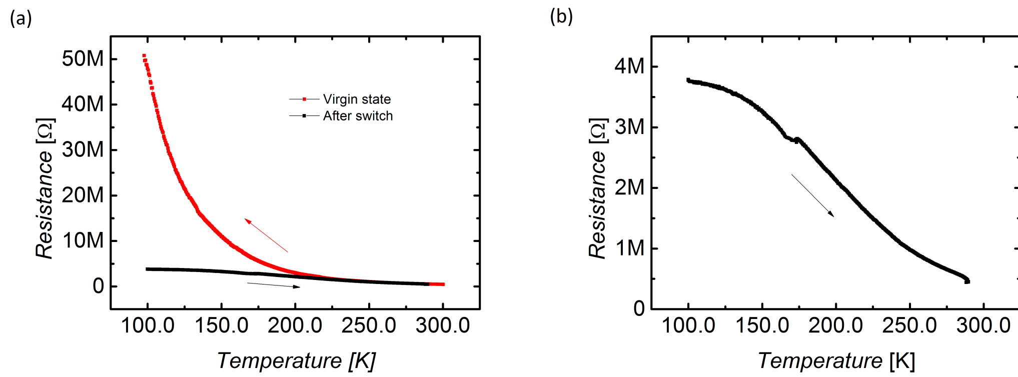


Figure 6.2: Measured R(T) curves (at -0.1V) of an a-STO device before and after forming pulse. The arrows in indicate the direction of the sweep.

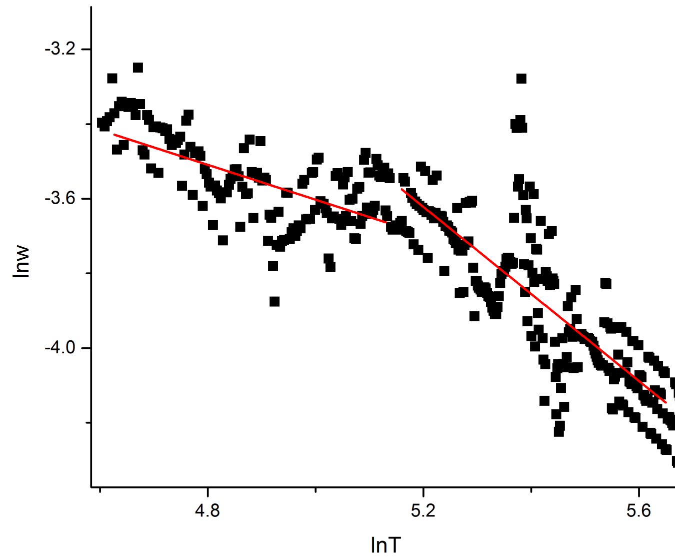


Figure 6.3: Zabrodskii-Zinov'eva analysis of device A in virgin state.

It is interesting to note the very evident fact that the resistance of device A in the virgin state, that we interpret as not featuring pinholes, is very dependent on temperature and thus we can conclude that no single step tunneling is taking place. So, we can consider either hopping mechanisms or Richardson-Schottky injection in the insulating barrier. We exclude *a priori* Richardson-Schottky phenomena, where the resistance is given by the interface barrier, because of the observed metallic paths in STO created with forming pulses [19] – if the behavior of the resistance were determined by the interface, so would the the resistance of the filamentary path in the device and thus the this path could not be metallic. Because of this inconsistency it is justified to consider only hopping mechanisms through the amorphous insulator. Hopping through such insulator is possible because of the strong defect structure formed by oxygen vacancies that are able to harbor electrons hopping from one part of the barrier to the other.
Fitting device A's virgin state with nearest-neighbor hopping (NNH), Mott variable-range hopping (M-VRH) and Efros-Schklovskii variable range hopping (ES-VRH) doesn't give good fits. To further analyze the device in this state, I used Zabrodskii and Zinov'eva's approach to studying hopping mechanisms shown in subsection 2.3.6, computing the function

$$W(T) = \frac{\mathrm{d}\ln R(T)}{\mathrm{d}\ln T}.$$

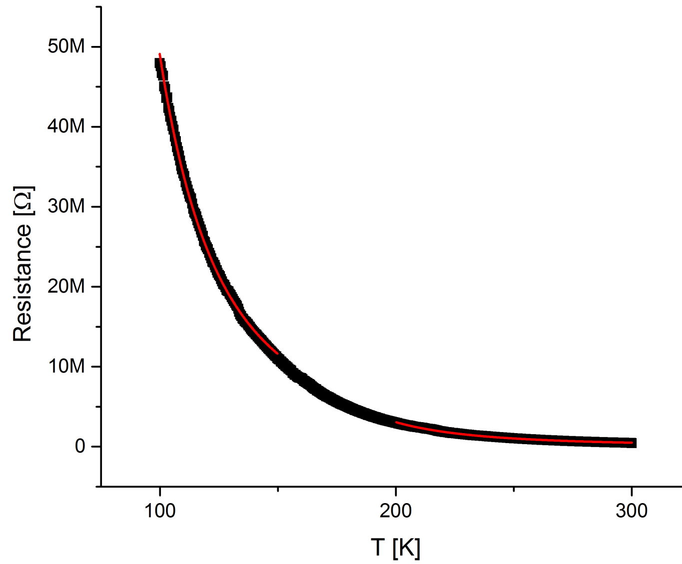


Figure 6.4: Fit of device A in the virgin state, from 100 K to 150 K the fit is ES-VRH and from 200 K to 300 K the fit is NNH.

By plotting $\ln W(T)$ vs $\ln T$, in the regions where the resistance follows the law

$$R \propto exp(-T_0/T)^s$$

(where $s = 1$ for NNH, $s = 0.5$ for ES-VRH and $s = 0.25$ for M-VRH), the resulting plot is a straight line with slope $-s$. The latter plot for device A in the virgin state is in fig. 6.3. The main sources of noise in this plot are temperature instability during the sweep from 100 K too 300 K and the very high density of points (because of the deriving algorithm). From 300 K to 175 K (where $\ln T = 5.17$) the plot can be clearly fitted with a downwards line, giving a slope of $s = 1.18$, indicating NNH respectively. At temperatures lower that 175 K it is more difficult to interpret the plot, so I tentatively used ES-VRH hopping as a working hypothesis since fitting from 175 K o 100 K gives a slope of $s = 0.45$. This is very similar to the crossover found in hydrogenated amorphous silicon by Yildiz et al [34] where the insulating junction showed NNH hopping above 220 K and ES-VRH for lower temperatures.
I fitted the resistance of device A from 100 K to 150 K the fit is ES-VRH and from 200 K to 300 K the fit is NNH (fig. 6.3). The $T_{NNH}$ is 1096 K, which gives an energy barrier between different states $W = 90$ meV, a very reasonable energy barrier. The characteristic temperature $T_{ES}$ from the low temperature fit is 6160 K, which is a temperature higher than those typically measured.

A good fit is not enough to prove that ES-VRH is applicable. We can compute

the localization length from this $T_{ES}$ from the formula in eq. 2.13 which gives us $\xi = 0.19$ nm (the dielectric constant at 100 K was taken from impedance spectroscopy measurements). This localization length is one order or magnitude less than those normally measured around 1 nm but this information alone is not enough to disprove that ES-VRH is actually happening. There are four criteria for the hopping parameter (Coulomb gap $\Delta_C$, mean ES-hopping energy $\Delta_{\text{ES}}$ hopping distance $R_{\text{ES}}$ and localization length $\xi$) already shown in subsection 2.3.4. The first is

$$\frac{\Delta_{ES}}{k_B T} = \frac{6^{1/2}}{2.8^{1/2}} \left(\frac{T_{ES}}{T}\right)^{1/2} \geq 1.$$

With our parameter, at 150 K, $\Delta_{\text{ES}}/k_B T = 12$.
Secondly,

$$\Delta_C > \Delta_{\text{ES}}$$

which gives

$$T < \frac{T_{ES}}{\pi 2.8^2}.$$

With our parameters $T_{ES}/(\pi 2.8^2) = 250$ K and since we see ES-VRH below 175 K the parameter $T_{ES}$ fits with criterion. The last two criteria concern the hopping length, which is given by the equation

$$R_{\text{ES}} = \frac{3^{1/6}}{2^{5/6} 2.8^{1/2}} \left(\frac{T_{ES}}{T}\right)^{1/2} \xi$$

that gives us $R_{\text{ES}} = 0.48$ nm. This hopping length satisfies the last two requirements,

$$d \gg R_{\text{ES}}$$

($d$ is the thickness of the device), and

$$R_{\text{ES}} > \xi,$$

but it is still a problematic length since it is only slightly more than the cubic cell parameter of STO (0.390 nm). To further prove the validity of this crossover one would have to compute the crossover temperature $T_C = W\xi/(rk_B)$, where $r$ is the NNH distance defined by

$$r = \left(\frac{4\pi N_d}{3}\right)^{1/3}$$

where $N_d$ is the carrier concentration, and compare the obtained value with the measure crossover temperature of $\approx 175$ K Unfortunately we were not able to measure the carrier concentration $N_d$.
For the sake of completeness, the $R(T)$ curve was fitted with M-VRH, both in the

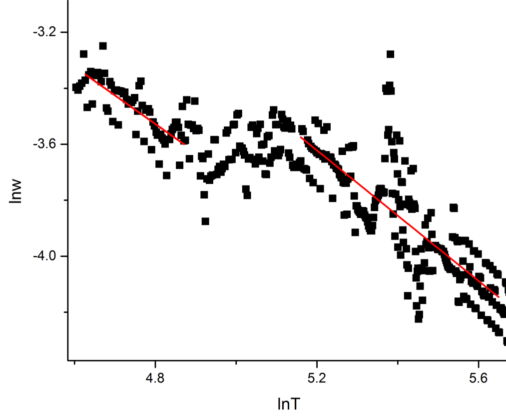


Figure 6.5: Zabrodskii-Zinov'eva analysis of device A in the virgin state: from 100 K to 130 K and from 175 K to 300 K the resistance follows two different nearest neighbor hopping regimes with a transition in the middle (which could also be an instrumental error).

whole temperature region and in the two different regions, giving very high $T_M$ parameters, the lowest of which is $T_M = 4 \times 10^6$. Since the requirement for M-VRH conduction

$$\Delta_{\text{Mhop}} > 2\Delta_C$$

implies [37]

$$T > T_M/465,$$

and since $T_M/465 \approx 10^4$ for the lowest $T_M$, we can conclude that no M-VRH is taking place in the STO junction.

In conclusion, the crossover from ES-VRH to NNH conduction at $\approx$ 175 K is consistent with their respective theories, but the low localization length $\xi$ and ES hopping distance $R_{\text{EShop}}$ together with the the fact that ES-VRH is rarely seen above 100 K strongly suggest that it is not a realistic transport mechanism. The Zabrodskii-Zinov'eva analysis can be interpreted in a more realistic manner by considering NNH from 300 K to 175 K and the again from 130 K to 100 K, since the latter region is clearly a straight line, giving $s = 1.01$, obviously compatible with NNH (fig. 6.5). What happens between 130 K and 175 could be simply instability during the temperature sweep, but I also report another device, this time with 25 nm thick a-STO, that similarly cannot be fitted with NNH in the whole 100-300 K region but has realistic fits in two separate temperature regions (fig. 6.6.

In conclusion, I have shown crossover from NNH to ES-VRH hopping conduction in pinhole-free a-STO junctions is consistent with the theory but it is physically unrealistic. I thus propose that transport in a fully insulating a-STO junction is essentially

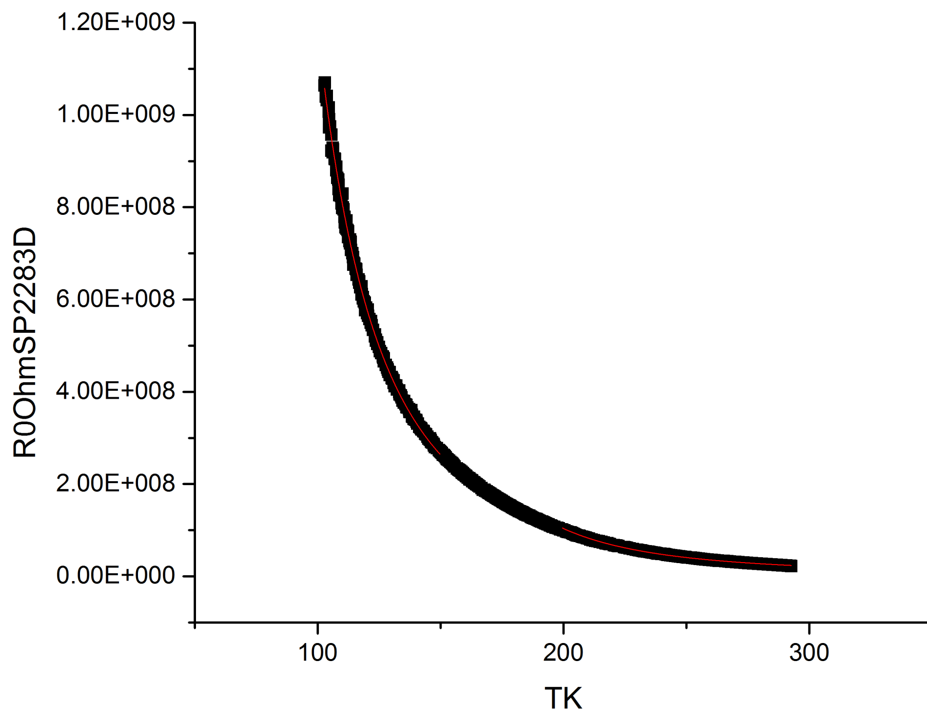


Figure 6.6: Fit of 25 nm thick device in the virgin state, from 100 K to 150 K the fit is NNH and from 200 K to 300 K the fit is again NNH, but the curve cannot be fitted with NNH in the whole temperature region.

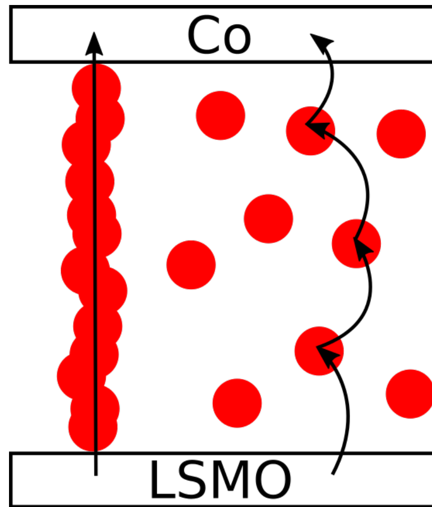


Figure 6.7: Schematic of the parallel model. The red dots are defects containing oxygen vacancies; forming pulses create dense networks of defects that form a conducting path from one electrode to the other.

NNH with a mid-temperature region showing a transition which should be subject of further study. This is a new result, both interesting for fundamental studies of this interesting material and because this knowledge will be useful to study conduction in the memristive a-STO spin-valves presented in the next subsection.

### 6.1.2 Parallel circuit model in a-STO junctions

To interpret the transport in device A after the formation of metallic filaments through forming pulse, we use the model first proposed by Ventura et al. [29], a parallel circuit between a metallic, filamentary pathway and and either a hopping pathway, so that the resistance of the device is given by

$$\frac{1}{R_d(T)} = \frac{1}{R_m(T)} + \frac{1}{R_h(T)}. \tag{6.1}$$

In this case, as proposed by Nili, the filaments are made of networks of defects that can accommodate oxygen deficiencies along their path; these pathways in insulating oxides can actually be metallic as reported by many groups [19] [39]. But how can electron behave as if they were inside a metal, while they are inside an insulator? The fact that oxygen vacancies in STO create localized states inside the insulating barrier has been shown [40]. If these states are far away from each other, electrons hop from one state to the other. Mott argued that if the hopping length is comparable to the effective Bohr radius of these localized states, a metallic band is formed inside the insulator. I propose that oxygen vacancies, normally distant enough so that electron transport in the insulator is hopping, can form filamentary paths that can act like

metals because of these considerations.
The forming pulse creates these paths and controlling the oxygen vacancy along these pathways is the means through which resistive switching is performed (this will be studied in the following chapter). Since forming pulses can be with both positive and negative voltages, these defect networks can be formed by electrons heating the a-STO junction and locally creating defects where the oxygen vacancies collect and alter the stoichiometry with a redox process [33]. As stressed by Nili et al., the formation of these filaments has to do with the amorphous nature of the junction since it facilitates the creation of such extended defect network .

The main idea behind this treatment is schematized in fig. 6.7. As previously stated, this model is extremely simple but works simply with the assumption that geometrical effect are irrelevant and that the two channels are independent (i.e. we ignore hopping from an electrode to the pinhole and, vice versa, hopping from somewhere in the pinhole to an electrode). Also, while the whole area of the device featuring hopping can be simply considered as a single channel, it is simplistic to considered the parallel between different metallic paths as a single metallic pathway. Still, the model is able to reproduce and explain many observed phenomena in devices with conducting paths through insulating materials (either pinhole made of electrode percolations or filamentary paths created by electroforming pulses).
As already stated in chapter 3, the only clear way to distinguish between conduction in pinholes and tunneling in insulating junctions is the temperature dependence, this model will be applied to the measure $R(T)$ to show its validity.
The low resistance state of the previously studied device A can be interpreted with this model. The temperature dependence of the resistance of the metallic channel is linearly increasing

$$R_m(T) = R_{m0} + mT$$

and the hopping channel is simply a NNH channel

$$R_h(T) = R_{h0} \exp(-T_0/T).$$

While I have shown that there is a crossover from NNH to ES-VRH at $\approx 175$ K, for this treatment it is reasonable to ignore the ES-VRH conduction al low temperatures. At low temperatures, if there is a metallic path significantly modifying the resistance of the device, the resistance of this channel is low while the resistance of the hopping channel is exponentially increasing. So, if

$$R_h \gg R_m$$

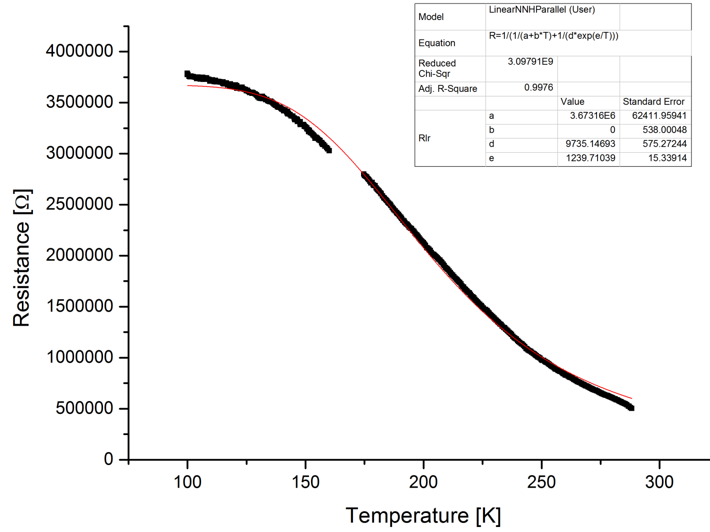


| Model | LinearNNHParallel (User) | | |
|---|---|---|---|
| Equation | R=1/(1/(a+b*T)+1/(d*exp(e/T))) | | |
| Reduced Chi-Sqr | 3.09791E9 | | |
| Adj. R-Square | 0.9976 | | |
| | | Value | Standard Error |
| Rlr | a | 3.67316E6 | 62411.95941 |
| | b | 0 | 538.00048 |
| | d | 9735.14693 | 575.27244 |
| | e | 1239.71039 | 15.33914 |

Figure 6.8: Fit of the low resistance state of device A with the parallel circuit model, with a linear metallic resistance and a NNH channel.

then

$$\frac{1}{R_h} \ll \frac{1}{R_m}$$

and thus

$$\frac{1}{R_d} = \frac{1}{R_h} + \frac{1}{R_m} \approx \frac{1}{R_m}.$$

This behavior is commonly observed in such devices. On the other hand, the resistance of the metallic channel is only growing linearly, so this approximation is not viable at high temperatures and even if hopping is the dominant mechanism since the metallic channel can significantly modify the $R(T)$ curve of the device.

I fitted the low resistance $R(T)$ of device A, with the constraint that $R_{m0}$ and $m$ be $> 0$. The fit is in fig. 6.8. While it is a good fit, the parameter $m$ converged to 0 giving a constant resistance of the metallic region. This is because in the temperature region where we measured the resistance NNH conduction is always dominating and even if the metallic filament actively modifies the total resistance we do not have enough data. It is still interesting to note that the parameter $T_{ES}$ changed from 1096 K to 1240 K. This is consistent with the observed change in oxygen concentration after a forming pulse in a-STO devices [19].

In the rest of this subsection I will analyze another device (B). This device presented a forming pulse at 100 K from from 1.3 MΩ to 18 kΩ (fig. 6.11). I then studied the temperature stability of the states after the initial forming pulse of the devices: I acquired $R(T)$ curve sweeping the temperature from 300 K to 80 K, where the device's resistance was 22 kΩ, at that temperature I lowered the device's resistance with a 0

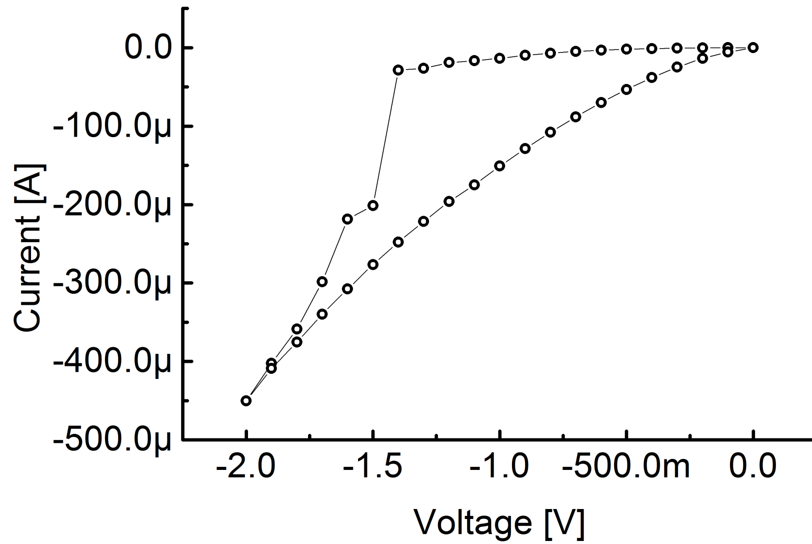


Figure 6.9: $I - V$ showing the forming pulse to 18 kΩ at 100 K of device B.

V → 4 V sweep to 3 kΩ. At that point I swept the temperature to 300 K and then back to 80 K where the device was at 18 kΩ. This behavior was observed in most devices: after the initial forming pulse, which we interpret as the creation of the oxygen vacancies defect filaments, the resistance of these filaments can be lowered further in a way that is irreversible only by increasing the temperature. This suggests that the mechanism is a modification of the filament is oxygen vacancies moving to the filament and thus lowering its resistance and the temperature instability is thermally assisted detrapping of oxygen vacancies from the filament to the LSMO electrode (the Co electrode oxidizes but no $CoO_x$ is in contact with the a-STO junction so we can assume that the relevant oxygen vacancy migration is from the LSMO electrode). $R(T)$ curves of such unstable devices typically show sudden increases of resistance (see fig. 6.12). For clarity, I will refer to forming pulse only as the thermically-irreversible creation of filaments and not to these thermically-reversible modification of the filament's resistance. To test this idea further, I brought third device (C) to a formed, low resistive state by applying a 0-4 V voltage sweep after the initial forming pulse. Device B was already in a thermically stable state (i.e., after the forming pulse the device was brought back to room temperature and then brought back to 100 K). At this point I brought both the devices to a certain $T_0$ and, after the devices had thermalized, brought them back to 100 K, measuring their resistance after the devices had thermalized again. The result of these measurements is in fig. 6.10: device B in the already stable state randomly changed the measured resistance by less than 10% while device C, in the unstable state, increased it measured resistance at 100 K by 20%.

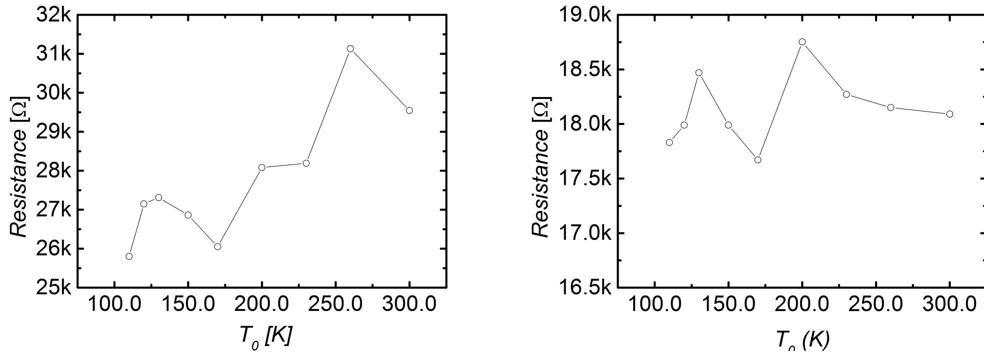


Figure 6.10: Temperature stability tests of device C in low resistance state by applying a 0-4 V voltage sweep after the initial forming pulse (left) and device B in a thermically stable state, the procedure is described in this section.

Thus, reliable $R(T)$ fits can only be made from thermally stable states since we can assume that the characteristics of the two channels and thus their parameters are changing while the temperature is rising, giving unreliable fitting parameters. Fitting the (1) state from fig. 6.11 using a NNH mechanism as a hopping channel and a linearly increasing resistance as the metallic channel doesn't give good results. This is because at low temperatures the curve is concave-up while the fitting function can only be concave-down, so we need to consider more complicated scattering mechanisms that can give rise to a concave-up $R(T)$ of the metallic channel so that the whole parallel can be concave-up.

Any kind of impurity of surface scattering mechanisms that the electrons can be subject to would have temperature-independent mobility and so it would only add a constant to the resistance. There are two remaining mechanisms: electron-electron scattering and the full Bloch-Grüneisen treatment of electron-phonon scattering. Since the former has never been observed at such temperatures, even in one-dimensional systems (even though such could be a valid subject of study), we will ignore it even though it can give reasonable fits in some devices. The Bloch-Grüneisen formula [38]

$$R(T) = C\left(\frac{T}{T_D}\right)^5 \int_0^{T_D/T} \frac{x^5}{(e^x - 1)(1 - e^{-x})}, \tag{6.2}$$

$T_D$ being the Debye temperature, is the most general treatment of electron-phonon interaction. This $R(T)$ starts to deviate from linearity only when $T \ll T_D$. During the writing of this thesis, I received another confirmation of the validity of this treatment from an article from Hueso's group [39] where "leaky" 1.2 nm $AlO_x$ junctions were studied (for their use in organic semiconductor spin valves). The measured $R(T)$ curve of such junction is in fig. 6.13. The junctions present metallic feature and are another example of oxide junctions with conductive filaments. We can clearly see a

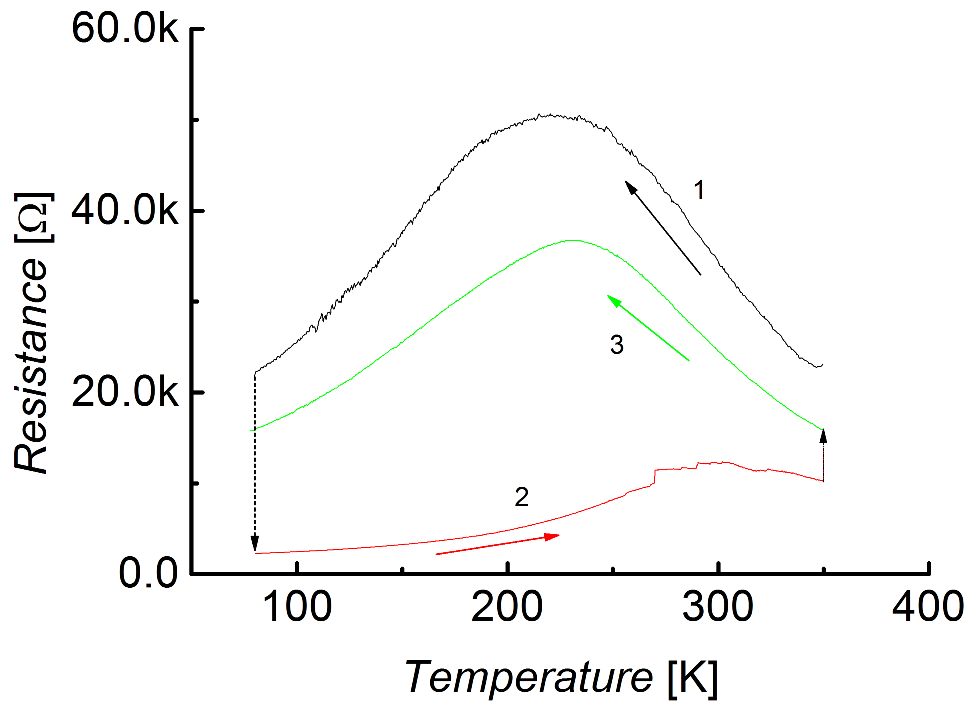


Figure 6.11: $R(T)$ curves of three different states of device B. The colored curves indicate the direction of the temperature sweep, the dashed downwards arrow indicates the 0 V $\rightarrow$ 4 V sweep that lowered the resistance to 3 k$\Omega$ and the upwards dashed arrow indicates that the resistance increased by itself during the two hours between the two temperature sweeps.

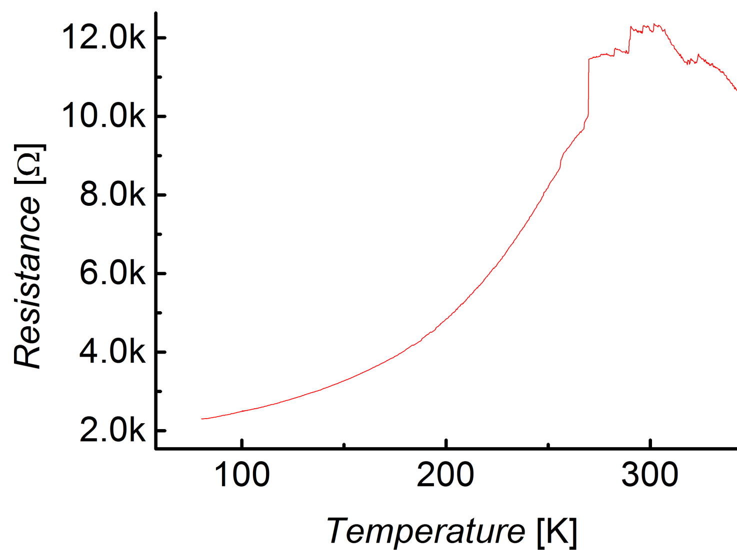


Figure 6.12: $R(T)$ curves of different state 2 of device B.

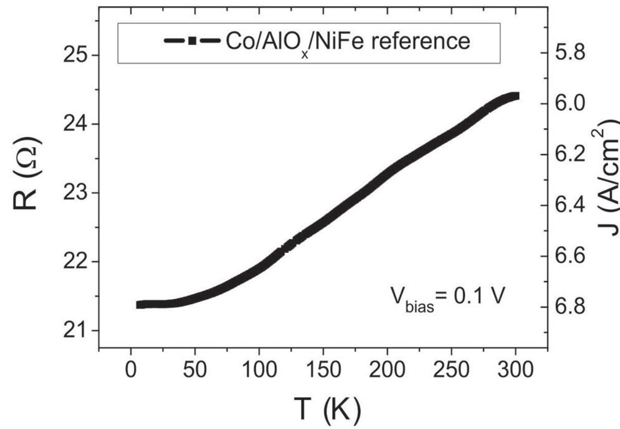


Figure 6.13: Temperature dependence of the resistance of an $AlO_x$ junction, confirming the metallic behavior of the $AlO_x$ "leaky" barrier. [39]

Bloch-Grüneisen trend of the resistance. In this particular $AlO_x$ junction we only see a metallic trend of the resistance; this means that the resistance of such channel is so low that the parallel circuit model in this case is simply a short-circuit through this very low resistance channel.

A fit of the temperature dependence of state 1 of device B using a parallel between BG and NNH is in fig. 6.14. The fitting parameters are reasonable: the $T_{NNH}$ of the NNH channel is 1580 K, giving an energy barrier between hopping states $W$ of 18 meV. The Debye temperature of the metallic channel is 562, which is very close to the epitaxial STO $T_D = 513$ K [41]. One has to be cautious while comparing the two temperatures. On one hand the electrons traveling in the approximately one-dimensional filament can interact with bulk phonons from the rest of the junction, which is amorphous. On the other hand the interaction with phonons can be with the one dimensional phonons in the filament (the electrons are metallic, so are able to form band structures and thus we can assume these one dimensional phonons exist) but their is no clear link between the $T_D$ of such filament and the $T_D$ of the bulk material. A fit of the temperature dependence of state 3 of device B is in fig. 6.15. In this state $T_D = 714$ K and $T_0 = 1710$ K, so both parameters have increased from the fit of the previous state.

Again we used only NNH conduction as the hopping channel ignoring the crossover to ES-VRH. From the fits of state 1 of device B we have $R_h/R_m = 3 \times 10^{-3}$ at 150 K, and since so we can effectively say that $R_d \approx R_m$ in the temperature region of the crossover to ES-VRH and so the crossover has no actual relevance on the resistance of this device.

It has been previously suggested that the observed temperature dependence of such devices depends on the resistance of the LSMO electrode, which also features similar $R(T)$ curves with a maximum at 250-350 K because of polaron transport in

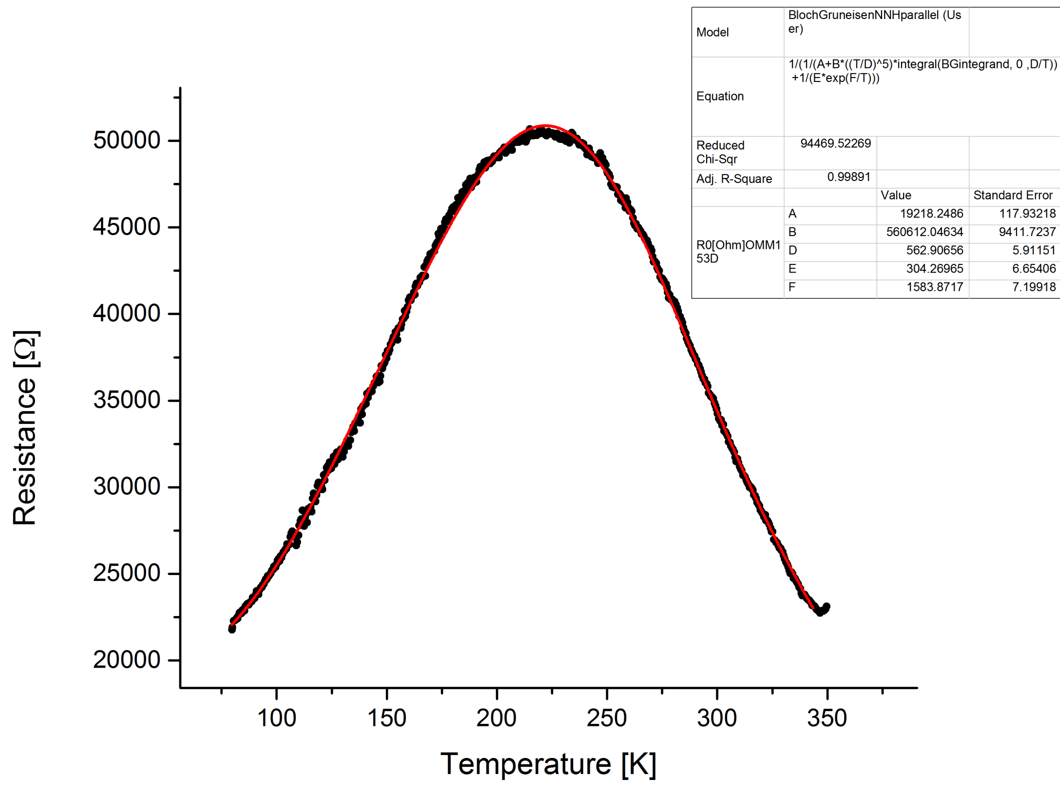


| Model | BlochGruneisenNNHparallel (User) | | |
|---|---|---|---|
| Equation | 1/(1/(A+B*((T/D)^5)*integral(BGintegrand, 0 ,D/T)) +1/(E*exp(F/T))) | | |
| Reduced Chi-Sqr | 94469.52269 | | |
| Adj. R-Square | 0.99891 | | |
| | | Value | Standard Error |
| R0[Ohm]OMM153D | A | 19218.2486 | 117.93218 |
| | B | 560612.04634 | 9411.7237 |
| | D | 562.90656 | 5.91151 |
| | E | 304.26965 | 6.65406 |
| | F | 1583.8717 | 7.19918 |

Figure 6.14: Fit of the temperature dependence of state 1 of device B using a parallel circuit between a Bloch-Grüneisen channel and a nearest neighbor hopping channel.

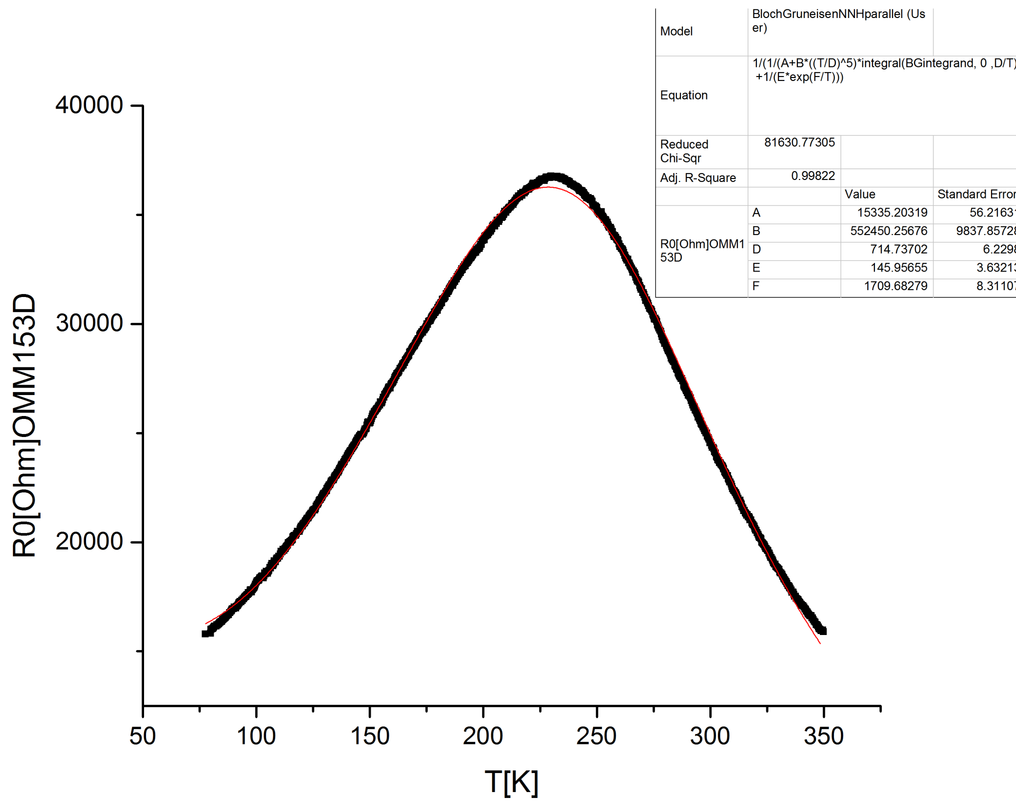


| Model | BlochGruneisenNNHparallel (User) | | |
|---|---|---|---|
| Equation | 1/(1/(A+B*((T/D)^5)*integral(BGintegrand, 0 ,D/T)) +1/(E*exp(F/T))) | | |
| Reduced Chi-Sqr | 81630.77305 | | |
| Adj. R-Square | 0.99822 | | |
| | | Value | Standard Error |
| R0[Ohm]OMM153D | A | 15335.20319 | 56.21631 |
| | B | 552450.25676 | 9837.85728 |
| | D | 714.73702 | 6.2298 |
| | E | 145.95655 | 3.63213 |
| | F | 1709.68279 | 8.31107 |

Figure 6.15: Fit of the temperature dependence of state 3 of device B using a parallel circuit between a Bloch-Grüneisen channel and a nearest neighbor hopping channel.

the LSMO [14]. Similar temperature dependences of the resistance have been reported by many groups [45] [46] [47]. These bumps in the $R(T)$ curve have been attributed to an ordering temperature of the LSMO/STO interface that is lower than the ordering temperature ($T_C$) of the bulk LSMO. If this were the case, one could observe a kink in the temperature dependence magnetoresistance at temperatures around the maximum of the $R(T)$. Also, this explanation relies on the presence of manganites but similar behaviors have been observed with different electrodes [29]. An LSMO/STO interface showing lower $T_C$ than that of the bulk LSMO has been considered mostly because of the fact that there is no correlation between the temperature of the maximum of the $R(T)$ of the device and of the LSMO electrode; on the other hand, devices with Alq3 junctions and LSMO electrode feature the same temperature dependence of the resistance. Lastly, as reported in this thesis, we have seen LSMO/STO/Co devices showing an entirely insulating-like $R(T)$. For these reasons, I propose the parallel circuit model as an explanation of the temperature dependence of such devices.

It has also been proposed that our a-STO device features polaron transport through the filaments; in this case we would have a net transition from a metallic conduction to hopping. It is important to stress that in our case, while similar to a transition from metallic conduction to hopping, is not the same as the polaron case. In the polaron model there is only one single channel where the conduction undergoes a transition and, at temperature far away from the transition the conduction is entirely either metallic or hopping. In our model, the two channel are always coexisting and the non-dominant channel can always influence the resistance of the whole device; as previously stated, at low temperature sufficiently far away from the "bump" of the $R(T)$ curve, since the hopping channel has exponentially rising resistance, the parallel circuit is essentially a short circuit through the metallic channel which completely dominates the conduction of the device. On the other hand the resistance of the metallic channel is only growing linearly, so this approximation is not viable at high temperatures and even if hopping is the dominant mechanism, the metallic channel can significantly modify the $R(T)$ curve of the device.

To test the parallel circuit model against the polaron one we can use the simple but powerful Zabrodskii-Zinov'eva approach: if the temperature is far away from the maximum of the resistance (the transition region) is hopping than this analysis would yield reasonable results confirming the polaron model. The result of the computation in the 250-350 K temperature region is in fig. 6.16. If there were temperature region with a pure hopping we would expect to see a linearly decreasing region in the $\ln W$ vs $\ln T$ plot. This is not the case (the last ten points are because of noise during the temperature sweep and anyway have a slope of -20 and could not be interpreted as hopping) so we can exclude polaron conduction in our device.

To further prove the validity of the model we are using we can still use the Zabrodskii-

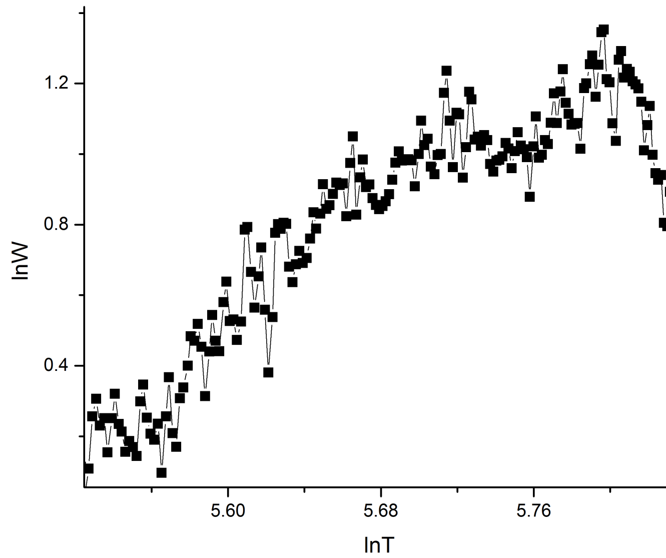


Figure 6.16: Zabrodskii-Zinov'eva analysis of the resistance of state 1 of the device B in the 250-350 K region.

Zinov'eva analysis: if we actually have a hopping channel in parallel to a metallic channel whose $R(T)$ curves is already known, we can compute the $R(T)$ of the hopping channel as

$$\frac{1}{R_h(T)} = \frac{1}{R_d(T)} - \frac{1}{R_m(T)} \tag{6.3}$$

where $R_d$ is the resistance of the whole device. As we have previously shown at low enough temperatures the resistance of the device is just the resistance of the metallic channel so fitting $R_d(T)$ in that region actually gives us the fit of $R_m(T)$. With these considerations in mind I fitted the $R(T)$ curve of state 1 of device B in the 80-150 K region with the Bloch-Grüneisen formula (eq. 6.2) plus a constant to account for temperature-independent scattering mechanisms and used eq. 6.3 to obtain the data of the resistance of the hopping channel in parallel to the metallic channel that I had just fitted. Computing $\ln W$ vs $\ln T$ in the 200-300 K region gives us linearly descending data and by fitting it we obtain $s = 0.94$, which indeed is a coefficient compatible to NNH.

Even though the inability to use $I - V$ fits to check for conductive channels inside an insulator has been shown in subsection 3.0.2, we can still use $I - V$ to test our parallel circuit model. In fig. 6.18 is the $I - V$ curve of device B at 300 K which is approximately linear, consistent with NNH that doesn't predict non-linear $I - V$ curves.

In fig. 6.19 are the $I - V$ curves of the same device, at 100 K, before forming pulse

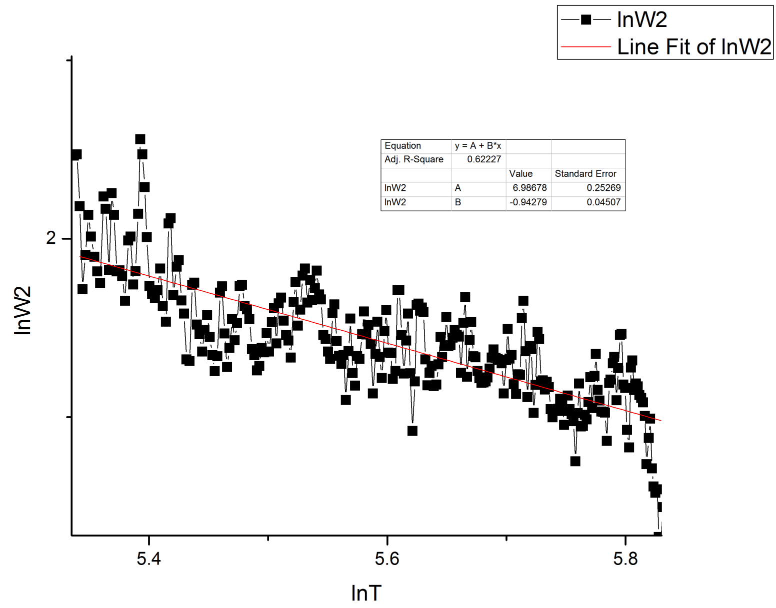


Figure 6.17: Zabrodskii-Zinov'eva analysis of the resistance of the extrapolated hopping channel of state 1 of the device B in the 200-330 K region.

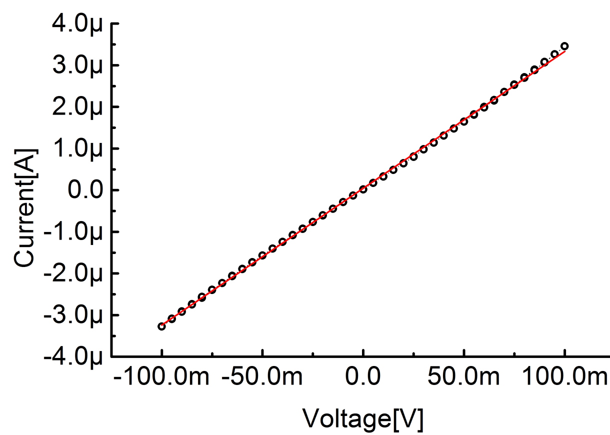


Figure 6.18: $I-V$ curve of device B at 300 K.

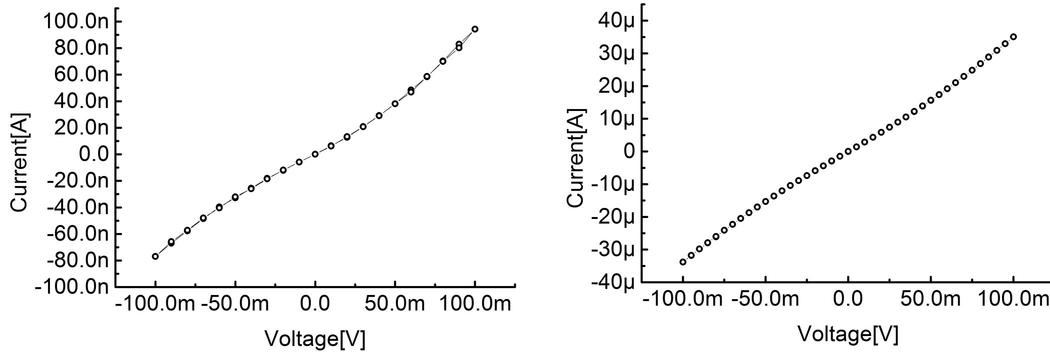


Figure 6.19: $I - V$ of the device B at 100 K in two different states.

and in its 3 k$\Omega$ state (state 2). Both are nonlinear, but why? The nonlinearity of filamentary conductive channel has been shown in MTJ to be simply a "parasitic" effect of the electrons that are tunneling and not passing through the pinhole. As reported in subsection 3.0.2, it has been computed that in an MTJ as much as 88% of the current can be passing through the pinhole while the device still has a differential conductance ($\mathrm{d}I/\mathrm{d}V$) with a positive curvature (such as these two $I - V$s); in general the more current is flowing through the pinhole, the lower is the normalized conductance (see fig. 3.4).

I computed the normalized different conductance for two different resistance states states, plotted in fig. 6.20. We can see that the lower resistance of the state has lower conductance: by lowering the resistance of the filamentary channel we change the ratio of current passing through this channel and thus we lower the normalized conductance. We can conclude that the $I - V$ curves of these filamentary devices both agree with previous experiments [24] and theory [25]. But where does the tunneling come from? In the parallel circuit model we have ignored tunneling: our devices have sufficiently high thicknesses so that electrons "prefer" to either hop through the oxygen vacancies or pass through the conductive filaments. At 100 K the resistance of the hopping channel is so low that it is almost as if it didn't exist (because $R_h \gg R_m$) and we can see the residual effects of tunneling only when measuring the conductances of our devices. Another possible explanation is that the conducting filaments do not completely short circuit the metal/oxide barrier and tunneling from the electrode to the filament, which cannot be probed with the temperature dependence of the resistance, is only visible from conductance measurements. This was also reported by Nili [19].

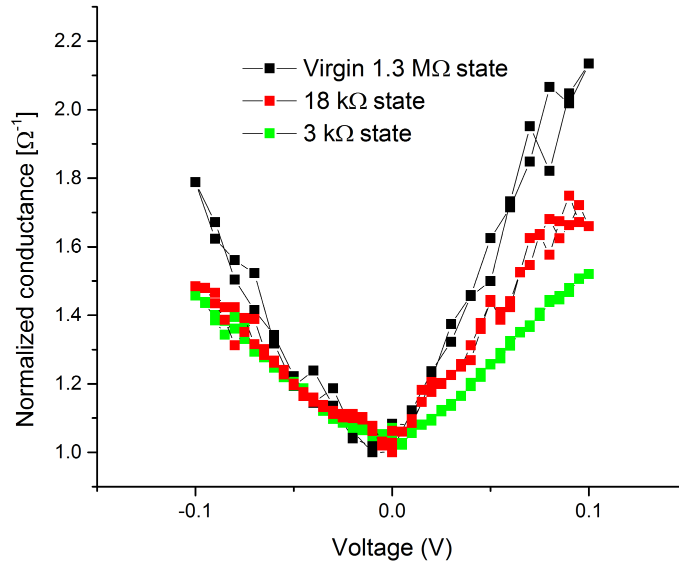


Figure 6.20: Normalized conductance of device B before forming pulse in a formed 18 kΩ state (state 3) and a formed 3 kΩ state (state 2).

## 6.2 Epitaxial STO devices

While crystalline STO was extensively studied by De Teresa, we wanted to use the techniques used in the previous part of this subsection on these devices to test these devices. Epitaxial STO is known to have filamentary paths of dislocations where oxygen vacancies can settle and create conductive filaments [42]. Because of this, we can use the parallel circuit model to study conduction trough these kinds of devices. While the e-STO devices we fabricated showed no memristor effect, it is still interesting to study the effects of filamentary conduction channels in these well known devices.

We fabricated 2.5 and 10 nm thick LSMO/e-STO/Co devices. The crystalline quality of the STO junction was verified with SEM measurements shown in chapter 5. We have seen no forming pulse in these devices but nonetheless the temperature dependence of the device suggests conductive channel in parallel to a tunneling/hopping channel as with the a-STO devices. We exclude nearest neighbor hopping and variable range hopping as they are mechanisms seen in amorphous and disordered system. We also exclude Richardson-Schottky for the same reason as with the a-STO device: if the behavior of the resistance were determined by the interface, so would the the resistance of the filamentary path in the device and thus the this path could not be metallic.

In fig. 6.21 is show the temperature dependence of the resistance a a 10 nm thick e-STO junction and a fit with the parallel circuit model, using Bloch-Grüneisen as one resistance and Richardson Schottky as the other. It is a good fit by itself: the

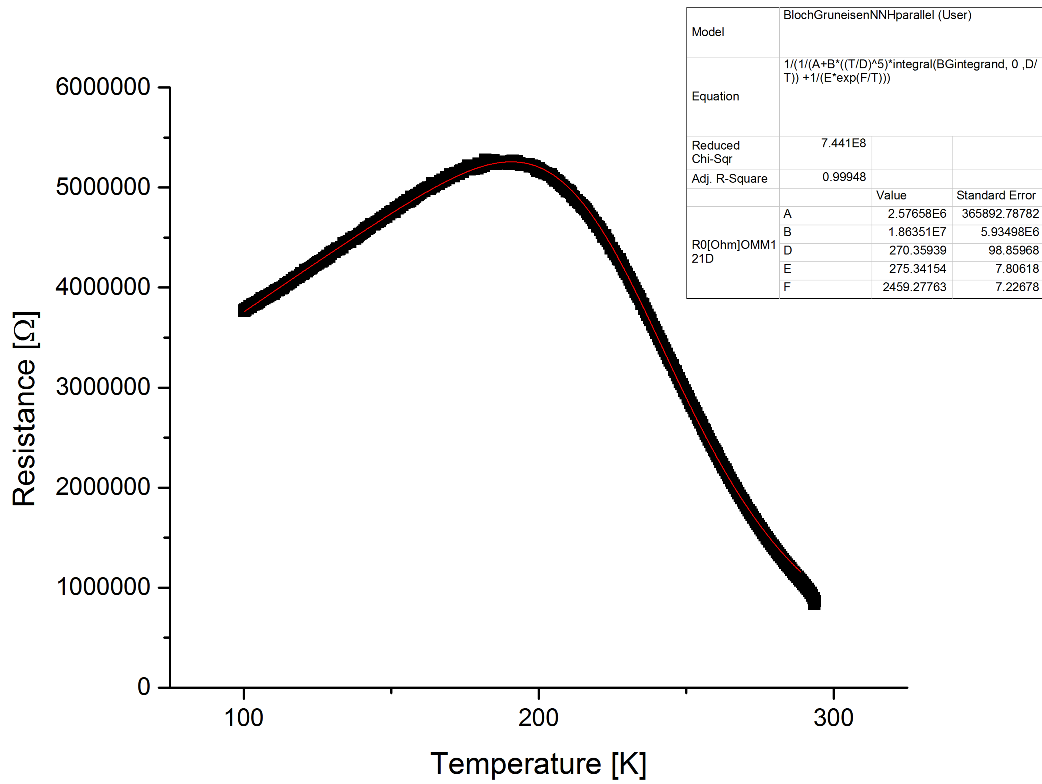


| | | | |
|---|---|---|---|
| Model | BlochGruneisenNNHparallel (User) | | |
| Equation | 1/(1/(A+B*((T/D)^5)*integral(BGintegrand, 0 ,D/T)) +1/(E*exp(F/T))) | | |
| Reduced Chi-Sqr | 7.441E8 | | |
| Adj. R-Square | 0.99948 | | |
| | | Value | Standard Error |
| R0[Ohm]OMM121D | A | 2.57658E6 | 365892.78782 |
| | B | 1.86351E7 | 5.93498E6 |
| | D | 270.35939 | 98.85968 |
| | E | 275.34154 | 7.80618 |
| | F | 2459.27763 | 7.22678 |

Figure 6.21: $R(T)$ of a 10 nm thick LSMO/e-STO/Co device and a fit with a parallel of a Bloch-Grüneisen channel and a Frenkel Poole emission.

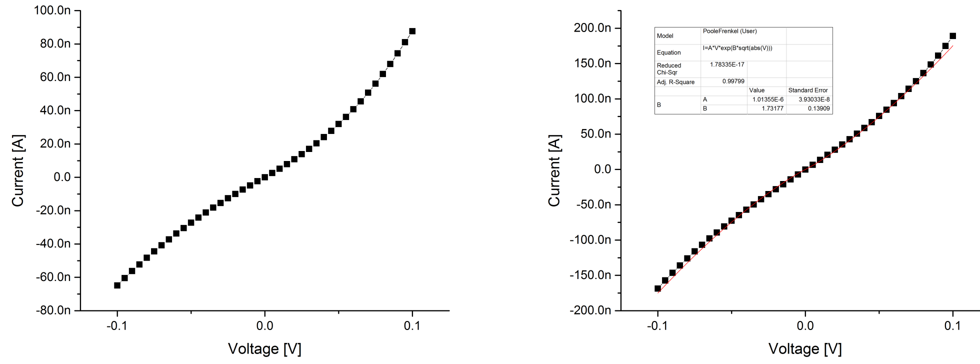


Figure 6.22: $I - V$ of the 10 nm e-STO device at 100 K (left) and 300 K (right) fitted with Poole-Frenkel.

Debye temperature $T_d$ is 270 K (we could have used a linearly increasing resistance giving the same fit) and the characteristic temperature

$$T_0(V) = e(\phi - \sqrt{eV/d\pi\epsilon_0\epsilon_R})/k_b,$$

where $\phi$ is the energy barrier that an electron must cross to move from one atom to another in the crystal, $d$ the thickness, in this fit is $k_bT_0(V) = 0.211$ eV. With our values $\sqrt{eV/d\pi\epsilon_0\epsilon_R} = 0.002$ eV $\ll \phi = 0.211$ V and thus the $e\phi \approx k_bT_0 = 0.211$ eV. This is a reasonable energy barrier, but it is genuine Poole-Frenkel effect we must also fit the $I - V$s (eq. 2.19).

The fit at 300 K with the Poole-Frenkel $I - V$ is in fig. 6.22. It is a good fit, but computing the $\epsilon_R$ from the fitting coefficient

$$B = \frac{e\sqrt{e/d\pi\epsilon_0\epsilon_R}}{k_bT}$$

gives $\epsilon_R = 1.4$. While I was not able to obtain a $\epsilon_R$ of the e-STO junction (our impedance spectroscopy instrument only worked in two-contact mode and because of the high resistance of the LSMO electrode, which features capacitance effect because of grain boundaries, overshadowed the lower resistance of the e-STO junction), at room temperature this value is typically $\epsilon_R = 300$ and thus conclude that this is not a genuine Poole-Frenkel conduction.

We suggest that in parallel to the conducting filament channel is simply tunneling: this would explain the non-linear $I_V$ of the device at 300 K (the conductance of a tunneling channel increases with bias, as carriers see an effectively narrower trapezoidal barrier.). The strong temperature dependence of tunneling channel could be because of the temperature dependence of the LSMO electrode and of the LSMO/STO barrier.

# Chapter 7

# Memristive and spintronic amorphous STO devices

In this chapter I will show the memristive and spintronic properties of the devices reported in the previous chapter.

Device C, after the initial forming pulse, showed bipolar resistive switching (fig. 7.1), switching reversibly from 90 kΩ to 136 kΩ (read at -0.1 V), lowering its resistance at 1.7 V and increasing it at -1.3 V. To check the polarity of the switching, after lowering the resistance at positive voltages (1.7 V) I applied even higher voltages (2.5 V) and measured the resistance again, with no significant changes. After increasing the resistance at negative voltages (-1.3 V) I applied even lower voltages (-2 V) and measured the resistance at the same bias, with no significant changes. This procedure is shown is fig. 7.2. After a resistive switch at negative voltages, applied another negative pulse shown no kind of hysteretic behavior while after a resistive switch at positive voltages the current saturated to compliance, but a successive resistance measurements showed no signs of change.

To test the stability of the device I applied a SET LOW voltage (2 V), then 0 bias (to avoid non-volatile effects) and then a READ voltage of -0.1 V was applied ten times, measuring the resistance, and then setting the bias to 0 after every READ. Then the SET HIGH (-1.6 V) was applied and the resistance read ten times like previously described. The result of this measurement is in fig. 7.3. Unfortunately this device isn't very stable.

The same bistability was seen in device A (fig. 7.4. Like the previous devices, this resistive switching is bipolar, with the same polarity (positive voltage lower the resistance and negative voltages lower it) and it is entirely non-volatile. The same stability test were carried out with better results (fig. 7.5).
The voltage is applied with the Co electrode as the ground, so the decrease of the resistance at positive voltages and the increase of the resistance at negative voltage is

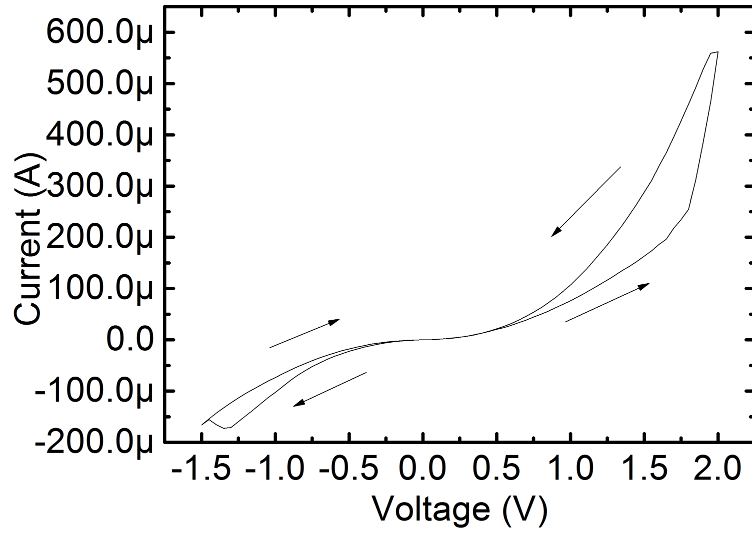


Figure 7.1: $I-V$ measurement showing the bipolar resistive switching of an LSMO/a-STO/Co device (C).

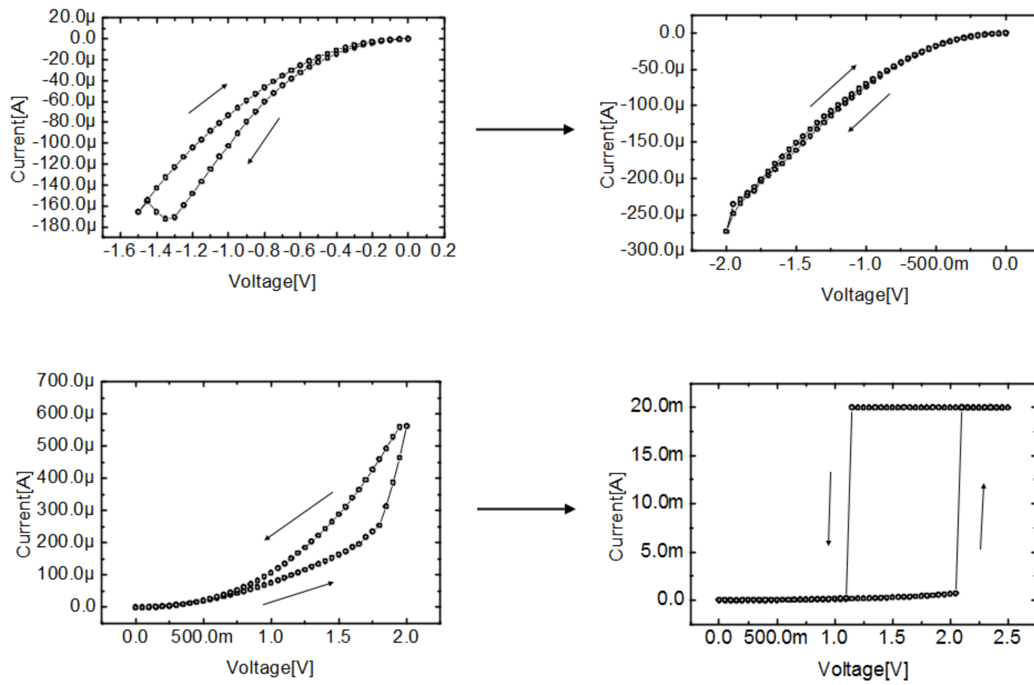


Figure 7.2

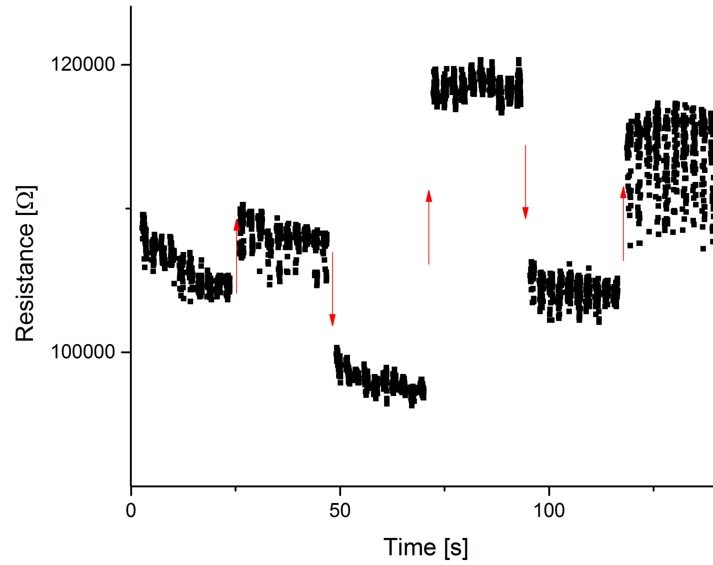


Figure 7.3: Stability test of the bipolar resistive switching of device C: the arrows indicate SET HIGH and SET LOW voltages and the data is the subsequent measurement of the resistance at -0,1 V.

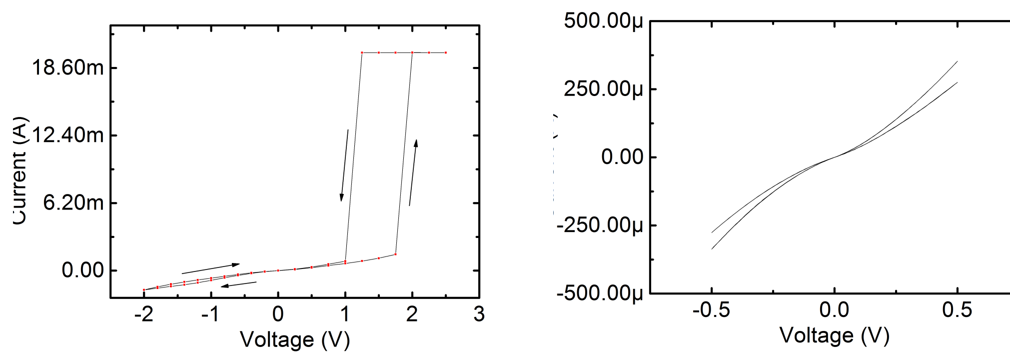


Figure 7.4: $I-V$ showing bipolar bistability (left) and comparison between the $I-V$ curves in the two different states.

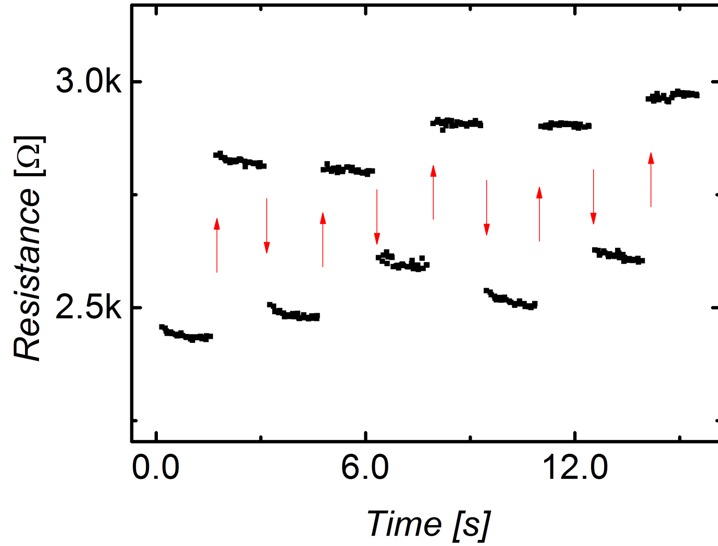


Figure 7.5: Stability test of the bipolar resistive switching of device B: the arrows indicate SET HIGH and SET LOW voltages and the data is the subsequent measurement of the resistance at -0,1 V.

consistent with oxygen vacancies transported from the LSMO electrode to the STO junction and vice versa, since the increase in concentration of oxygen vacancies lowers the resistance of the metallic filament. We also cannot exclude that oxygen vacancies diffuse in the rest of the STO junction and thus changing the properties of the hopping channel. Because of the low OFF/ON resistance ratio ($\approx$ 115%), we can say that unlike the results of Jang [12] and Nili [19], this is not the creation of annihilation of the metallic filament but only a modification.
OFF/ON ratio can be improved by controlling the oxygen vacancy concentration in the $SrTiO_3$ junction; we expect to do this by growing the amorphous $SrTiO_3$ in argon and oxygen atmosphere instead of an oxygen atmosphere. Changing the LSMO electrodes with other ferromagnetic materials (for example permalloy, $Ni_{.80}Fe_{.20}$) may also improve the resistive switching properties of the devices since oxygen vacancy diffusion also depends on the metal/oxide interface properties.

I will now show the spintronic properties of the amorphous STO devices and their correlation to the resistive switching. While devices A and B showed no spin valve effect in any of the resistive states, device B showed both spin valve magnetoresistance and an interesting interplay between magnetoresistance and resistive switching.

Device B, after forming pulse, in its low resistance state showed a magnetoresistance represented in fig. 7.6. We can clearly see a negative spin valve magnetoresistance (SVMR = 1.1%) with coercitivities 80 Oe and 1100 Oe. The coercitivies of the LSMO and Co electrode are measured from the AMR (the increase of resistance when apply-

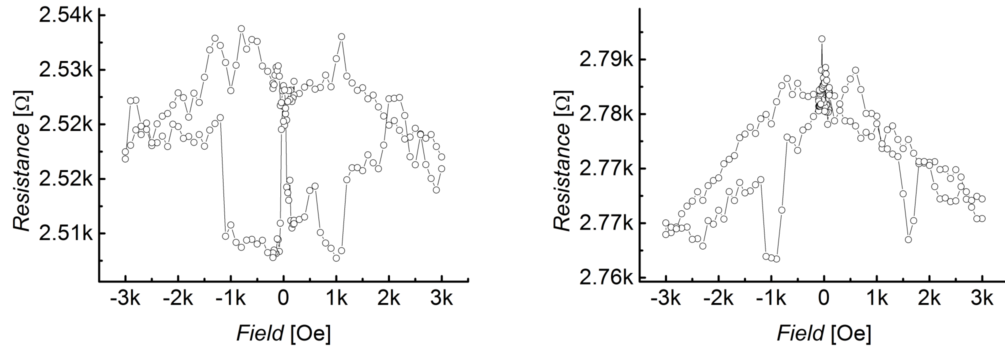


Figure 7.6: Magnetoresistance measurements of the low resistance state (left) and high resistance state (right) of device B.

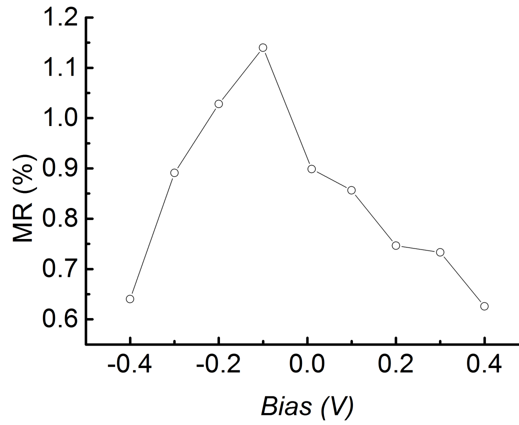


Figure 7.7: Bias dependence of the inverse SVMR of device A.

ing a magnetic field with the magnitude of the coercive field, respectively parallel and perpendicular to the current) and are respectively 50 Oe and 1100 Oe. The fact that these two sets of coercivities do not match is commonly observed but not yet explain; one hypothesis is that the transport is not from states with bulk properties but from other states at the surface (for example, grain with different coercitivies because of their shape or oxidized regions of the electrodes). The maximum of the SVMR is at -0.1 V. The full voltage dependence of the MR is in fig. 7.7.
In its high resistance state, the device showed a clear modification of the magnetoresistance: no clear SVMR is seen but only an almost-linear decrease of the resistance with the applied field. We have regularly seen what could look like SVMR with very high coercive fields. These signal were not reproducible and appear to be some noise of unknown origin. The linear decrease is also commonly observed in device with LSMO electrodes and is not yet explained, but it is qualitatively similar to the CMR of the LSMO electrode (see fig. 2.8).

We can attribute the SVMR to the conductive filaments for two reason. In the

parallel circuit model, from eq. 6.1, we can compute the magnetoresistance of the whole parallel circuit as a first order modification of the resistance (MR $< 10\%$):

$$MR_d = \frac{MR_d \times R_h + MR_h \times R_m}{R_m + R_h}. \tag{7.1}$$

If the contribution of the hopping channel to the magnetoresistance of the device is comparable to the contribution of the metallic channel,

$$MR_d \times R_h \sim MR_h \times R_m$$

implies

$$\frac{MR_h}{MR_d} \sim \frac{R_h}{R_m}.$$

This ratio is of the order of $10^5$, computed from the fits from the previous chapter, at 100 K. Since the hopping mechanism would have to have unrealistically high magnetoresistances, and considering that

$$R_h \gg R_m$$

at 100 K, we can say

$$MR_d \approx MR_m.$$

As we have previously seen, resistive switching can be seen as the modification of the metallic channel of the device: in the low resistance state the device has a magnetoresistance that can be explained by BMR theory [30], in the high resistance state the filament is modified and lacks some oxygen vacancies compared to the low resistance state, giving this state a higher resistance. This modification is responsible for the disappearance of the spin valve magnetoresistance observed in this state, although it is interesting as to why such a small increase of the resistance can modify the transport of spin in the device.

The difference between the voltage dependence of our device and of the devices reported by De Teresa (fig. 2.12) is also to be noted. Since BMR and TMR are the matching of the electron wave function at both sides of the pinhole, the fact that we see negative MR can be attributed to the Co hybridization at the STO interface. We can attribute the difference of the voltage dependence to either a difference in stechiometry caused by the amorphousness (the TEM images suggest and abundance of Sr compared to Ti in the STO junction) and because of the effect of oxygen content on spin transport [45].

Since transport of spin is through an approximately one-dimensional metallic channel, the spin valve effect can be explained with BMR theory shown in subsection 3.0.4.

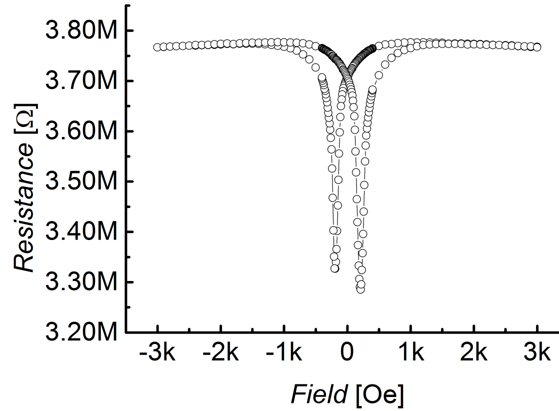


Figure 7.8: Magnetoresistance of a 10 nm thick e-STO device, at -0,1 V and 100 K.

The reason why the observed MRs are so low in magnitude is the because the length of the filaments, and thus their resistance, is too high. Thus phonon scattering is too high, lowering the spin diffusion length and thus lowering the observed SVMR. Devices with less resistive filaments may transport spin in a completely ballistic regime and thus have higher MR ratios. This may be observed both with devices with a higher concentration of oxygen vacancies in the STO junction, which we could achieve by fabricating the device in an argon atmosphere instead of an oxygen one. Lowering the thickness of the STO junction may also work, but it has to be noted that the interplay between resistive switching and spin valve works because if the electron is not transported through the metallic filament it is transported through hopping, a channel not featuring magnetoresistance. If we lower the thickness of the device, hopping may not favored and we may end up with a parallel circuit of metallic conduction and tunneling. Since tunneling also transports spin, the device could have a lesser interplay between the two effects.

We can use the parallel circuit model to interpret the magnetoresistance of the previously shown epitaxial STO junctions. At room temperature the device showed no SVMR because of the $T_C$ of the LSMO electrode is around room temperature. At 100 K it presented a clear spin valve signal magnetoresistance of 12% at -0.1 V, in fig. 7.8. This spin valve is negative as the previous devices for the same reasons concerning Co/STO interface hybridization. As we previously shown, from BMR we expect that a ballistic channel has the same magnetoresistance of a tunneling channel because the physics from which the two phenomena arise is the same. In we have a parallel circuit of two channels that feature the same magnetoresistance, the magnetoresistance of the whole device is the same as the two channels. If instead the metallic channel does not provide any magnetoresistance (perhaps because it is too long and the spin diffusion length is too low), then the effect of this metallic filament is to lower the magnitude,

but not any other property, of the magnetoresistance, following eq. 7.1: if the metallic channel has no magnetoresistance,

$$MR_d = \frac{R_m}{R_m + R_t} MR_t.$$

In our specific case, we do not have enough information on the temperature dependence of the tunneling channel and thus we can not quantify how the metallic filament modifies the magnetotransport properties of the junction.

# Conclusions

In conclusion, we have investigated $La_{0.7}Sr_{0.3}MnO_3$/amorphous-$SrTiO_3$ (5 nm)/Co devices featuring bipolar resistive switching, with the low resistance state showing a clear spin valve magnetoresistance that switches off in the high resistance state. Both the magnetoresistance and resistive switching are attributed to a complex interplay between conductive and hopping channels. The polarity of the bistable resistive switching is compatible with oxygen vacancy movement from and to the LSMO electrode and the sign of the observed magnetoresistance is consistent with previous theories concerning $SrTiO_3$/Co interface hybridization that modify the effective polarization of the electrode.
I have put significant effort in expanding a previously proposed model to account for metallic channels throughout the insulating $SrTiO_3$ junction. Using this model I have shown that the amorphous $SrTiO_3$ device acts like a parallel circuit between metallic channels whose resistance is described by the Bloch-Grüneisen formula and a nearest neighbor hopping channel. The magnitude of the magnetoresistance measured in the low resistance state is due to both on the quality of the interface between the $SrTiO_3$ junction and the electrodes and on the low scattering in the metallic filaments created by forming pulse. The magnitude of the OFF/ON ratio also depends on the quality of the metallic channels, presumably filaments. Both the magnetoresistance and the OFF/ON ratio can be improved by controlling the oxygen vacancy concentration in the $SrTiO_3$ junction and we seek to do this by growing the amorphous $SrTiO_3$ in argon and oxygen atmosphere instead of an oxygen atmosphere.
I have also provided a formula to compute the magnetoresistance of the parallel circuit between the metallic and the hopping/tunneling circuit (depending on the material of the device). This formula can account for and quantify how the metallic filament through the insulating junction can alter or degrade the spintronic properties of a magnetic tunnel junction.
In this thesis for the first time I show an $La_{0.7}Sr_{0.3}MnO_3$/$SrTiO_3$/Co device showing both magnetoresistance and resistive switching, using knowledge on one phenomenon

to interpret the other. This device is, to my current knowledge, the third reported device to feature both these effects. I have also expanded a previously proposed phenomelogical model to account for metallic filaments in an insulating junction and have used this model to study the reported devices. At the time of writing, I am currently working on applying this model on spin valves with Alq3 junctions as these devices feature many similarities to the amorphous $SrTiO_3$ devices. Since the scope of this thesis is both to show how such devices may be used for a computing compatible to beyond CMOS technology and to provide insight on the physics behind transport in $SrTiO_3$ junctions it is expected that this work will offer both ideas on the fabrication of multifunctional devices and on the charge and spin transport in such devices.

# Bibliography

[1] M. N. Baibich et al. *Giant Magnetoresistance of (001)Fe/(001)Cr Magnetic Superlattices.* Phys. Rev. Lett. **61**, 2472 (1988).

[2] G. Binash et al. *Enhanced magnetoresistance in layered magnetic structures with antiferromagnetic interlayer exchange.* Phys. Rev. B **39**, 4828(R) (1989).

[3] N. F. Mott *Electrical conductivity of transition metals.* Proc. Roy. Soc. A, **153**, 699-717 (1936).

[4] M. Julliere (1975). *Tunneling between ferromagnetic films.* Phys. Lett. **54A**, 225–226 (1973).

[5] B. Dieny, V. S. Speriosu, S. S. P. Parkin, B. A. Gurney, D. R. Wilhoit, and D. Mauri *Giant magnetoresistive in soft ferromagnetic multilayers.* Phys. Rev. B **43**, 1297(R) (1991).

[6] E. Y. Tsymbal et al. *Perspectives of Giant Magnetoresistance* published in Solid State Physics, ed. by H. Ehrenreich and F. Spaepen, Vol. 56 (Academic Press, 2001) pp.113-237.

[7] Chua, L. O *Memristor - the missing circuit element.* IEEE Trans. Circuit Theory **18**, 507–519 (1971).

[8] D. B. Strukov et al. *The missing memristor found.* Nature **453**, 80-83 (2008).

[9] L. Chua *Resistance switching memories are memristors.* Applied Physics A March 2011, Volume **102**, Issue 4, pp 765-783 (2011).

[10] M. Prezioso et al. *Electrically Programmable Magnetoresistance in Multifunctional Organic-Based Spin Valve Devices.* Advanced Materials **2011**, 23, 1371–1375 (2011).

[11] M. Prezioso et al. *A Single-Device Universal Logic Gate Based on a Magnetically Enhanced Memristor.* Advanced Materials **2013**, 25, 534–538 (2013).

[12] H-J. Jang et al. *Spin transport in memristive devices.* Appl. Phys. Lett. *100*, 043510 (2012).

[13] B. Nadgorny et al. *Origin of high transport spin polarization in* $La_{0.7}Sr_{0.3}MnO_{0}3$*: Direct evidence for minority spin states*. Phys. Rev. B 63, 184433 (2011).

[14] P. Graziosi et al. *Polaron framework to account for transport properties in metallic epitaxial manganite films*. Physical review B 89, 214411 (2014).

[15] J. M. De Teresa et al. *Inverse Tunnel Magnetoresistance in* $Co/SrTiO_3/La_{0.7}Sr_{0.3}MnO_3$*: New Ideas on Spin-Polarized Tunneling*. Phys. Rev. Lett. **82**, 4288 (1999).

[16] J. M. De Teresa et al. *Role of Metal-Oxide Interface in Determining the Spin Polarization of Magnetic Tunnel Junctions*. Science **286** (1999).

[17] R. Meservey and P. M. Tedrow *Spin-polarized electron tunneling* Phys. Rep. **238**, 173 (1994).

[18] E. Y. Tsymbal and D. G. Pettifor *Modelling of spin-polarized electron tunnelling from 3d ferromagnets*. J. Phys. Condens. Matter **9**, L411 (1997).

[19] H. Nili et al. *Nanoscale Resistive Switching in Amorphous Perovskite Oxide (a-*$SrTiO_3$*) Memristors*. Adv. Funct. Mater. **2014**, 24, 6741–6750 (2014).

[20] H. Nili et al. *Donor-Induced Performance Tuning of Amorphous SrTiO 3 Memristive Nanodevices: Multistate Resistive Switching and Mechanical Tunability*. Adv. Funct. Mater. **2015**, 25, 3172–3182 (2015).

[21] N. F. Mott and W. D. Twose *The theory of impurity conduction*. Advances in Physics **10**, 38 (1961).

[22] A. G. Zabrodskii and K. N. Zinov'eva **Low-temperature conductivity and metal-insulator transition in compensate n-Ge**. Zh. Eksp. Teor. Fiz. 86, 727-742 (1984).

[23] D. A. Rabson et al. *Pinholes may mimic tunneling* Journal of Applied Physics, **89**, 2786-2790 (2001).

[24] B. J. Jönsson-Åkerman et al. *Reliability of normal-state current–voltage characteristics as an indicator of tunnel-junction barrier quality*. Applied Physics Letters. **77**, 1870-1872 (2000).

[25] Z.S. Zhang and D. A. Rabson *Electrical and thermal modeling of the non-Ohmic differential conductance in a tunnel junction containing a pinhole*. Journal of applied physics, **95**, 2 (2004).

[26] B. Oliver et al. *Tunneling criteria and breakdown for low resistive magnetic tunnel junctions.* Journal of Applied Physics, **94**, 1783-1786 (2003).

[27] J. G. Simmons *Generalized Formula for the Electric Tunnel Effect between Similar Electrodes Separated by a Thin Insulating Film.* J. Appl. Phys. **34**, 1793 (1963).

[28] W. F. Brinkman, R. C. Dynes, and J. M. Rowell *Tunneling conductance of asymmetrical barriers.* J. Appl. Phys. **41**, 1915 (1970).

[29] J. Ventura et al. *Pinholes and temperature-dependent transport properties of MgO magnetic tunnel junctions.* Physical Review B **78**, 024403 (2008).

[30] N. Garcia *Conducting ballistic magnetoresistance and tunneling magnetoresistance: Pinholes and tunnel barriers.* Applied Physics Letters **77**, 1351 (2000).

[31] G. Tatara, Y.-W. Zhao, M. Muñoz, and N. García *Domain Wall Scattering Explains 300% Ballistic Magnetoconductance of Nanocontacts.* Phys. Rev. Lett. **83**, 2030 (1999).

[32] P. Graziosi, M. Prezioso, A. Gambardella, C. Kitts, R.K. Rakshit, A. Riminucci, I. Bergenti, F. Borgatti, C. Pernechele, M. Solzi, D. Pullini, D. Busquets- Mataix, and V.A. Dediu. *Conditions for the growth of smooth La0.7Sr0.3Mno3 thin films by pulsed electron ablation.* Thin Solid Films, 534(0):83 – 89 (2013).

[33] R. Waser , M. Aono *Nanoionics-based resistive switching memories* Nature Materials **6**, 833 (2007).

[34] A. Yildiz et al. *Crossover from Nearest-Neighbor Hopping Conduction to Efros–Shklovskii Variable-Range Hopping Conduction in Hydrogenated Amorphous Silicon Films.* Japanese Journal of Applied Physics **48**, 111203 (2009).

[35] C. J. Adkins *Conduction in granular metals-variable-range hopping in a Coulomb gap?* J. Phys.: Condens. Matter **1**, 1253 (1989).

[36] A. L. Efros and B. I. Shklovskii *Electronic Properties of Doped Semiconductors.* Springer, Berlin, 1984.

[37] R. Rosenbaum *Crossover from Mott to Efros-Shklovskii variable-range-hopping conductivity in $I_x O_x$ films.* Physical Review B **44**, 44, 3599 (1991).

[38] J. M. Ziman *Electrons and Phonons.* Clarendon Press, Oxford, (1960).

[39] Amilcar Bedoya-Pinto *Spin-Polarized Hopping Transport in Magnetically Tunable Rare-Earth Quinolines.* Adv. Electron. Mater. **2015**, 1, 1500065 (2015).

[40] M. Choi et al. **Anti-ferrodistortive-Like Oxygen-Octahedron Rotation Induced by the Oxygen Vacancy in Cubic SrTiO 3**. Adv. Mater. **2013**, 25, 86–90 (2013).

[41] M. Ahrens et al. *Effective masses of electrons in n-type* $SrTiO_3$ *determined from low-temperature specific heat capacities.* Physica B **393**, 239 (2007).

[42] K. Szot et al. *Switching the electrical resistance of individual dislocations in single-crystalline* $SrTiO_3$. Nature Materials **5**, 312-320 (2006).

[43] R. Muenstermann et al. *Coexistence of Filamentary and Homogeneous Resistive Switching in Fe-Doped* $SrTiO_3$ *Thin-Film Memristive Devices.* Adv. Mater. **2010**, 22, 4819–4822 (2010).

[44] X. Sun et al. **Unipolar memristors enable "stateful" logic operations via material implication**. Applied Physics Letters **99**, 072101 (2011).

[45] J. Z. Sun et al. **Interface stability in hybrid metal-oxide magnetic trilayer junctions**. Physical Review B, **61**, 17, 11244 (200).

[46] I. J. Vera Marún et al. **Tunneling magnetoresistance with positive and negative sign in** $La_{0.67}Sr_{0.33}MnO_3$ **/**$SrTiO_3$ **/Co junctions**. Physical Review B **76**, 064426 (2007).

[47] M. Viret et al. **Low-field colossal magnetoresistance in manganite tunnel spin valves**.Europhysics Letters, **39**, 5 (1997).